High Resolution Electron Beam Lithography

An improved understanding of a versatile lithography technique

Von der Fakultät Mathematik und Physik der Universität Stuttgart zur Erlangung der Würde eines Doktors der Naturwissenschaften (Dr. rer. nat.) genehmigte Abhandlung

Vorgelegt von

Marcus Rommel

aus Eisenach

Hauptberichter:	Prof. (apl.) Dr. Jürgen Weis
Mitberichter:	Prof. Dr. Martin Dressel
Tag der mündlichen Prüfung:	22.03.2018

Max-Planck-Institut für Festkörperforschung
Stuttgart, 2018

Contents

List of Figures

Lists of abbreviations and symbols

Symbols

a	edge length or lattice constant
A_{exp}	exposed area
D	dose
D_B	base dose
d_{beam}	beam diameter
d	diameter
D_{ring}	dose applied to a ring
DF	dose factor
DTS	dose to size
DTS_{G}	dose to size for a grating spanning over a large area
DTS_{S}	dose to size for a large square
$\mathcal{E}_z$	exposure in a material slice extracted at height z
$\mathcal{E}_{z,in}$	intrinsic exposure in a material slice extracted at height z
$\mathcal{E}_{z,\text{norm}}$	normalized exposure in a material slice extracted at height z
$\mathcal{E}_{z,\text{norm},S}$	normalized exposure in a material slice extracted at height z in the center of a disk
$\mathcal{E}_{z,\text{norm},S,f}$	normalized exposure needed to achieve a final resist thickness
$\mathcal{E}_{z,\text{norm},S,i}$	normalized exposure needed to achieve an initial resist thickness
$\mathcal{E}_{z,\text{norm},S,\text{meas}}$	normalized exposure in a material slice extracted at height z derived from measured resist heights
$\mathcal{E}_{z,\text{norm},S,\text{simu}}$	simulated normalized exposure in a material slice extracted at height z
$\vec{E}$	electric field
E_1	deposited energy by an average electron in an exposed sample
$E_{1,z}$	deposited energy by an average electron in a material slice extracted at height z
E_{tot}	total deposited energy in an exposed sample
$E_{\text{tot},z}$	total deposited energy in a material slice at height z

f	frequency or flow of gas
F	filling factor
$g_\sigma(r)$	Gaussian function with FWHM σ
LADTC	large area dose to clear
I	beam current
I_{holo}	intensity profile in a hologram
M_w	molecular weight
N	number of electrons
O	point of origin
p	exposed pattern or pressure
p_{DTS}	large line grating with 50% duty cycle
p_{LADTC}	large square
P	observation point or power
PSF	point spread function
PSF_z	point spread function extracted for a material slice at height z
t	time
t_{bin}	thickness of an investigated material slice
T	temperature
T_g	glass transition temperature
Z	atomic number
α	FWHM of the forward scattering Gaussian function in the double Gaussian model or angle of incidence
β	FWHM of the backscattering Gaussian function in the double Gaussian model
γ	resist contrast
ε_1	energy density deposited by an average electron in an exposed sample
$\varepsilon_{1,\text{DG,norm}}$	normalized energy density deposited by an average electron calculated for a double-Gaussian PSF
$\varepsilon_{1,z}$	energy density deposited by an average electron in a material slice extracted at height z
$\varepsilon_{1,z,\text{inf}}$	energy density deposited by an average electron in a material slice extracted at height z for an infinite pattern
$\varepsilon_{1,z,\text{norm}}$	normalized energy density deposited by an average electron in a material slice extracted at height z
$\varepsilon_{1,z,\text{norm,inf}}$	normalized energy density deposited by an average electron in a material slice extracted at height z for an infinite pattern
$\varepsilon_{\text{DTS,G}}$	normalized energy density deposited by an average electron at the edge of a line in the center of a large line grating calculated for a double-Gaussian PSF

$\varepsilon_{\mathrm{DTS,S}}$	normalized energy density deposited by an average electron at the edge of a large square calculated for a double-Gaussian PSF
$\varepsilon_{\mathrm{LADTC}}$	normalized energy density deposited by an average electron in the center of a large square calculated for a double-Gaussian PSF
$\varepsilon_{\mathrm{ring}}$	normalized energy density deposited by an average electron in a material slice extracted at height z in the center of a concentric ring
$\varepsilon_{\mathrm{sens}}$	normalized energy density deposited by an average electron in a material slice extracted at height z in the center of a disk
η	weighing factor between forward and backscattering in the double Gaussian model
λ	wavelength
ρ	material density
ρ_{disks}	areal density of disks
Θ	Heaviside step function
Ψ_{ref}	reference plane wave
Ψ_t	plane wave with topological charge

Abbreviations

AFM	atomic force microscope
AOI	angle of incidence
aSNOM	apertureless scanning near-field microscope
BOE	buffered oxide etch
CSDA	continuous slowing down approach
DACS	detailed atomic cross sections method
EBL	electron beam lithography
EELS	electron energy loss spectroscopy
EMCD	energy-loss magnetic chiral dichroism
FIB	focused ion-beam milling
HCL	hole-mask colloidal lithography
HF	hydrofluoric acid
HSQ	hydrogen silsesquioxane
IPA	isopropyl alcohol
LSPR	localized surface plasmon resonance
MIBK	methyl isobutyl ketone
MCS	Monte-Carlo simulation
MPI-FKF	Max Planck Institute for solid state research

NA	numerical aperture
NaOH	sodium hydroxide
NCM-AFM	non-contact mode atomic force microscopy
NEA	nuclear energy agency
NEP	n-ethyl pyrrolidone
NFL	Nanofabrication Laboratory
NH_4F	ammonium fluoride
NIL	nanoimprint lithography
NSL	Nanostructuring Lab
OAM	orbital angular momentum
OECD	organization for economic co-operation and development
PE	proximity effect
PEC	proximity effect correction
PMMA	poly(methyl methacrylate)
POI	point of injection
PS	polystyrene
RIE	reactive ion etching
SE	secondary electrons
SEM	scanning electron microscope
SHG	second-harmonic-generation
StEM	Stuttgart Center of Electron Microscopy
TEM	transmission electron microscope
TMAH	tetramethylammonium hydroxide
UHV	ultra-high-vacuum
VASE	variable-angle spectroscopic ellipsometer

1. Introduction

Electron beam lithography (EBL) is a prevalent technique used in research as well as in industry to define patterns in resists to locally protect the underlying substrate during subsequent processing steps. It features high-resolution patterning capabilities down to a few nanometers and an amazing versatility.

EBL is used for the production of optical lithography masks for semiconductor industry and is therefore a key technology to meet the required component densities and computing performance of state-of-the-art microchips [1, 2, 3, 4]. Another lithography technique at the border to industrial relevance is nanoimprint lithography (NIL) [5, 6, 7, 8], which relies on stamps fabricated by EBL, too [9, 10]. In contrast, in basic research institutions EBL is often used to directly pattern resist masks on a substrate. Often the resist itself acts as a pattern transfer layer and is removed in the end. In such cases the patterned substrate or deposited material are the objects of interest. The large variety of resists and substrate materials, as well as the spectrum of requested patterns, cause many challenges in EBL. Usually, for each material resist combination a new process has to be developed, sometimes the individual parameter are depending on the pattern, too [2, 3].

Nevertheless, due to the high flexibility and compatibility to many substrate materials, EBL has many fields of application in science. For instance neurobiology to pattern substrates for growing nerve cell networks [11, 12] and biophysics to create micro or nanofluidic cells [13, 14]. Solid state physics also profits from EBL in various ways, for example to pattern contacts or gates on different materials [15, 16], defining quantum point contacts [17] or to fabricate plasmonic structures [18, 19]. Further fields of application are the fabrication of micro and nano electro mechanical systems [20, 21] or integrated circuits [2, 22]. They rely on the resolution and flexibility of EBL as well. This is only a very small collection of research applications.

The basic requirement for EBL is a well controlled electron beam. As electron sources different materials and extraction methods are possible. Nowadays the most common emitter type in high end EBL is the thermal assisted field emission emitter [3]. Usually this sharply-pointed Schottky type emitter consists of tungsten coated with zirconium oxide to lower the barrier for extracting the electrons [2]. To further reduce the necessary extraction voltage and to

increase the extraction current the tip is heated to a temperature between 1500 K and 2000 K [2]. By setting the emitter to a negative potential of a few kilo volt relative to the extractor electrode, electrons are extracted. The electrons are accelerated further and thereafter focused on the sample. Today, commercial EBL tools provide up to 130 kV acceleration voltage [23]. To focus the electron beam, magnetic electron optical lenses are used and either magnetic or electrostatic deflection units allow a precise positioning of the electron beam. State-of-the-art EBL systems use vector scanning to guide the beam over the sample. Thereby the beam can be positioned freely in the writing-field and scanned according to the grid and therefore the beam is not necessarily rastered over the whole writing-field. For Gaussian-beam-writers the deflected electron beam can be focused down to a spot of a few nanometer size and circular shape [2]. In contrast to the Gaussian-beam-writer the so-called shape-beam EBL systems can modify the shape and size of the area in which the electron beam hits the substrate. However the achievable minimal spot size of the shape-beam systems is usually not as small as for the Gaussian-beam-writer. The use of different shapes with variable area allows a faster exposure since the beam can be adapted to the pattern instead of filling the exposed area with circular shots. For fabricating nano-structures the focus diameter on the sample is one of the limitations for the feasible resolution. The focal spot size is influenced by the column design, the source size, the current density, and the acceleration voltage [2]. Further the resolution is limited by the fabrication process and electron scattering, too.

The EBL fabrication processes consist of several steps and usually starts by spin coating a thin film of resist on top of a plane substrate. The resist-covered substrate is then exposed by scanning the electron beam over the sample and the injected electrons lead to a modification of the chemical and physical properties of the resist. Depending on the tone of the resist the electrons cause main-chain scissioning (positive tone resist) [24] or cross-linking (negative tone resist) [25] of the resist molecules. These modifications cause a change in the molecular weight and therefore a different solubility in the corresponding solvents (developer). In the development process the lighter fractions of the resist are dissolved, leaving a resist pattern on the substrate. Since the development result depends on the developer, time and temperature, these parameters have to be well controlled to achieve proper results. The patterned resist layer, protects the subjacent substrate locally. This resist mask can be used for further processing steps, thereby the substrate surface can be chemically etched, ion sputtered, chemically modified or covered by depositing material [2, 3]. Finally, the resist can be removed by a suitable 'remover' solvent, including the material on top of the resist. In Fig. 1.1 a typical fabrication flow for a metal lift-off process is

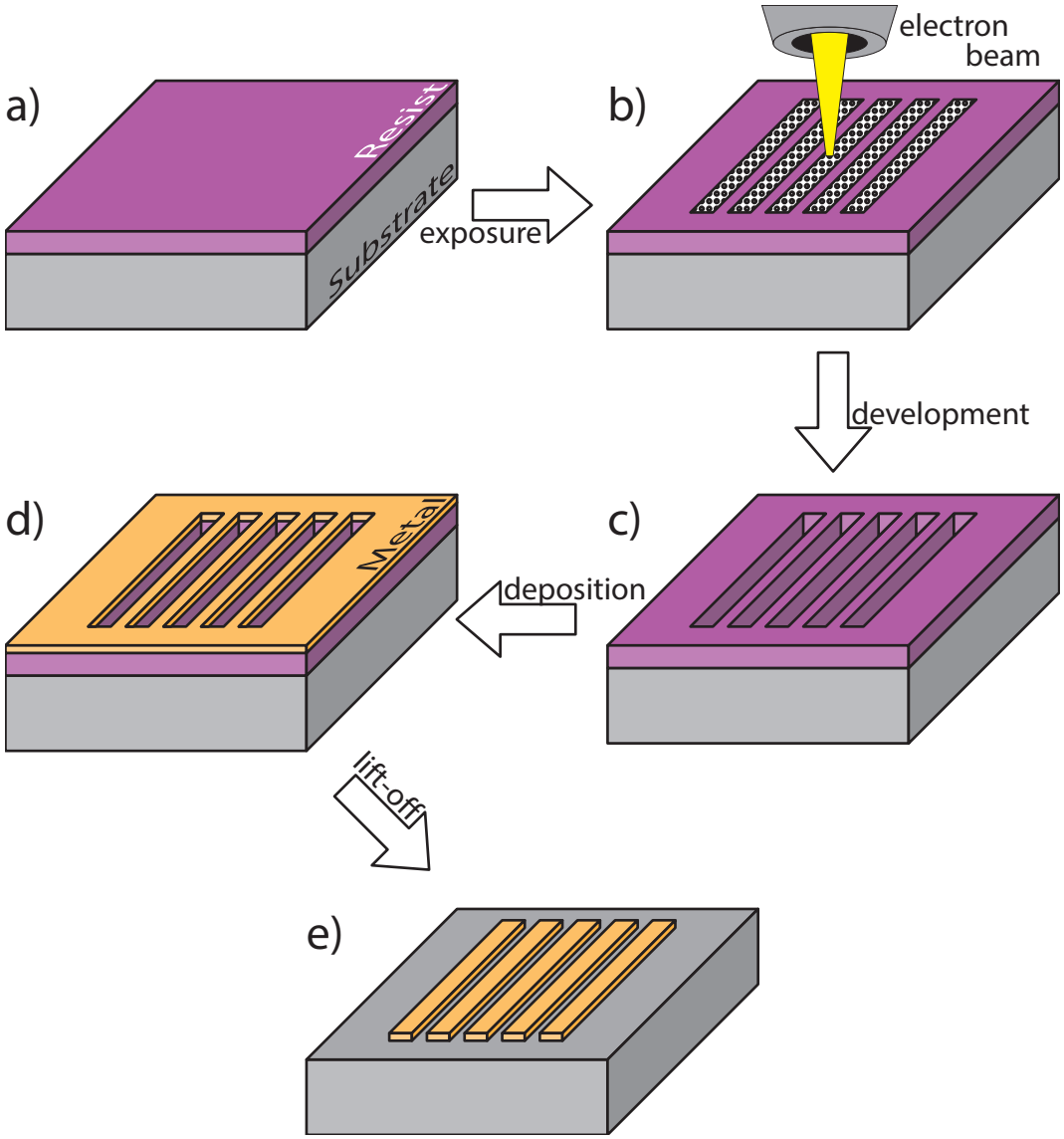

Figure 1.1.: Steps of a metal lift-off process: (a) Resist-covered substrate. (b) Pattern exposed into the resist. (c) Trenches created by developing the exposed sample. (d) Metal deposited on developed resist. (e) Final metal pattern after lifting-off the residual material.

presented. In this work mainly such lift-off techniques are used to create dense nano-structures.

One of the keys to understand EBL is to get insight how the electron beam modifies the resist on the microscopic scale and how these modifications lead via the development process to a resist pattern with a certain profile at the pattern edge. The local modification is controlled by the dose, which is the number of locally injected electrons into the resist. Usually, the dose is measured in terms of injected charge per area and given in units $\mu C\,cm^{-2}$. In order to control the dose for a given electron beam current, the dwell time on a point of injection (POI) and the distance between individual POIs can be modified. While the electrons penetrate the resist and substrate they are scattered many times and the modification of the resist happens due to inelastic scattering. The mean free path between scattering events, the scattering angle and loss of kinetic energy depend on one hand on the actual kinetic energy of the electron, on the other hand on the density and the atomic numbers of the elements in the material [26]. Compared to the resist, electrons reaching the substrate usually face an increase in density and atomic number of the material. Due to the changed material properties, the scattering probability, the energy transfer during inelastic scattering and the scattering angle can increase [26]. The electrons are actually able to be scattered back into the resist and cause further resist modifications at large distances from the POI.

The discussion above demonstrates that the resolution of EBL is not alone limited by the electron beam diameter at the POI. The complex electron scattering mechanisms inside the material leads to chemical modifications of the resist far away from the POI. For example the influenced range (3σ) by scattering during exposing a resist on silicon with 100 keV electrons is up to 100 µm, while for gallium-arsenide it is 40 µm and for bulk gold it is only 10 µm [27]. This phenomenon is called proximity effect (PE) and has to be taken into account to obtain finally the desired pattern in the resist. Due to the PE, writing a dense pattern with the same dose at each point will not lead to the desired resist pattern. Indeed, a common approach is to fracture the designed pattern in smaller areas and attribute different dose values to these smaller areas by defining a base dose D_B and a dose factor map $\mathrm{DF}(x, y)$. For simple and sparse designs this can be done even by hand in a trial-and-error procedure. However, such an approach is not feasible for pattern designs containing complex shapes and large variations in the pattern area density, as well as for dense patterns containing many shapes.

How to tackle the PE problem in a more general way? At a first approach a good measure for the expected local modification of resist might be to look at the energy density locally deposited by electron scattering in the resist.

It requires the knowledge of the so-called point spread function (PSF), i.e. the deposited energy density distribution for the lateral distance r from the POI caused by an injected electron. The electrons can only travel a certain distance inside the material stack before their initial energy is absorbed by inelastic scattering events. Therefore they can only contribute to the deposited energy density within a certain distance from the POI. For the fabrication, the energy density distribution in the resist is of interest since it will define the pattern after development. In order to calculate the expected energy density distribution after the exposure the PSF is convolved with the pattern. During the convolution the pattern design is locally weighted with a dose factor DF to consider different doses applied to different parts of the pattern. Using the obtained deposited energy density landscape it is possible to determine the expected pattern after development by assuming a development threshold value in the deposited energy density. The threshold can be considered as a contour in the deposited energy landscape, defining the resist pattern edge. For example, for a positive tone resist all regions where the deposited energy is higher than the threshold will be removed, while the rest of the resist stays. For a negative tone resist it is the other way around. This is a simplified model neglecting for instance several resist properties and processing effects. It is only considering the influence of electron scattering. Using the local DFs as parameters of control, the deposited energy density landscape can be modified until the desired resist pattern is obtained. This dose adaption is a feasible way to perform proximity effect correction (PEC) [2]. For 2D lithography using electrons with 100 keV, which is discussed in this thesis, PEC is usually only performed for a specific slice in the resist layer. Assuming the remaining slices behave similar, which is a fair assumption. The specific slice used for the PEC is defined by the used PSF_z. Therefore I am limiting my discussions to the PSF_z. If the PSF_z perfectly describes the overall EBL process, only a single experimental D_B value would be required to cross the energy density threshold at the designed pattern edges and therefore obtaining the correct resist structure after development.

Unfortunately it is not that simple:

1. The PSF_z might be obtained from physical simulations. However, the accuracy of the result depends on the completeness of the physical model used for the simulation. At which depth inside the resist layer one should determine the PSF_z?

2. In many cases, crude approximations for the PSF_z are taken with free parameters determined from experiments. What is their validity?

3. Does the deposited energy density distribution alone determine the result of the EBL process? Obviously not, as different resists under same exposure conditions show different results. For instance, cut-off pieces of resist molecules might diffuse away from the point of creation, modifying the solubility of the resist in the vicinity. To take care of such effects, a modified, empirically determined pseudo-PSF_z might be used.

4. A pseudo-PSF_z can be fine tuned in a trial-and-error procedure in comparison with experimental results. Is an adequate pseudo-PSF_z found for a certain type of pattern, it usually fails in case of other pattern designs. This might come from the effect that different concentrations of the chemicals will appear during the development process over pattern areas of different pattern density. The development process goes faster or slower, depending on the pattern density. Such effects - commonly denoted as process loading effects - are not mimicked by a pseudo-PSF_z.

5. The application of a high dose might locally heat and therefore rise the local temperature of the sample leading to chemical modifications in the resist. Here, the exposure strategy can influence the heating. The history of writing and modeling of local heating are - at present - not taken into account in simulations.

Already these considerations show, that EBL is still a challenging task, especially in the area of basic research with all these various substrate materials, resist materials, applications and - not to forget - the constantly evolving pattern designs, justifying scientific work to further understand EBL and push it to its physical resolution limits.

With this work I would like to contribute to the fundamental understanding of PSFs and PEC in EBL to improve the predictability of results. I concentrated on the fabrication of dense patterns using high-resolution EBL as well as the limiting processes or conditions. In order to understand EBL I studied the requirements for achieving a proper PEC result. Since appropriate PEC algorithms using sophisticated correction models are commercially available, I focused on studying and measuring PSF_zs and methods to determine the base dose D_B, since the PSF_z and the D_B are the two main ingredients for 2D PEC. PSFs can be determined experimentally or by using sophisticated simulation packages. In this work I compared two different simulation packages and realized that the consideration of secondary electron (SE) as moving particle instead of evenly distributing the energy of the SE has a measurable impact on the fabrication results. To prove the correctness of a simulated PSF_z as

well as to measure its range of validity I developed a method to experimentally validate a PSF_z.

D_B is a sort of starting point of the PEC. For the correction itself only multipliers are used to optimize the calculated energy density distribution to reach the threshold at the design pattern edges. The PEC does not know about the resist properties, therefore the D_B is used to tie the PEC to the physical resist. Determining the right D_B is always a source of concern, since it is not trivial to measure it. In this thesis I explain the most common ways to determine D_B and study there theoretical relation.

Still, if the PSF_z and D_B are correct, it is only possible to correct the influence of scattering by PEC. As mentioned before the exposure result might be affected by process effects, too. These process effects depend on the resist exposure chemistry and the developer resist interaction as well as the post processing [28, 29, 30]. Therefore differences between the designed and fabricated pattern can still occur even though a perfect PEC was applied. A good process control is important to preserve the achieved EBL resolution during the transfer in a functional device by lift-off or etching. I mainly worked with two common resists, with poly(methyl methacrylate) (PMMA) which was the main working horse at the Nanostructuring Lab (NSL) at the Max Planck Institute for Solid State Research and hydrogen silsesquioxane (HSQ) which is known for its high resolution capabilities. Both resists are complementary to each other, not only in their behavior under electron exposure, also in terms of resist chemistry.

Since PMMA is using solvent based developers and HSQ is developed using lyes, a bilayer of HSQ and PMMA can be used to profit from both resists properties. During my work I pushed this bilayer system into the sub-10 nm regime. Actually, I was able to create 100 nm gold squares with sub-10 nm separation over several square millimeters. This patterned films showed an unexpected broadband light absorption in the infrared region.

A second project, in which I was engaged in was the fabrication of a square millimeter sized pattern of randomly or tetragonal distributed gold disks. I fabricated structures with different disk densities, for each density I fabricated an ordered and a random version. Especially the random patterns are challenging for PEC since the overall density is constant, however locally it can vary remarkably. The final sample was used to investigate long range interaction of localized surface plasmon resonances.

Another interesting application was to perform EBL on 30 nm thin silicon nitride membranes. These membranes allowed me to fabricate special gold gratings with a line width of 30 nm. Since the membranes are that thin, the backscattering can be completely neglected and due to the high energy of the exposing electrons a correction for the forward scattering is not necessary, too.

In order to create PSFs for my corrections I am relying on a non-commercial sophisticated Monte-Carlo simulation (MCS) software called PENELOPE. This code suite is distributed by the Nuclear Energy Agency (NEA) belonging to the Organization for Economic Co-operation and Development (OECD). PENELOPE is commonly used for dosimetry in x-ray therapy, as well as for designing and developing of x-ray detectors and sources. Further PENELOPE calculates the trajectories and energy absorption for each electron, primary and secondary. The named applications and the physical approach encourage my trust, nevertheless the agreement between simulation and reality should be investigated carefully, since the simulations have to assume many boundary conditions [26].

I use the generated PSFs extracting the needed PSF_z and perform PEC with a commercial software called BEAMER developed and distributed by GenISys GmbH. This software provides different correction approaches and levels of detailedness. Besides the PSF_z based correction, further process and machine influences can be considered. BEAMER features further functionalities to process the pattern design and convert it into the native machine format of various EBL systems, as well as to simulate the exposure result.

To fabricate samples mainly the cleanroom facility Nanostructuring Lab (NSL) at the Max Planck Institute for Solid State Research was used. They provide state-of-the-art processing equipment. I used spin coaters, hotplates, and resistive evaporation tools from Leybold as well as a reactive ion etching (RIE) setup for the pre- and post-exposure processing of my samples. For the actual exposure a high-quality, spot-beam EBL system, a JBX-6300FS from JEOL was used. The JBX-6300FS allows a maximum acceleration voltage of 100 kV and provides an ultimate spot size of 2 nm as well as high stability. For investigating fabrication results I used a Zeiss Merlin scanning electron microscope (SEM). In addition to the NSL at the MPI-FKF, the Nanofabrication Laboratory (NFL) at Chalmers University of Technology was used. Providing two 100 kV EBL systems, a JEOL JBX-9300FS and a Raith EBPG5200 as well as advanced process and metrology equipment. Besides the EBL systems I used spin coaters, hotplates, an electron beam evaporator from Lesker, a Zeiss Supra 60 VP SEM and a Bruker Dimension ICON scanning probe microscope.

My thesis is divided into two parts. The first one is dedicated to the general investigation of PEC and resist properties. The PEC part is again split into several sections about the determination of D_B, a comparison of two different MCS packages and the description of my new process to validate PSF_zs experimentally. In the subsequent chapter about resist properties I describe the concept of contrast curves which is commonly used to classify resists. Further the resists PMMA and HSQ as well as the bilayer system HSQ

on PMMA are presented.

The second part of my thesis concentrates on applications. I am showing three different projects which are all very different and challenging from the lithography point of view. As a side effect two of these projects helped to study physical effects which were not accessible without the samples I fabricated.

Publications

With the support of my collaborators I was able to author and co-author the following publications:

- M. Rommel, K. Hoffmann, T. Reindl, J. Weis, N. Unal, and U. Hofmann, "Benchmark test of Monte-Carlo simulation for high resolution electron beam lithography," *Microelectronic Engineering*, vol. 98, pp. 202–205, 2012

- M. Rommel, B. Nilsson, P. Jedrasik, V. Bonanni, A. Dmitriev, and J. Weis, "Sub-10nm resolution after lift-off using HSQ/PMMA double layer resist," *Microelectronic Engineering*, vol. 110, pp. 123 – 125, 2013

- M. Rommel and J. Weis, "Hydrogen silsesquioxane bilayer resists - Combining high resolution electron beam lithography and gentle resist removal," *Journal of Vacuum Science and Technology B: Microelectronics and Nanometer Structures*, vol. 31, no. 6, pp. 06F102–1 – 06F102–5, 2013

- M. Rommel and B. Nilsson, "Estimating the optimum dose for arbitrary substrate materials based on Monte Carlo simulated point spread functions," *Microelectronic Engineering*, vol. 155, pp. 29–32, 2016

- R. Jany, C. Richter, C. Woltmann, G. Pfanzelt, B. Förg, M. Rommel, T. Reindl, U. Waizmann, J. Weis, J. Mundy, D. Muller, H. Boschker, and J. Mannhart, "Monolithically Integrated Circuits from Functional Oxides," *Advanced Materials Interfaces*, vol. 1, no. 1, pp. 1300031–1 – 1300031–7, 2014

- S. De Zuani, T. Reindl, M. Rommel, B. Gompf, A. Berrier, and M. Dressel, "High-Order Hilbert Curves: Fractal Structures with Isotropic, Tailorable Optical Properties," *ACS Photonics*, vol. 2, no. 12, pp. 1719–1724, 2015

- S. De Zuani, M. Rommel, R. Vogelgesang, J. Weis, B. Gompf, M. Dressel, and A. Berrier, "Large-Area Two-Dimensional Plasmonic Meta-Glasses

and Meta-Crystals: a Comparative Study," *Plasmonics*, vol. 12, pp. 1381–1390, Oct 2017

- S. De Zuani, M. Rommel, B. Gompf, A. Berrier, J. Weis, and M. Dressel, "Suppressed Percolation in Nearly Closed Gold Films," *ACS Photonics*, vol. 3, no. 6, pp. 1109–1115, 2016

Electron-beam-lithography

Improvement of the pattern definition and transfer to the resist

2. Proximity effect

One of the aims of my research is to fabricate samples benefiting from high-resolution EBL processes. To achieve the demanded resolution I identified three main topics influencing the feasible feature size: The electron beam focus spot size at the substrate, the sample fabrication process and the PE. This interdisciplinary challenge has to be addressed by combining engineering, material science and physics. Using sophisticated EBL tools, offering focus spot sizes smaller than 4 nm, able to expose sparse line gratings with 8 nm line width as well as 100 nm spacing, is a very good starting point for fabricating high-resolution samples for specific applications.

This chapter discusses and explains the proximity effect (PE) and its influence on the exposure as well as its correction. In order to ease the discussion I am assuming a positive tone resist is investigated if not stated differently. To be able to use the results of the proximity effect correction (PEC) on a real world sample the base dose D_B is needed.

There are several different possibilities to determine D_B and three of them are discussed in this chapter. Since the quality of the PEC is dependent on the accuracy of the point spread function (PSF_z), two different PSF simulation tools are evaluated. I developed two experimental evaluation methods to compare simulated PSF_zs. These methods and the evaluation are presented in this chapter. Followed by explaining a new method I developed to validate the PSF_z experimentally.

For the discussions in this chapter I have to refer to resist properties. A more thorough investigation of the properties of resists in general as well as for PMMA and HSQ are presented in chapter 3.

2.1. Introduction

The PE describes the unintended energy deposition in unexposed regions during the exposure caused by electron scattering. As mentioned before the influence of the PE can range up to hundreds of microns from the point of injection (POI) of the electrons, depending on the energy of the injected electrons as well as densities ρ and atomic numbers Z of the exposed material stack. Especially,

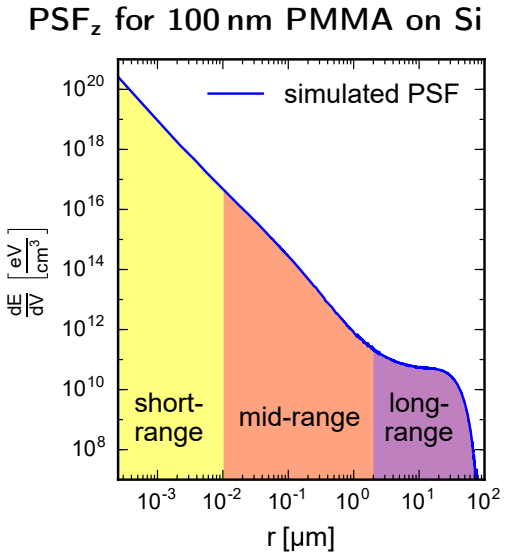

Figure 2.1.: PSF$_z$ simulated for a 100 nm thick PMMA layer on Si extracted at 50 nm from substrate surface and a layer thickness of 20 nm.

in regions with a high pattern density the PE can cause a high deposited energy density background, which results in an exposure bias of the resist. The exposure $\mathcal{E}_z$ is the product of the applied dose D, and $\varepsilon_{1,z}(x,y)$, the locally deposited energy density by an average electron in the layer z. z is the layer of the material stack the PSF$_z$ is extracted from. $\varepsilon_{1,z}(x,y)$ is derived by a convolution of the pattern $p(x,y)$ with the PSF$_z$ considering the dose factor map DF(x,y):

$$\mathcal{E}_z(x,y) = D \cdot \varepsilon_{1,z}(x,y), \tag{2.1}$$

with:

$$\varepsilon_{1,z}(x,y) = (p(x,y) \cdot \mathrm{DF}(x,y)) * \mathrm{PSF}_z(r) \tag{2.2}$$

As mentioned before DF(x,y) is used to describe the locally applied dose in side the pattern (PEC). The convolution in Eqn. (2.2) assumes a flood exposure of the pattern. In reality the pattern is exposed by many shots spaced by a certain distance. The spacing of the shots and the diameter of the electron beam are usually chosen to cause the individual shots to overlap. Therefore, a flood exposure is an acceptable approximation.

The PE can be quantified by the help of a PSF$_z$ that describes the energy density deposition distribution inside the material stack caused by electron scattering. PENELOPE averages the PSF using many - typically several millions

- injected electrons and provides the energy density deposition distribution for an average electron. The PSF_z shown in Fig. 2.1 is simulated for 100 nm PMMA on silicon and was extracted at half thickness of the resist layer for a $t_{bin} = 20$ nm thick resist sheet. Physically the PSF is gradually changing over the whole resist thickness. For technical reasons PENELOPE is however binning the deposited energy into finite bins [26]. Choosing bins with a height of $t_{bin} = 20$ nm has proven to be a good compromise between simulation time and PSF_z quality. Usually, the PSF_z is extracted from a slice around the middle of the resist height with thickness t_{bin}. PENELOPE assumes a homogeneous material neglecting for example effects caused by the crystalline nature of the substrate or the molecular weight of the resist. The parameters required for the Monte-Carlo simulation (MCS) are thickness, density and stoichiometric formula of all materials in the simulated stack.

If the PSF_z is investigated more thoroughly, three different regions are distinguishable in the plot. In the range of few nanometers around the POI the energy density is influenced by forward scattering. This part of the PSF_z is named the short-range. Manfrinato *et al.* [38] published an article in which they refer to "volume plasmons" as another quantity influencing the shape of the PSF_z in the short-range region. In their description "volume plasmons" are longitudinal oscillations of valence electrons in the bulk resist and are generated during inelastic scattering events. Those may expose the resist directly or decay to secondary electrons (SEs) modifying the resist. Depending on the MCS package used to determine the PSF_z a finite beam diameter at the POI can be chosen. This beam diameter would influence the short-range part of the PSF_z, too.

From a few nanometers to approximately 2 µm away from the POI in Fig. 2.1, the PSF_z shape is influenced by the mid-range effect, which is attributed mainly to energy deposition by fast secondary electrons generated during the scattering. A common approximation of the PSF_z is done using a double-Gaussian model [39, 40, 41] which describes a simulated PSF_z properly, if the SEs are not simulated as individual moving particles. However, as presented in the following sections I proved experimentally the necessity of considering the SEs as individual moving particles in the simulation, in order to improve the resulting PSF_z.

The third part of the PSF_z is the long-range region, attributed to the energy deposition by the backscattered electrons, ranging from approximately 2 µm to approximately 100 µm in Fig. 2.1.

The mentioned radius values separating short-, mid- and long-range are specific for the analyzed PSF_z and depend on the energy of the injected electrons as well as the material stack, therefore these values can vary. Using

PSF_zs to predict the PE allows its algorithmic correction. Since the PSF_z depends only on the initial electron energy and the material stack, it can be used for the PEC of any pattern design. However, I am going to focus on the PSF_z extracted at the middle of the resist height and their influence on the 2D PEC. Using algorithm-based PEC, it is possible to reduce the number of test exposures and thus save time as well as costs, in contrast to manual correction by trail and error.

The undesired discrepancy between the designed and the achieved pattern can be reduced by changing the dose locally to compensate for the PE and processing effects. In order to achieve the designed pattern, the deposited energy density $\varepsilon_{1,z}$ and thereby $\mathcal{E}_z$ outside of the designed pattern has to be low enough that the resist has a sufficient thickness after development to not influence the fabrication result. The response of the resist to the received $\mathcal{E}_z$ caused by the applied dose is characterized by a contrast curve, which describes the dependency of the resist height on the dose in a large exposed area after development. In the middle of a sufficiently large pattern, $\varepsilon_{1,z}$ becomes constant and therefore the remaining resist height is related to $\mathcal{E}_z$ via the contrast curve (see Eqn. (2.1)). Contrast curves describe a certain process and depend on the resist type and thickness, the substrate material and thickness, the developer, the developer temperature and development time as well as the energy of the injected electrons.

To simplify the correction a resist with step-like contrast curve is assumed. This simplification allows to apply a development threshold to $\varepsilon_{1,z}(x, y)$ instead of transforming it by using the more complex contrast curve. As explained in chapter 1 the threshold method assumes that the pattern is transfered into the resist correctly if $\varepsilon_{1,z}(x, y)$ is higher inside and lower outside of the pattern than the development threshold, independent of the magnitude of the difference. This simplification reduces the complexity of the correction considerably however causes uncertainties in the resist profile prediction. In many cases this is a minor issue since the resist behavior is sufficiently step-like or the critical pattern dimensions are large enough to be not effected by this simplification.

Besides PEC by dose modulation using $\mathrm{DF}(x, y)$ it is possible to adapt the pattern in order to achieve the desired $\varepsilon_{1,z}(x, y)$, however this approach is less common. The dose modulation might be more flexible, since the dose can be adjusted more accurately than the pattern can be changed, since the pattern will be exposed by individual shots, which have to be aligned on the machine grid. Both correction mechanisms are available in BEAMER. This software uses the explained development threshold method to optimize the dose so that the edge of the exposed pattern receives the defined threshold energy density.

To emphasize the possibilities of PEC two hypothetical fabrication processes are compared. Both process expose the pattern shown in Fig. 2.2(a) and follow the same flow, however the first neglects PEC while the second considers PEC. The intermediate and final results for the case neglecting PEC are shown in Fig. 2.3(a)+(c) as well as in Fig. 2.4(a). For the process using PEC the results are depicted in Fig. 2.3(b)+(d) as well as in Fig. 2.4(b). For the comparison the following items are discussed:

- Pattern definition.
- Simulated energy density distribution after exposure.
- Resist profile.

Pattern The test pattern consists of five 200 nm wide, 2 µm long stripes, separated by 100 nm, surrounded by a 20 µm wide frame, as shown in Fig. 2.2(a). As material stack a gallium arsenide wafer coated with 100 nm PMMA is assumed. Due to the high pattern density, a strong background $\varepsilon_{1,z}(x, y)$ and $\mathcal{E}_z$ caused by backscattered electrons is expected. Thus this pattern is a proper example to study the PE and its correction. For the uncorrected case the whole pattern gets the same dose D_B assigned, accordingly the design for each shape in Fig. 2.2(a) $\mathrm{DF}(x, y) = 1$.

For the PE corrected case the same pattern is corrected using BEAMER and the PSF_z presented in Fig. 2.2(c). This exemplary PSF_z is simulated for PMMA on gallium arsenide and 100 keV acceleration voltage, assuming an infinitesimal small electron beam. The PSF_z is extracted at 50 nm from substrate surface and a layer thickness of 20 nm. The PEC result using BEAMER is shown in Fig. 2.2(b), where the colors represent different DF allocated in the individual regions. Due to backscattering the deposited energy density in the center is higher than in the corners therefore the applied dose is decreased towards the center and increased in the corners. The DFs range from $\mathrm{DF}_{\mathrm{min}} = 0.66$ in the center to $\mathrm{DF}_{\mathrm{max}} = 1.46$ in the corners. The dominating effect in our test is backscattering. As a result of this dose variation obtained from PEC, the shapes in the center of the pattern get the same dose assigned as their proximity.

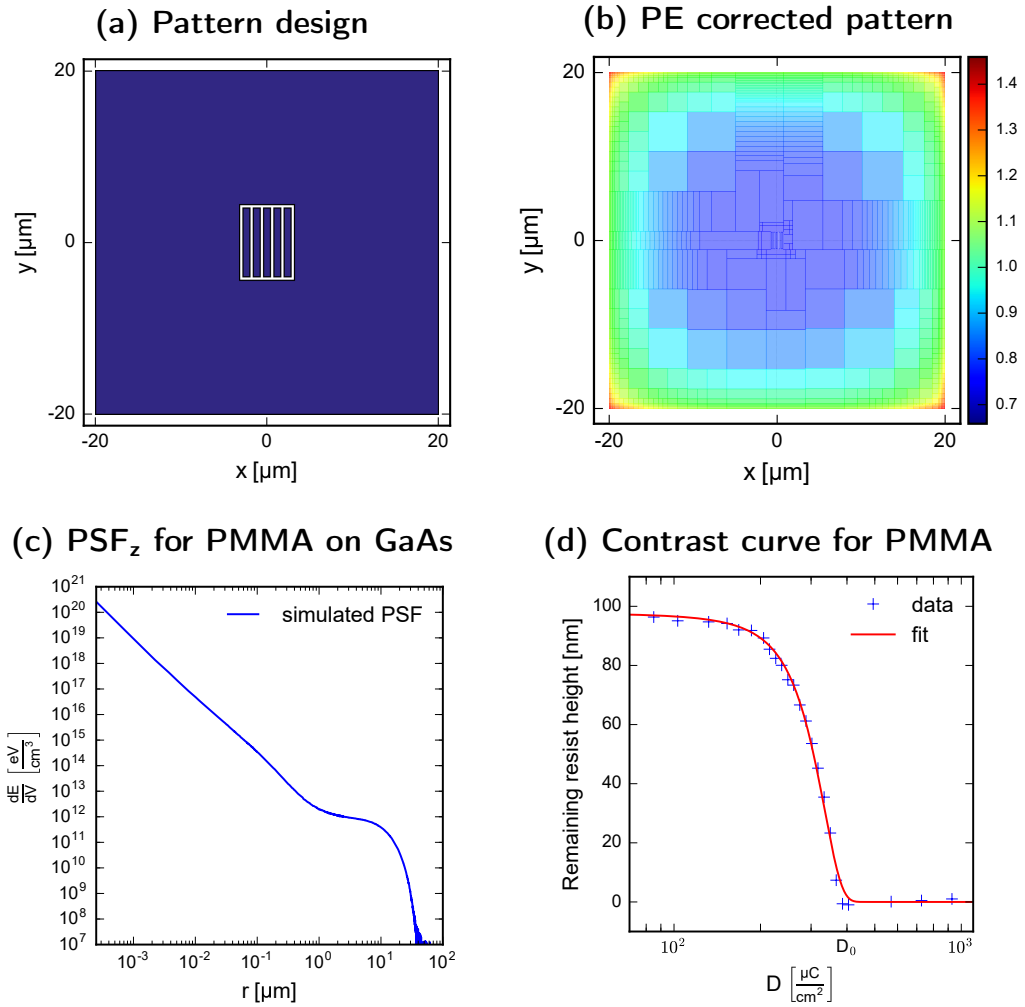

Figure 2.2.: (a) Test pattern, the whole blue area is exposed using the same dose. (b) PE corrected test pattern, the dose is modulated to compensate for the PE. (c) PSF$_z$ simulated for a 100 nm thick PMMA layer on GaAs extracted at 50 nm from substrate surface and a layer thickness of 20 nm. (d) Contrast curve determined for 100 nm PMMA on GaAs, developed in MIBK:IPA 1:3 volume ratio for 1 min.

Deposited energy density distribution As stated in the beginning of this chapter $\varepsilon_{1,z}(x,y)$ can be calculated by convolving the DF-weighted pattern $p(x,y)$ with the $\mathrm{PSF}_z(r)$ (see Eqn. (2.2)). As simulation result BEAMER provides the normalized exposure $\mathcal{E}_{z,\mathrm{norm}}$ [42], which can be calculated according to Eqn. (2.1) by replacing $\varepsilon_{1,z}$ with the normalized deposited energy distribution for an average electron $\varepsilon_{1,z,\mathrm{norm}}$.

$$\mathcal{E}_{z,\mathrm{norm}}(x,y) = D\,\varepsilon_{1,z,\mathrm{norm}}(x,y). \tag{2.3}$$

with:

$$\varepsilon_{1,z,\mathrm{norm}}(x,y) = \big(p(x,y)\,\mathrm{DF}(x,y)\big) * \mathrm{PSF}_{z,\mathrm{norm}}\,(x,y) \tag{2.4}$$

In contrast to Eqn. (2.2) for the convolution the normalized point spread function $\mathrm{PSF}_{z,\mathrm{norm}}$ is used.

In order to calculate the normalization factor the PSF_z is rotated around the energy density axis. The volume surrounded by the rotated PSF_z and the plane of zero energy density is the normalization factor. The $\mathrm{PSF}_{z,\mathrm{norm}}$ is defined by dividing the PSF_z with the normalization factor. Therefore the rotation volume of $\mathrm{PSF}_{z,\mathrm{norm}}$ is one. By using the normalized $\mathrm{PSF}_{z,\mathrm{norm}}$ the convolution with the pattern can be understood as a weighted averaging of $\mathrm{PSF}_{z,\mathrm{norm}}$ and pattern [43]. Further the use of the $\mathrm{PSF}_{z,\mathrm{norm}}$ allows to verify the convolution result. Corroding to the mean value theorem is the volume described by the pattern before and after the convolution identical. Additionally, the simulated normalized deposited energy density $\varepsilon_{1,z,\mathrm{norm}}$ will be between 0 and 1 using a $\mathrm{PSF}_{z,\mathrm{norm}}$ which allows a direct prediction of the resist edge using the threshold model. Further information can be found in the appendix A.2.

The amount of energy deposited in the resist is assumed to be proportional to the applied dose. The energy spread causing the deviations from the designed pattern is described by the PSF_z. By convolving the designed pattern with a normalized version of the PSF_z shown in Fig. 2.2(c) including the DFs for the uncorrected and corrected pattern the resulting normalized energy density distribution in the resist can be calculated [39]. Detailed considerations concerning the calculation of the total deposited energy and the deposited energy density can be found in the appendix A.1.

For the following consideration the $D = 1$ was chosen in order to separate the simulation results from a resist process. Therefore the $\mathcal{E}_{z,\mathrm{norm}}(x,y) = \varepsilon_{1,z,\mathrm{norm}}(x,y)$ and the simulation results will be discussed in terms of deposited energy density without any loss of generality.

Fig. 2.3(a) is the normalized 2D spatial resolved distribution of the deposited energy density $\varepsilon_{1,z,\mathrm{norm}}(x,y)$ for the uncorrected case simulated by BEAMER using and normalizing the PSF_z shown in Fig. 2.2(c). Fig. 2.3(b) is the

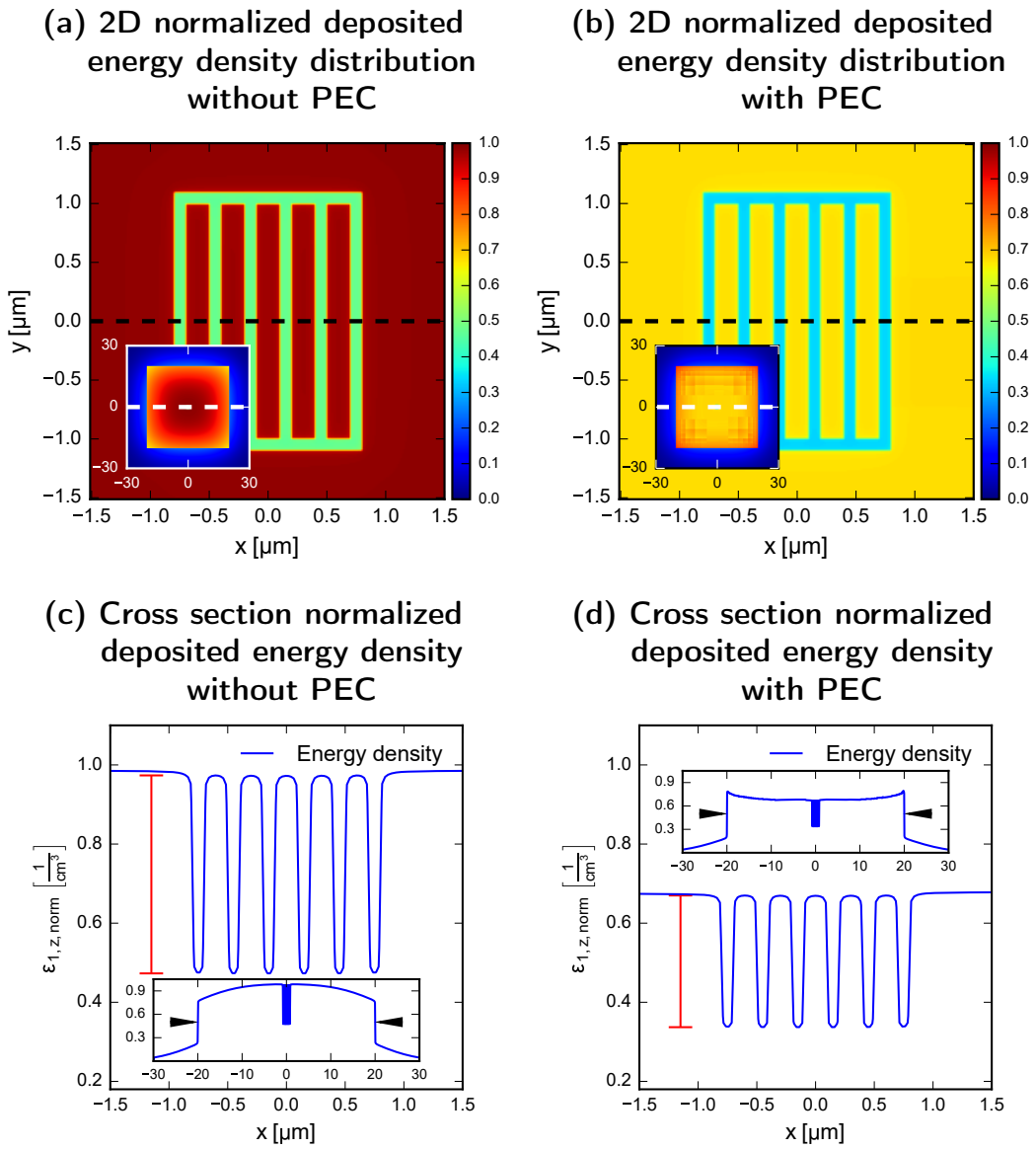

Figure 2.3.: (a) 2D normalized deposited energy density distribution calculated for the uncorrected case (convolution of Fig. 2.2(a) with Fig. 2.2(c)). (b) 2D normalized deposited energy density distribution calculated for the PE corrected case (convolution of Fig. 2.2(b) with Fig. 2.2(c)). (c) Normalized deposited energy density profile along the black and white dashed line in (a). (d) Normalized deposited energy density profile along the black and white dashed line in (b). The black arrows (c) and (d) indicate the outer pattern edge and the red marker emphasizes the normalized deposited energy density ratio for exposed and unexposed areas in the middle of the pattern.

counterpart for the PE corrected case. Both share the same color scale. The figures show a zoom-in to the region of interest while the inserts in both figures present an overview.

At the first glance $\varepsilon_{1,z,\mathrm{norm}}(x,y)$ in the center for the uncorrected case is higher, approximately by 30 % and is close to one. Additionally, $\varepsilon_{1,z,\mathrm{norm}}(x,y)$ in the unexposed region in the center reaches almost 0.5, which is caused by the background originating from the exposed frame. The insert shows a high $\varepsilon_{1,z,\mathrm{norm}}(x,y)$ in the pattern center which decreases towards the edges and corners of the frame. In the PE corrected case $\varepsilon_{1,z,\mathrm{norm}}(x,y)$ is lower both in the exposed and the unexposed areas in the center. Furthermore $\varepsilon_{1,z,\mathrm{norm}}(x,y)$ is increasing from the center to the corners as observed in the insert.

Fig. 2.3(c) and Fig. 2.3(d) present $\varepsilon_{1,z,\mathrm{norm}}(x, y = 0)$ along the white and black dashed lines for the uncorrected and corrected case. These plots show the mentioned reduction of $\varepsilon_{1,z,\mathrm{norm}}$ in the center of the pattern for the PE corrected case. In the insert in Fig. 2.3(d) $\varepsilon_{1,z,\mathrm{norm}}(x, y = 0)$ increases from the center to the edges. Additionally, the steepness of $\varepsilon_{1,z,\mathrm{norm}}(x, y = 0)$ at the outer edge (see black arrow in Fig. 2.3(c)+(d)) is higher for the PE corrected case. Interestingly, the ratio of $\varepsilon_{1,z,\mathrm{norm}}$ for the exposed and unexposed areas in the center of the PE corrected (red marker in Fig. 2.3(d)) is smaller than in the not corrected (red marker in Fig. 2.3(c)) case. The steepness of the $\varepsilon_{1,z,\mathrm{norm}}$ profile at a pattern boundary and the $\varepsilon_{1,z,\mathrm{norm}}$ ratio between exposed and unexposed regions influence the stability of a lithography process. In general, the steeper the profile and the larger the ratio the higher is the stability. However, the background is important, too. Even though the $\varepsilon_{1,z,\mathrm{norm}}$ ratio in the uncorrected case is larger, the overall background is so high that a strong overexposure in the center is expected. The reduced background in the center as well as the improved $\varepsilon_{1,z,\mathrm{norm}}$ profile steepness in the PE corrected case will improve the pattern fidelity and increase the process stability.

Resist profile Since the $\varepsilon_{1,z,\mathrm{norm}}(x,y)$ in the resist is known, the final topography of the resist can be determined by applying the resist contrast curve presented in Fig. 2.2(d). According to the threshold model used by BEAMER ($\varepsilon_{1,z,\mathrm{norm}}(x,y) \geq 0.5$ resist is removed) $\mathcal{E}_{z,\mathrm{norm}}$ is defined as:

$$\mathcal{E}_{z,\mathrm{norm}}(x,y) = 2\, D_0\, \varepsilon_{1,z,\mathrm{norm}}(x,y), \tag{2.5}$$

with D_0 as the large area dose to clear (LADTC) extracted from Fig. 2.2(d). The LADTC is the dose needed to clear the center of a large expose area after development. A detailed discussion with more information is presented in the next section.

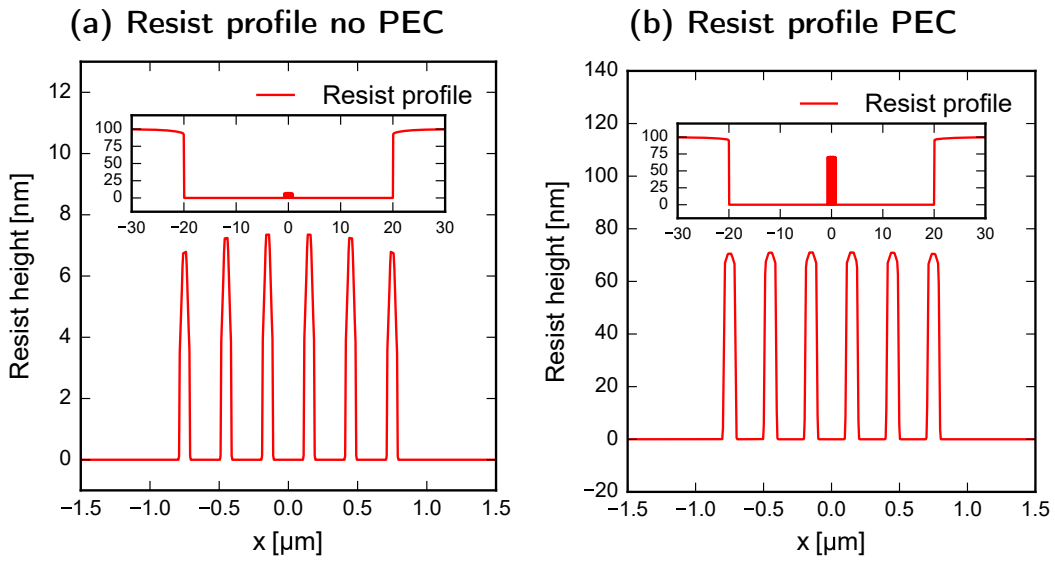

Figure 2.4.: (a) Resist profile for the uncorrected case, derived from Fig. 2.3(c) by applying the contrast curve presented in Fig. 2.2(d). (b) Resist profile for the uncorrected case, derived from Fig. 2.3(d) by applying the contrast curve presented in Fig. 2.2(d).

As mentioned, BEAMER provides $\mathcal{E}_{z,\mathrm{norm}}$ as simulation result. For a sufficiently large pattern $\varepsilon_{1,z,\mathrm{norm}}(x,y) = 1$ in the center of the pattern and $\mathcal{E}_{z,\mathrm{norm}} = D$ (see Eqn.(2.3)). The contrast curve is measured using such a pattern. After multiplying the simulated $\varepsilon_{1,z,\mathrm{norm}}$ shown in Fig. 2.3(c)+(d) with $2\,D_0$ the contrast curve can be applied to determine the expected resist profiles shown in Fig. 2.4(a)+(b).

Fig. 2.4(a) presents a cross section of the final resist topography in the center region for the uncorrected case. The calculated remaining resist height is less than 10 % of the original resist thickness, due to the high $\varepsilon_{1,z,\mathrm{norm}}$ background. Additionally, the width of the resist features shrinks, too. In the insert a cross section of the resist topography over the whole pattern range is illustrated. By comparing the center region with the pattern edges the decrease in thickness is even more obvious. Another effect can be observed while investigating the overview. In the unexposed region close to the pattern edge a decreased resist thickness and a rounding off of the top edge can be found caused by the PE, too.

In Fig. 2.4(b) the calculated resist height for the PE corrected case is shown. Comparing the uncorrected and corrected case, an increase in the remaining

resist height and feature width in the center can be observed using PEC. Further the erosion at the outer edge of the frame is reduced, even tough it is hard to see in Fig. 2.4. Summarizing it can be stated that this particular pattern would not be possible to fabricate without PEC. The reduced $\varepsilon_{1,z,\mathrm{norm}}$ background in the center of the pattern for the PE corrected case (compare Fig. 2.3(c)+(d)) caused the substantial increase in the expected resist thickness (see Fig. 2.4(a)+(b)) Additionally, the increased steepness of the $\varepsilon_{1,z,\mathrm{norm}}$ profile at the pattern edge (black arrows in Fig. 2.3(c)+(d)) will improve the pattern fidelity, since the profile steepness describes the amount of dose needed to shift the pattern edge a certain distance.

2.2. Base dose determination

To relate the PEC to a real sample covered with resist it is necessary to take the resist sensitivity into account. This is realized by multiplying the DF map generated by PEC with the base dose D_B. D_B is the amount of charge per area needed in conjunction with the DF map to modify the resist enough to achieve a resist mask which is as close as possible to the design.

My colleague Bengt Nilsson and I compared the needed dose D_m to achieve a defined resist step height in a positive tone resist for different materials while measuring contrast curves. Furthermore we calculated the amount of energy an average injected electron deposits in the investigated resist slice $E_{1,z}$ for those materials and observed the correlation:

$$E_{1,z}\, D_m = \text{const.} \tag{2.6}$$

$E_{1,z}$ can be calculated by shell integration of the PSF_z extracted for the particular resist slice:

$$E_{1,z} = 2\pi\, t_{\mathrm{bin}} \int_r \mathrm{PSF}_z(r)\, r\, \mathrm{d}r. \tag{2.7}$$

t_{bin} is the thickness of the resist slice used for extracting the PSF_z as explained in the beginning of section 2.1. The relation stated in Eqn. (2.6) is true if the exact same process is used and only the substrate material is exchanged [34].

Using our observation, a process property called intrinsic exposure $\mathcal{E}_{z,\mathrm{in}}$ can be defined:

$$\mathcal{E}_{z,\mathrm{in}} = D_m\, \varepsilon_{1,z,\mathrm{inf}}. \tag{2.8}$$

$\varepsilon_{1,z,\mathrm{inf}}$ is the deposited energy density in the center of an infinite pattern. $\mathcal{E}_{z,\mathrm{in}}$ can be understood as the exposure needed to modify the investigated resist

slice enough to be developed, without any contribution from the substrate, for certain process conditions. In reverse conclusion this allows us to calculate the dose needed to modify the resist when transferring a well studied process to a different substrate material. The only needed ingredients are the PSF_zs simulated for the both material stacks and D_m for the well-studied substrate.

In principle the dose D_m to achieve the desired step height could be used as a D_B for fabricating areas with a constant resist thickness. The choice of the D_m is not limited to the conditions we chose to study the $\mathcal{E}_{z,\mathrm{in}}$ it can be any type of process dependent dose. For example the base dose $D_{B,\mathrm{GaAs}}$ needed on a GaAs substrate for a process transfered from a Si substrate could be estimated by:

$$\begin{aligned} D_{B,\mathrm{GaAs}}\,\varepsilon_{1,z,\mathrm{inf,GaAs}} &= D_{B,\mathrm{Si}}\,\varepsilon_{1,z,\mathrm{inf,Si}} \\ D_{B,\mathrm{GaAs}} &= D_{B,\mathrm{Si}}\frac{\varepsilon_{1,z,\mathrm{inf,Si}}}{\varepsilon_{1,z,\mathrm{inf,GaAs}}} \end{aligned} \tag{2.9}$$

Here it is important to use $\varepsilon_{1,z,\mathrm{inf}}$ instead of $\varepsilon_{1,z,\mathrm{norm,inf}}$, which would use a normalized $\mathrm{PSF}_{z,\mathrm{norm}}$. By normalizing the PSF_z the magnitude of the deposited energy density is lost, however the spreading is conserved. The magnitude of the deposited energy density is important when a new D_B on a different substrate is calculated. However, if the same process is studied on the same substrate just for different patterns or correction, as done for the resist height prediction in Fig. 2.4, the $\varepsilon_{1,z,\mathrm{norm}}(x,y)$ can be used. For the resist thickness prediction the simulated $\mathcal{E}_{z,\mathrm{norm}}(x,y)$ in conjunction to the contrast curve is important as explained in the last section.

D_B for clearing the resist can be defined and determined using different approaches, depending on the used algorithm for calculating the DFs for the PEC. Two common approaches are the - already mentioned - large area dose to clear (LADTC), that is for example used as base dose by the software PROXECCO from Vistec Electron Beam GmbH, and dose to size (DTS) used by the correction software BEAMER from GenISys GmbH. Both definitions of D_B and possible methods to determine them experimentally will be explained in the next sections assuming a positive tone resist. Additionally the relation between the two different types of base doses will be investigated.

2.2.1. Large area dose to clear

One method to measure D_B is using a contrast curve. As explained in section 2.1 to measure a contrast curve a large pattern is exposed, keeping the dose constant over the whole exposed area. As pattern for example a square or a disk larger than the influence range of the PSF_z can be used. Using such a large pattern

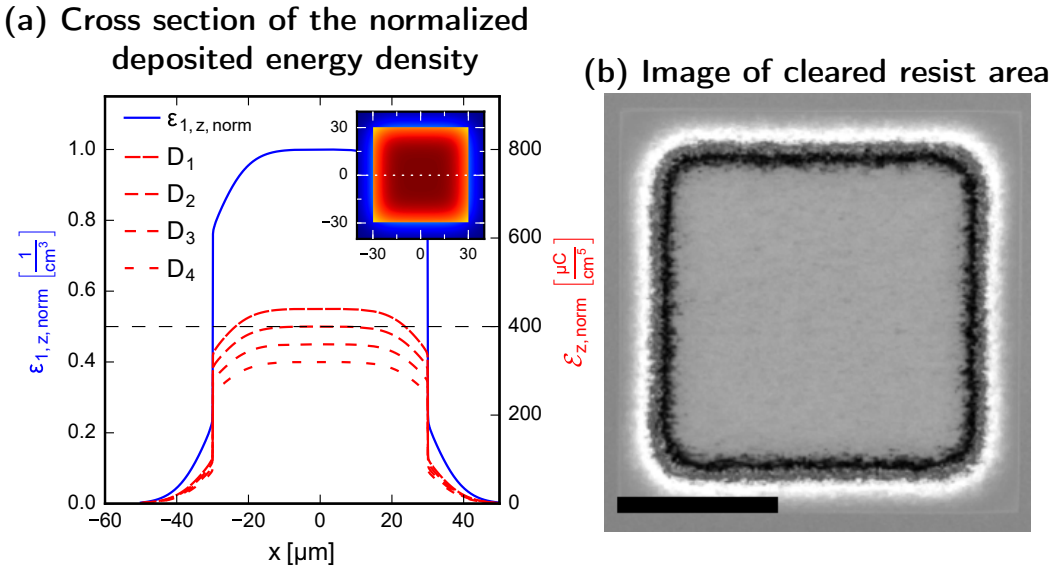

Figure 2.5.: (a)Profile of the $\varepsilon_{1,z,\mathrm{norm}}(x, y = 0)$ (blue line) along the dashed white line shown in the insert presenting a large square used to determine the LADTC. In the cross section the development threshold is indicated by the black dashed line. The red dashed line shows the simulated normalized exposure $\mathcal{E}_{z,\mathrm{norm}}$ for the doses from D_1 =440 µC cm^{-2} to D_4 =320 µC cm^{-2} in steps of ΔD =40 µC cm^{-2}. D_2 =400 µC cm^{-2} corresponds to the LADTC(b) Image of a large square exposed and developed to determine the LADTC. The black scale bar corresponds to 100 µm

assures that the whole influence range of the PE is covered. $\varepsilon_{1,z,\mathrm{norm}}(x, y = 0)$ in the resist increases from the edge to the center as presented in Fig. 2.5(a). The insert shows the 2D $\varepsilon_{1,z,\mathrm{norm}}(x, y)$ and the blue curve is extracted along the white dashed line. If a pattern larger than the influence range of the PSF$_z$ is exposed the $\varepsilon_{1,z,\mathrm{norm}}$ in the center of the pattern saturates, since the backscattering contribution is constant in that region.

If the local $\mathcal{E}_{z,\mathrm{norm}}$ is high enough the resist can be developed completely, which is indicated by the development threshold (black dashed line) in Fig. 2.5(a). The red dashed lines indicates the simulated $\mathcal{E}_{z,\mathrm{norm}}$ for different dose D applied to the pattern. For D_2 =400 µC cm^{-2} the development threshold is reached, therefore D_2 corresponds to the LADTC.

In Fig. 2.5(b) a large exposed and developed square with a completely cleared center is shown. At the periphery of the pattern remaining resist can

be observed. In practice the corresponding dose would be chosen to be the LADTC. Since the LADTC is material and process dependent quantity it has to be measured for any combination of resist, substrate and developer conditions separately.

A major drawback of the LADTC method is that the exposed area has to be fairly large since the influence range of the backscattered electrons is large, especially for silicon substrates. The pattern dimensions are usually the influence range of the PE plus tens of micron - depending on the measurement technique - to achieve stable measurement conditions. Depending on the resist, the developer and further process conditions, the exposure of large areas will take long time. Additionally the pattern is exposed several times with increasing dose in order to determine the lowest dose achieving a resist-free center of the pattern after development. In principle it would be sufficient to use an optical microscope to investigate the exposed areas searching for the first cleared center. Unfortunately, residuals can be missed if they are too small. Therefore a measurement of the resist profile after development is the preferred approach to determine the LADTC.

To determine the resist profile reliably experience is needed and it is usually a time consuming process which is another major drawback. The measurement difficulties are partly caused by the resist properties. For an ideal resist a step-like edge profile after development would be expected. Since the resist development process in reality does not comply to the development threshold model the resist profile after development is smeared out. In literature the resist property quantifying the grade of the blur is defined as the contrast. Thereby a high contrast means a more step-like behavior. A finite contrast results in a partly developed resist even if the development threshold is not crossed and causes the transition region between the undeveloped pattern edge and the cleared center in Fig. 2.5(b).

Resist profilometry Measuring the resist profile reliably is a challenge due to the material properties of the partly exposed resist, however it is the preferred method, since additional information for the resist contrast can be acquired simultaneously. In principal it is possible to measure the resist profile optically or mechanically, whereupon the mechanical methods can be divided in tactile or contact mode and non-contact mode.

Optical profilometers use a variety of different approaches to measure the sample profile. One possibility is to use a confocal microscope [44] and to measure the sample either slice by slice in z-direction or in line traces while keeping the surface in focus. Using confocal microscopy allows to achieve

sub-20 nm resolution in z-direction. The high resolution requires a high NA, which limits the field of view. By choosing the correct objective the ratio between resolution and investigated area can be optimized.

Another type of optical profilometers use Mirau objectives [45]. The built-in interferometer allows to observe Newton rings on the sample surface if it is in focus. By changing the distance between objective and sample the height difference between surfaces can be measured. With this technique it is possible to measure the part of the sample covered by the field of view of the objective in one single measurement, which is an advantage compared to serial profilometric methods. Unfortunately resists are usually semitransparent and therefore interferences can occur since the resist and the substrate form a Fabry-Pérot interferometer. These interferences can lead to measurement errors.

Due to the high lateral resolution of the optical profilometric methods the exposed region for determining the LADTC is only limited by the PE. Since the measurement should be conducted in the regime of constant deposited energy density (see Fig. 2.5(a)) the exposed area has to be larger than the measured area. Thus the edge length of the exposed pattern has to be at least one PSF_z diameter. Additionally, as a rule of thumb the inspected resist feature should be four times larger than the probe. The probe size however is small and can be neglected. Assuming a large focus spot size of 5 µm and a PSF_z diameter of 200 µm for resist on Si the pattern should be larger than 220 µm. Another advantage is that the measurement is non-invasive, so the resist profile is not altered during the measurement if the wavelength is matched to the absorption spectrum of the resist. Depending on the resist, the refractive index of the resist can be different from the not exposed. In order to avoid issues caused by the change in reflectivity a thin metal layer could be deposited on top of the resist.

Tactile profilometers use a pointed stylus with an apex radius of a few micron which is scanned over the sample maintaining the hard contact. Avoiding resist scratching is the main challenge for this tactile measurement method. During the development the resist is softened and therefore especially in the transition region between almost undeveloped to fully developed, scratching can occur. In this critical transition region, scratching can influence the measurement result or even make the data inconclusive. Besides from scratching and a medium measurement speed the tactile profilometry does not suffer from the change of the refractive index caused be the exposure. The exposed area has to be fairly large in order to get a sufficient area with a constant resist height, however the difference to the optical methods is modest. Using our rule of thumb the exposed pattern for resist on Si and an apex radius of 12.5 µm should have a minimum size of approximately 250 µm.

method	+	-	pattern size
optical (confocal)	small probe size non-invasive no tip degradation	slow expensive	$\approx 10\,\mu m + d_{PSF_z}$
optical (Mirau)	fast non-invasive no tip degradation	interference effect expensive	$\leq 20\,\mu m + d_{PSF_z}$
tactile contact mode	fast no interference effect no tip degradation	resist scratching invasive	$\approx 50\,\mu m + d_{PSF_z}$
NCM-AFM	small probe size no interference effect non-invasive	slow tip degradation non-linear scanner	$\approx 10\,\mu m + d_{PSF_z}$

Table 2.1.: Comparison of profilometric methods for resist thickness measurements

The third possibility to measure the resist profile is to use non-contact mode atomic force microscopy (NCM-AFM). Thereby influences from optical effects or resist scratching can be avoided, however the softened resist can be deformed elastically. Further AFM measurements are slow and the probe can degrade or be destroyed during the measurement. Since the measured height is orders of magnitudes larger than the tip oscillations, slow scans are required to prevent tip damage. Furthermore the exposed pattern still has to be as large as the diameter of the PSF_z plus a few micron to create a flat region to measure. Therefore the exposed region for resist on Si has to be approximately 210 µm. AFM are often not optimized to scan such large areas causing measurement uncertainties due to non-linearities arising by the deflected scanner piezo.

In table 2.1 the comparison of the three resist profilometry approaches is summarized, showing their advantages, disadvantages and the required pattern size for measuring the LADTC.

After studying all the challenges of using the LADTC as base dose the positive aspects of measuring it have to be mentioned, too. The exposed feature size for the LADTC is a few 100 µm and the thickness of commonly used EBL resists is below 1 µm. The resulting aspect ratio prevents developer saturation effects, which can for example occur inside narrow features. The development rate can be reduced in narrow trenches due to insufficient liquid exchange.

2.2.2. Dose to size

A different approach to measure the base dose is to determine the dose to size (DTS). To measure the DTS a special pattern, which is not PE corrected, is exposed with different doses. The DTS equals the dose needed to achieve exactly the designed pattern dimensions after the development. A proper DTS measurement pattern would be a line grating. For the pattern design several guidelines should be considered:

- cover a large area to achieve a homogeneous $\varepsilon_{1,z,\mathrm{norm}}(x, y)$ background in the measurement area.
- avoid line and gap widths smaller than the resist thickness, to prevent resist collapse and to ease the analysis. Especially narrow deep trenches in the resist are difficult to examine in an SEM. Due to increased secondary electron (SE) generation at pattern edge or cloaking inside narrow trenches the measurement results can be influenced. Furthermore it is challenging to judge if the resist is removed completely in trenches.
- design pattern features in the sub-micron range if possible. Since SEM measurements are using image analysis methods, the uncertainty of the measurement is tied to the image resolution and the field of view.
- optimum in most cases is a grating with equal line and gap width in the range of a few hundred-nm.

In Fig. 2.6 an SEM image of a developed resist example pattern is shown. It consists of a large array of 200 nm wide lines and spaces in a 200 nm thick resist. The total covered area is 250 µm.

The DTS can be used as the base dose for PEC carried out by BEAMER. As mentioned before, their corrections assume a threshold model to predict the resist dimension after the development and assume a development threshold of 0.5 for their PEC. This threshold means that in order to be able to remove the resist in the exposed area at a certain position the $\varepsilon_{1,z,\mathrm{norm}}(x, y)$ in the resist has to be at least 0.5. Additionally a resist with an infinite contrast is assumed. The resist would be removed completely during development if the threshold is crossed in a certain region and would stay completely if not. The transition would be step-like, independent of the difference in the $\varepsilon_{1,z,\mathrm{norm}}$ at the threshold. In case the threshold is reached exactly at the feature boarder, the pattern dimension will be as designed independent of the difference in $\varepsilon_{1,z,\mathrm{norm}}$ between in- and outside of the designed pattern boundaries. Unfortunately, such a digital resist is not existing.

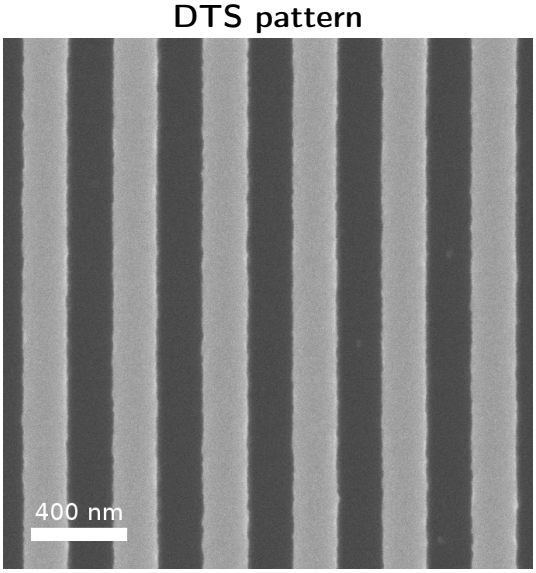

Figure 2.6.: SEM micrograph of a section from a typical DTS structure in developed resist, consisting of a 50 % duty cycle line grating with 400 nm pitch. The pattern was exposed in 200 nm thick ARP6200 from AllResist GmbH.

All resists have a certain dose range where they change from 100 % to 0 % resist thickness or vise versa. The smaller this range is the better the resist contrast is. Therefore, using a resist with a poor contrast demands a steep transition of $\varepsilon_{1,z,\mathrm{norm}}(x,y)$ at the pattern edge. If the transition is too shallow the resulting resist profile will cause problems during lift-off or etching. Actually, the resist contrast and the steepness of the transition at the pattern edge define the process window. Therefore the difference of $\varepsilon_{1,z,\mathrm{norm}}(x,y)$ in and outside the pattern matters to achieve a properly defined pattern edge. A proper pattern edge eases the measurement in the SEM, since the lines can be determined more reliably.

2.2.3. Relation between LADTC and DTS

As described the LADTC and the DTS can be used as base doses for two different PEC approaches. In the following section their relation will be investigated. In order to explain this relation I will compare the $\varepsilon_{1,z,\mathrm{norm}}(x,y)$ for both approaches. As pattern a large square pattern and a line grating are used. The large square can be used to calculate both LADTC and DTS.

However, for the determination of the DTS commonly a line grating is used, since it is less challenging to measure the size of a grating line than a large square with the required precision. For all calculations a flood exposure of the pattern is assumed instead of filling it with shots. As mentioned in the beginning of section 2.1 this is an acceptable approximation since in many cases the distance between the individual shots is chosen to cover the whole exposed area considering the beam diameter. For the comparison the PSF_z will be approximated by two superimposed Gaussian distributions the so-called double-Gaussian model.

Double-Gaussian model In the double-Gaussian model, one Gaussian distribution is related to the forward scattering and one to the backscattering. The PSF_z can be approximated by the double Gaussian $\mathrm{PSF}_{\mathrm{DG}}$ described by the following equations:

$$\mathrm{PSF}_{\mathrm{DG}}(r) = \frac{1}{1+\eta} g_\alpha(r) + \frac{\eta}{1+\eta} g_\beta(r) \tag{2.10}$$

$$\text{with } g_\sigma(r) = \frac{1}{\pi\sigma^2} \exp\left(-\frac{r^2}{\sigma^2}\right). \tag{2.11}$$

r is the radial distance to the point of injection (POI) of the electrons and η is a weighting factor between forward and backscattering. α and β are defined by the influence range of forward and backscattering. The normalization in Eqn. (2.11) is chosen to achieve a rotation volume of 1 enclosed by $g_\sigma(r)$ and the x,y-plane. As a result calculating the rotation volume of Eqn. (2.10) around the z-axis results in the normalized volume 1. This normalization is the same as used for $\varepsilon_{1,z,\mathrm{norm}}(x,y)$. The rotation volume corresponds to the $\varepsilon_{1,z,\mathrm{norm}}$ in the resist in the center of an infinitely large exposed area.

Exposing a resist on silicon the forward scattering FWHM α would be in the range of a few nanometers whereas the backscattering FWHM $\beta \approx 60\,\mu\mathrm{m}$ and $\eta \approx 0.6$. Therefore every exposure shot causes a high and very localized energy deposition as well as a low and far spread one. If a pattern is exposed the forward scattering broadens it by a few nanometer and the backscattering causes a large area $\varepsilon_{1,z,\mathrm{norm}}(x,z)$ background biasing of the resist.

The double-Gaussian model is frequently used because it allows to calculate the convolution of pattern and $\mathrm{PSF}_{\mathrm{DG}}$ analytically. Since the influence range of forward and backscattering is orders of magnitude different the double-Gaussian model allows a separation of the effects simplifying calculations. Therefore the double-Gaussian model is used for the comparison of LADTC and DTS, too. Unfortunately, this model has limits, especially for materials having

substantial mid-range contributions. For example the mid-range effects in III-V semiconductors or substrates covered with thicker gold layers cannot be modeled by the double-Gaussian model [40].

LADTC For the comparison of LADTC and DTS it is essential to remember: the resist needs the same exposure $\mathcal{E}_{z,\mathrm{norm}}(x,y)$ to be modified locally independent from the pattern (see beginning of section 2.2). The dose D has to be used to compensates the background caused by the proximity effect originating from the substrate and depending on the pattern density ($\varepsilon_{1,z,\mathrm{norm}}(x,y)$), in order to achieve the correct $\mathcal{E}_{z,\mathrm{norm}}(x,y)$ in the resist. The following considerations are based on the square pattern for LADTC as described in section 2.2.1 as well as the line grating pattern for the determination of the DTS as explained in section 2.2.2. The $\mathcal{E}_{z,\mathrm{norm}}$ in the center of the LADTC pattern and the $\mathcal{E}_{z,\mathrm{norm}}$ at the feature edges in the center of the DTS pattern have to be identical when they are developed properly.

For the comparison the $\varepsilon_{1,\mathrm{DG,norm}}(x,y)$ is calculated according to Eqn. (2.4) using a double-Gaussian PSF ($\mathrm{PSF_{DG}}$) for every position $P(x,y)$.

$$\begin{aligned}\varepsilon_{1,\mathrm{DG,norm}}(x,y) &= \big(p(x,y)\cdot \mathrm{DF}(x,y)\big) * \mathrm{PSF_{DG}}(r)\\ &= p(x,y) * \mathrm{PSF_{DG}}(r)\\ &= \int_{\upsilon}\int_{\tau} p(\tau,\upsilon)\,\mathrm{PSF_{DG}}\left(\sqrt{(x-\tau)^2+(y-\upsilon)^2}\right)\mathrm{d}\tau\,\mathrm{d}\upsilon. \quad (2.12)\end{aligned}$$

A constant dose distribution $\mathrm{DF}(x,y)=1$ is assumed and the convolution of pattern and $\mathrm{PSF_{DG}}$ is written in its integral form.

In the case of the LADTC, $\varepsilon_{1,\mathrm{DG,norm}}(x,y)$ can be calculated following Eqn. (2.12) and using a pattern $p_{\mathrm{LADTC}}(x,y)$ consisting of a large square with an edge length a with $a > 3\beta$ as shown in Fig. 2.7. The red area is p_{LADTC}. For all positions inside the pattern $p_{\mathrm{LADTC}}(x_{in},y_{in}) = 1$ and for the rest $p_{\mathrm{LADTC}}(x_{out},y_{out}) = 0$. The blue semitransparent region depicts the influence range of the $\mathrm{PSF_{DG}}(-a/2,-a/2)$ at $P(-a/2,-a/2)$. The deposited energy density at the position $P(x_n,y_n)$ (indicated by the red cross in Fig. 2.7) originated by exposing $P(-a/2,-a/2)$ is defined by $\mathrm{PSF_{DG}}(\sqrt{(x_n-\tau)^2+(y_n-\upsilon)^2})$, using the vector $\overrightarrow{(\tau,\upsilon)}$ depicted in Fig. 2.7. By inserting Eqn. (2.10) in (2.12) and applying the pattern definition p_{LADTC}, $\varepsilon_{1,\mathrm{DG,norm}}(0,0)$ reduces to $\varepsilon_{\mathrm{LADTC}}$ the normalized deposited energy density in the center of a large pattern:

$$\varepsilon_{\mathrm{LADTC}} = \int_{-\frac{a}{2}}^{\frac{a}{2}}\int_{-\frac{a}{2}}^{\frac{a}{2}} \frac{1}{1+\eta} g_\alpha\left(\sqrt{\tau^2+\upsilon^2}\right) + \frac{\eta}{1+\eta} g_\beta\left(\sqrt{\tau^2+\upsilon^2}\right)\mathrm{d}\tau\,\mathrm{d}\upsilon. \quad (2.13)$$

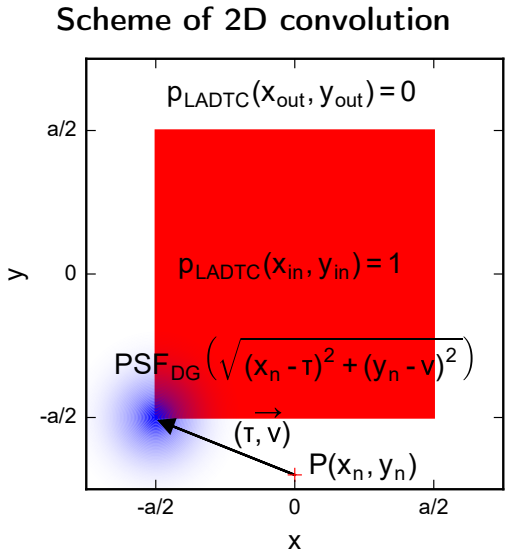

Figure 2.7.: Scheme of a 2D convolution of a double-Gaussian $\mathrm{PSF}_{\mathrm{DG}}$ with a large square pattern. The pattern is presented by the red square and the blue semi-transparent area is the double-Gaussian $\mathrm{PSF}_{\mathrm{DG}}$. The observation point $P(x_n, y_n)$ is marked with a red cross and the vector $\overrightarrow{\tau, v}$ indicating the distance from P to the lower left corner of the pattern is presented by a black arrow.

After inserting Eqn. (2.11) into Eqn. (2.13) and since $a \gg \beta \gg \alpha > 0$, Eqn. (2.13) can be reduced to:

$$\begin{aligned} \varepsilon_{\mathrm{LADTC}} &= \frac{1}{1+\eta} 1 + \frac{\eta}{1+\eta} 1 \\ &= 1. \end{aligned} \tag{2.14}$$

The normalized deposited energy density in the LADTC case $\varepsilon_{\mathrm{LADTC}} = 1$. This result is expected since the normalization of the $\mathrm{PSF}_{\mathrm{DG}}$ was chosen to be one for the LADTC case. Exposing a large pattern with a fixed dose the center region receives the maximum energy density possible. As a result, in a pattern, which is not PE corrected, the normalized deposited energy density will never exceed $\varepsilon_{\mathrm{LADTC}}$.

DTS for a large square Now I am repeating the same analysis however for the position $P(-\frac{a}{2}, 0)$. $\varepsilon_{1,\mathrm{DG,norm}}(-\frac{a}{2}, 0)$ for the pattern p_{LADTC} is defined as the normalized deposited energy density at the edge of a large square $\varepsilon_{\mathrm{DTS,S}}$:

$$\varepsilon_{\mathrm{DTS,S}} = \int_{-\frac{a}{2}}^{\frac{a}{2}} \int_{-\frac{a}{2}}^{\frac{a}{2}} \frac{1}{1+\eta} g_\alpha \left(\sqrt{\left(-\frac{a}{2} - \tau\right)^2 + \upsilon^2} \right) + \\ + \frac{\eta}{1+\eta} g_\beta \left(\sqrt{\left(-\frac{a}{2} - \tau\right)^2 + \upsilon^2} \right) \mathrm{d}\tau \, \mathrm{d}\upsilon. \quad (2.15)$$

The integration of both Gaussian g_α and g_β is explained by:

$$\int_{-\frac{a}{2}}^{\frac{a}{2}} \int_{-\frac{a}{2}}^{\frac{a}{2}} g_\sigma \left(\sqrt{\left(-\frac{a}{2} - \tau\right)^2 + \upsilon^2} \right) = \frac{1}{2} \operatorname{erf}\left(\frac{a}{2\sigma}\right) \operatorname{erf}\left(\frac{a}{\sigma}\right) \quad (2.16)$$

$$\text{for } a \gg \sigma :$$

$$\frac{1}{2} \operatorname{erf}\left(\frac{a}{2\sigma}\right) \operatorname{erf}\left(\frac{a}{\sigma}\right) = \frac{1}{2}. \quad (2.17)$$

Using this result, Eqn. (2.15) can be reduced to:

$$\varepsilon_{\mathrm{DTS,S}} = \frac{1}{1+\eta}\frac{1}{2} + \frac{\eta}{1+\eta}\frac{1}{2} \quad (2.18)$$
$$= \frac{1}{2}$$

The normalized deposited energy density at the edge of a large square ($\varepsilon_{\mathrm{DTS,S}}$) is therefore half of the normalized deposited energy density in the center ($\varepsilon_{\mathrm{LADTC}}$) as illustrated in Fig. 2.8. Since the same exposure $\mathcal{E}_{z,\mathrm{norm}}(x, y)$ is needed to modify the resist enough to dissolve it completely, the dose needed to achieve the designed width of a large square ($\mathrm{DTS_S}$) is twice as high as the dose needed to clear only the center. Therefore in Fig. 2.5(b) the edge of the square is not cleared while the resist in the center is dissolved.

DTS for a line grating In the grating case the pattern edge of a line from the center is investigated. The grating has equal line and gap width, it can be described as follows:

$$p_{\mathrm{DTS}}(x, y) = \sum_{n=0}^{a/(2l)} \left(\Theta\left(x + \frac{-a + (4n-1)l}{2}\right) \Theta\left(-x + \frac{-a + (4n+1)l}{2}\right) \right. \\ \left. \Theta\left(y + \frac{a}{2}\right) \Theta\left(-y + \frac{a}{2}\right) \right). \quad (2.19)$$

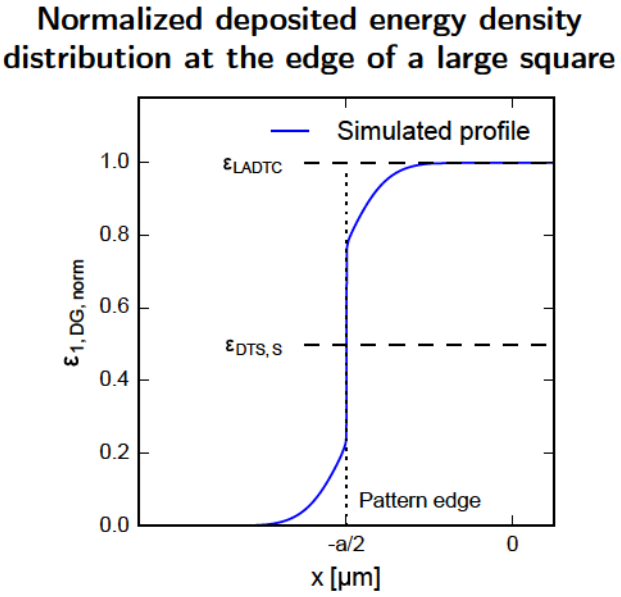

Figure 2.8.: Simulated normalized deposited energy density distribution at the edge of a large square emphasizing the relation of $\varepsilon_{\mathrm{DTS,S}}$ and $\varepsilon_{\mathrm{LADTC}}$.

Θ is the Heaviside step function and l is the line and the gap width, further $l > 3\alpha$. a is the edge length of the pattern bounding box, with $a > 3\beta$. In order to calculate the normalized deposited energy density $\varepsilon_{\mathrm{DTS,G}}$ at the line edge in the center of the pattern ($P(-\frac{l}{2}, 0)$), p_{DTS} (Eqn. (2.19)) is applied to $\varepsilon_{1,\mathrm{DG,norm}}$ (Eqn.(2.12)).

$$\varepsilon_{\mathrm{DTS,G}} = \sum_{n=0}^{a/(2l)} \int_{-\frac{a}{2}}^{\frac{a}{2}} \int_{\frac{a+(4n\ \ 1)l}{2}}^{\frac{a+(4n+1)l}{2}} \mathrm{PSF}_{\mathrm{DG}} \left(\sqrt{\left(-\frac{l}{2} - \tau \right)^2 + \upsilon^2} \right) \mathrm{d}\tau\, \mathrm{d}\upsilon. \quad (2.20)$$

In order to ease the calculation the forward scattering and the backscattering are investigated independently. Focusing on the forward scattering ($l \gg \alpha$) the neighboring lines are not contributing to the deposited energy density originating from the forward scattering, therefore applying Eqn. (2.10) in (2.20)

and focusing on g_α $\varepsilon_{\mathrm{DTS,G}}$ becomes:

$$\begin{aligned}\varepsilon_{\mathrm{DTS,G}} &= \int_{-\frac{a}{2}}^{\frac{a}{2}} \int_{-\frac{l}{2}}^{\frac{l}{2}} \frac{1}{1+\eta}\, g_\alpha \left(\sqrt{\left(-\frac{l}{2}-\tau\right)^2 + \upsilon^2} \right) \mathrm{d}\tau\, \mathrm{d}\upsilon + \cdots \\ &= \frac{1}{1+\eta}\frac{1}{2}\,\mathrm{erf}\left(\frac{a}{2\alpha}\right)\mathrm{erf}\left(\frac{l}{\alpha}\right) + \cdots . \end{aligned} \tag{2.21}$$

Since $a \gg l \gg \alpha > 0$ Eqn. (2.21) reduces to:

$$\varepsilon_{\mathrm{DTS,G}} = \frac{1}{1+\eta}\,\frac{1}{2} + \cdots . \tag{2.22}$$

Investigating the backscattering contributions to the $\varepsilon_{\mathrm{DTS,G}}$, Eqn. (2.20) by applying Eqn. (2.10) and focusing on g_β $\varepsilon_{\mathrm{DTS,G}}$ becomes:

$$\begin{aligned}\varepsilon_{\mathrm{DTS,G}} = \cdots + \sum_{n=0}^{a/(2l)} \int_{-\frac{a}{2}}^{\frac{a}{2}} \int_{\frac{a+(4n\ \ 1)l}{2}}^{\frac{a+(4n+1)l}{2}} \frac{1}{1+\eta} \\ g_\beta \left(\sqrt{\left(-\frac{l}{2}-\tau\right)^2 + \upsilon^2} \right) \mathrm{d}\tau\, \mathrm{d}\upsilon \\ = \cdots + \frac{\eta}{1+\eta} \sum_{n=0}^{a/2l} \left(\frac{1}{2}\,\mathrm{erf}\left(\frac{a}{2\beta}\right)\left(\mathrm{erf}\left(\frac{a-4ln}{2\beta}\right) - \right.\right. \\ \left.\left. - \mathrm{erf}\left(\frac{a-2l-4ln}{2\beta}\right)\right)\right). \end{aligned} \tag{2.23}$$

For $a > 3\beta$ and $\beta \gg l > 0$ (2.23) reduces to:

$$\varepsilon_{\mathrm{DTS,G}} = \cdots + \frac{\eta}{1+\eta}\,\frac{1}{2}. \tag{2.24}$$

By summing up Eqn. (2.22) and Eqn. (2.24) $\varepsilon_{\mathrm{DTS,G}}$ can be determined as:

$$\begin{aligned}\varepsilon_{\mathrm{DTS,G}} &= \frac{1}{1+\eta}\,\frac{1}{2} + \frac{\eta}{1+\eta}\,\frac{1}{2}. \\ &= \frac{1}{2} \end{aligned} \tag{2.25}$$

Comparing $\varepsilon_{\mathrm{LADTC}}$ with $\varepsilon_{\mathrm{DTS,G}}$ it can be observed that the deposited energy density in the center of a large square is twice as high as in a grating with 50% duty cycle, if both patterns are exposed using the same substrate and process.

Remembering my statement from the beginning, that a certain resist always requires the same exposure $\mathcal{E}_{z,\mathrm{norm}}(x, y)$ to develop properly, combined with calculation results for $\varepsilon_{\mathrm{LADTC}}$ and $\varepsilon_{\mathrm{DTS,G}}$, it can be stated, that:

$$DTS = 2\,LADTC. \tag{2.26}$$

In practice the dose ratio is lower than two. The deviation might be caused by resist properties or the quality of the PSF_z.

2.2.4. Dose test

A third common approach to determine the base dose is to:

1. PE correct the pattern
2. select the most important regions enlarged enough to get the actual background caused by the PE
3. extract the selected region from the design
4. expose the extracted pattern with a variety of base doses, a so-called dose test

By measuring the dimension of critical features the most suitable base dose can be determined. To preserve the resist bias caused by backscattering the extracted region should be enlarged by the backscattering range. For the dose test the relative dose factors (DFs) are kept constant and only the base dose is varied therefore the correction is preserved while the absolute dose values are changed.

The dose test might be the most direct way to determine the base dose, however it is specific for a certain pattern. If the full pattern is exposed, eventual process effects can be observed and compensated. Using the LADTC or the DTS as base dose is a more generic approach and yields a fundamental information about the process. This information is useful to compare resists and processes or to have a starting point for an individual process optimization. Nevertheless it is almost unavoidable to perform a dose test for high-resolution processes. Determining the correct base dose is not trivial due to the mentioned measurement issues using profilometers or SEM and the multiplicity of influences.

2.3. Simulated point spread function

After discussing the different ways of measuring the base dose it is important to investigate how PSF_zs can be determined. Experimental methods to compare and validate PSF_zs by exposing special patterns and measuring their dose-dependent dimensions, as well as different simulation packages are investigated.

Simulation is a cost-effective and fast way to determine PSFs. By simulating a PSF it is possible to study the complete influence range of the PE in the extracted PSF_z. Especially the short-range characteristic of the PSF_z is difficult to investigate experimentally since it is in the range of the resist resolution limit. Therefore the amount of available data for validating simulation results is limited which leads to deviating results depending on the used simulation package. Commonly, the Monte-Carlo method is used to simulate the electron scattering inside the material stack. From the Monte-Carlo simulation (MCS) results the PSF can be calculated and the PSF_zs can be extracted. The Monte-Carlo method is a numerical approach based on random numbers, often used to solve integrals numerically or to simulate systems with many coupled degrees of freedom in physics. Applications can be found in the fields of fluids, strongly coupled solids, disordered materials or our field of interest - i.e. electron scattering [26, 46].

In the studied Monte-Carlo simulation packages random numbers are used for several purposes. When the electron hits the sample surface it is necessary to decide if an elastic or inelastic scattering event will take place. This decision is based on the scattering cross section depending on the material properties and the energy of the injected electron. Thereafter several identities are calculated depending on the interaction type, for example, the energy loss, the generation of secondary particles, like electrons, photons or positrons, the direction and mean free path of the primary electron after interaction. These steps are repeated until the energy of the primary electron drops beneath a defined threshold. The simulation results depend on the used package, since the implemented physical effects as well as the implementation itself can be different. Since all these decisions and calculations are based on probabilities a sophisticated random number generator is needed and the naming "Monte-Carlo Method" becomes plausible.

The individual MCS packages have to make assumptions and approximations in order to be fast and to be viable. This has however consequences for the area of validity. For example, the exposed material is often assumed to be amorphous and therefore all effects based on the mono-crystalline nature of materials are neglected. For example, channeling or Bragg reflection can not be considered in the simulated PSF. Limitations are not only arising from compromises

which have to be made however also from the physical models, for example the scattering cross sections the package relies on. These cross sections for all the elements and many materials can be extracted from sophisticated databases which are based on experimental results or can be calculated using the latter. For more complex materials like the resists used in EBL the number of available experimental scattering cross sections is limited. Especially organic resist materials are problematic due to their complex structure and often unknown chemical composition. If the chemical composition is know an effective medium approximation is used to calculate the scattering cross section.

In the following section I am comparing two MCS packages used for simulating PSF_zs. Parts of that section were published in the journal "Microelectronic Engineering" [31]. The theoretical comparison of the MCS packages, the presented PSF_zs and the discussion of results are based on a close cooperation with Prof. Karl E. Hoffmann, Hochschule Rosenheim. However the experimental validation of the differences observed in the simulated PSF_zs is solely my work. To measure the quality of the PSF_zs I exposed and processed PE corrected test patterns. The exposures were done using 100 keV electrons and the fabrication was repeated using different substrates. The quality of the PSF_zs was judged by analyzing the properties of the fabricated structures. In the following section of my thesis two MCS packages will be compared providing different PSF_zs and fabrication results. We attribute the observed deviation to the difference in the treatment of secondary electrons.

2.3.1. Comparing Monte-Carlo simulation tools

The used MCS packages assume an electron beam with an infinitely small diameter with a certain energy which is injected into a material stack. They calculate the energy-loss of the injected electrons due to their interaction with the material with spatial resolution. The PSF_z can be extracted from the information about the energy stored in the resist layer during the scattering events. One investigated Monte Carlo package is called SceletonX-v2011 which treats secondary electrons (SEs) by using the Continuous Slowing Down Approximation (CSDA) [47]. It assumes angular deflections originating only from elastic scattering and summarizes all energy loss processes by the Bethe equation [48] to a continuous energy loss. The simulation of detailed scattering trajectories for SEs is disregarded. These simplifications reduce the complexity of the package and decrease the computation time. In contrast, the other investigated package called Penelope-v2008 uses the Detailed Atomic Cross Sections method (DACS) referring to Garvey and Green [49]. It simulates the following types of scattering events individually: elastic collisions, inelastic

collisions with excitation and ionization as well as bremsstrahlung and plasmon excitation. This package also includes the generation and tracing of SEs, photons and positrons in the substrate and resist. MCS packages using DACS need sophisticated scattering cross sections and top-quality trajectory tracing methods to provide reliable results. The computation time for a single primary electron simulated with a MCS package using DACS can be several times longer than for a package using CSDA.

In the first approximation, PSF_zs are often described by the in section 2.2.3 explained double-Gaussian model. The PSF_z is thereby approximated by a superposition of two Gaussian functions: One considers the energy deposition originating from forward-scattered electrons and the other accounts for contributions from backscattering of electrons. Forward scattering occurs mainly in the resist and backscattering can be attributed mostly to events in the substrate. Cui [29] noted that the generation of fast SEs effectively broadens the PSF_z in the mid-range. To verify this effect, we compare the PSF_zs simulated with SceletonX-v2011 which does not trace the SEs, and with PENELOPE [26] which includes the tracing of SEs.[1]

Fig. 2.9(a) shows a comparison of PSF_zs simulated using 100 keV electrons injected in 400 nm PMMA on a GaAs substrate. The PSF_zs are in fair agreement at long-range distances, however a substantial deviation at mid-range distances between 10 nm and 2 µm can be observed. By repeating the same simulation using Penelope however with a disabled SE generation and tracing module the SceletonX-v2011 PSF_z could be reproduced in good agreement. To switch off the SE generation implies that no propagating electron is generated. The energy transfered during an inelastic scattering event, previously allowing a SE generation, however is preserved and will be stored using the CSDA method. The good agreement of the PSF_z simulated with PENELOPE, neglecting the SE generation, and SceletonX-v2011 suggests that the SEs cause the mid-range deviation.

In Fig. 2.9(b) the influence of different substrate materials for the PSF_zs is shown. This time a 100 nm thick PMMA layer on GaAs or Si is studied, as well as the effect of SE generation and tracing on both substrates. If the SEs are neglected the PSF_zs indeed can be described by a double-Gaussian model. The low scattering probabilities of the high energy primary electrons in the resist cause a beam broadening of only a few nanometers however it depends on the resist thickness. Since PENELOPE calculates every injected

[1] As a consequence of this work a newer version of SceletonX-v2011 was released including SE generation and tracing as well as GenISys GmbH started the development of there own Monte-Carlo simulator called TRACER.

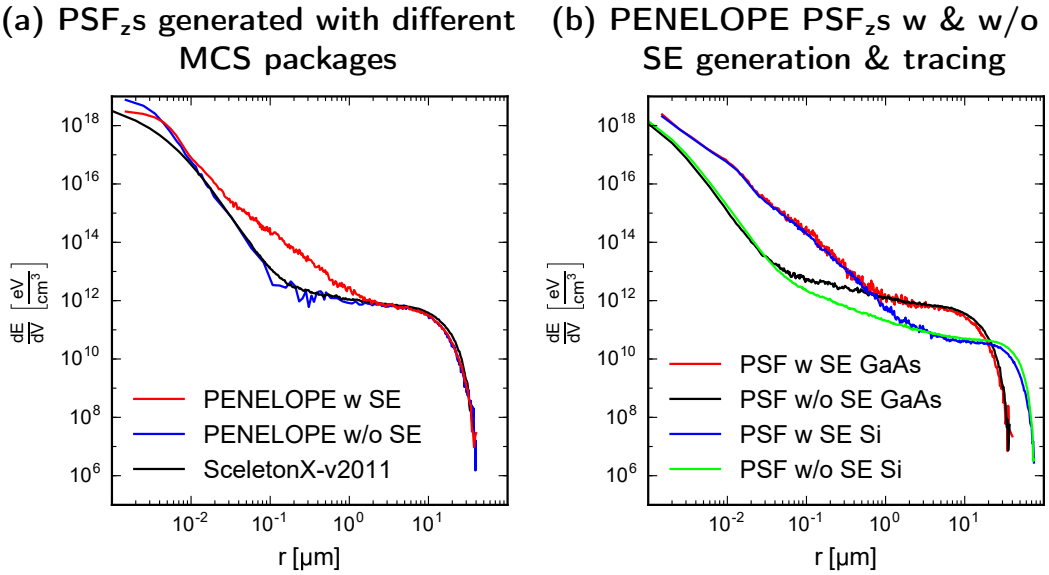

Figure 2.9.: (a) PSF$_z$s determined at $z = 225\,\text{nm}$ and for a virtual layer thickness $t_{\text{bin}} = 50\,\text{nm}$ of a 400 nm PMMA resist layer on a GaAs substrate, calculated with different MCS packages. (b) PSF$_z$s calculated considering the SE in different ways. The PSF$_z$s are determined at $z = 50\,\text{nm}$ and for a virtual layer thickness $t_{\text{bin}} = 20\,\text{nm}$ of 100 nm PMMA resist on GaAs and Si substrate, respectively.

electron independently, assuming the same starting conditions for each electron, effects like substrate charging and local heating are neglected. Therefore the simulated electrons can only interact with the material which they pass and the beam broadening is substrate independent. The effect of this simplification can be observed in the PSF$_z$, too. All PSF$_z$s simulated with the same resist thickness and type on different substrates show similar trends as presented in Fig. 2.9(b). The results neglecting SE generation and tracing however show one to two orders of magnitude lower amount of deposited energy density in the short- and mid-range regime than those considering SE generation and tracing. Additionally, the energy an average electron could deposit in the investigated resist slice $E_{1,z}$ for the PSF$_z$s simulated considering SE generation and tracing is higher. $E_{1,z}$ can be calculated by a shell integration of the PSF$_z$ (see Eqn. (2.7))As explained in section 2.2, the product of $E_{1,z}$ and the base dose D_B is constant. Therefore differences in $E_{1,z}$ could cause a different base dose as well as deviating proximity effect correction (PEC) results for the same material stack depending on the used MCS package.

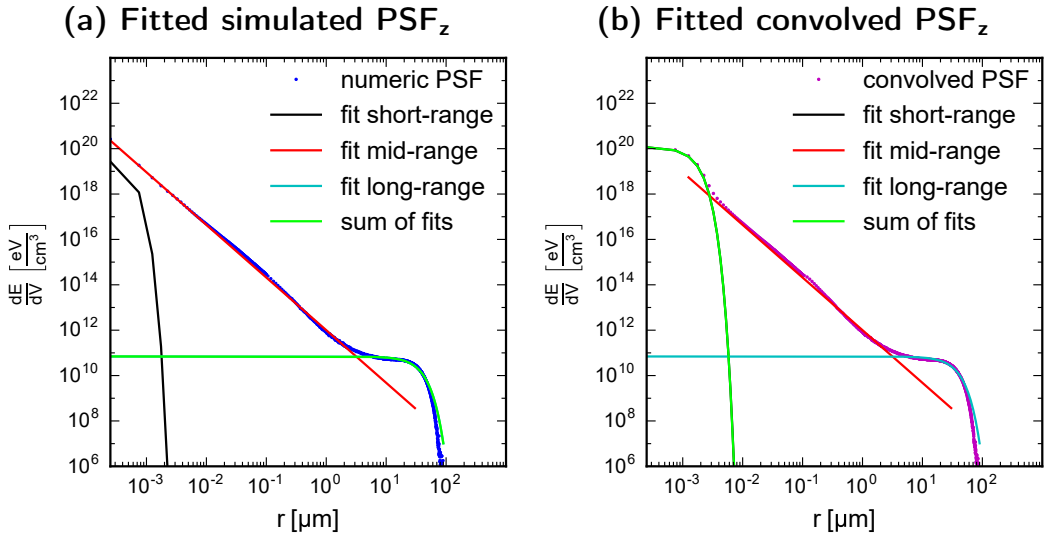

Figure 2.10.: Two fitted PSF$_z$s simulated by PENELOPE. (a) double logarithmic plot of a PSF$_z$ (blue dots) simulated for 100 nm PMMA on Si extracted at 50 nm from substrate surface and a layer thickness of 20 nm. The PSF$_z$ is fitted (green line) by combining two Gaussian distributions (black and aquamarine line) and a power function (red line). (b) the same PSF$_z$ convolved with FWHM 2 nm Gaussian beam fitted by the same combination of functions.

Comparing two PSF$_z$s simulated with the same MCS package (either neglecting or considering SE generation and tracing) show identical results in the short-range regime even for different substrate materials (see Fig. 2.9(b)). These results emphasize the reliability of the used MCS package, since the resist type and thickness are identical. First when the backscattering from the substrate starts to dominate the energy deposition a clear differentiation of the PSF$_z$s can be observed. Comparing the shape of the PSF$_z$s presented in Fig. 2.9 it can be observed that the PSF$_z$s simulated considering SE generation cannot be described by a double-Gaussian model anymore.

2.3.2. Interpretation of the PSF simulation results

The PSF$_z$ in Fig. 2.10 (blue dots) is simulated by PENELOPE assuming a 80 nm thick PMMA resist layer on bulk silicon. Before starting the approximation with different functions, it is important to keep the rotation volume around the energy-density-axis constant to maintain energy conservation.

The aquamarine curve in Fig. 2.10(a) demonstrates that the long-range contribution of the backscattered electrons can be fitted by a Gaussian distribution. The red curve visualizes, that the mid-range contribution of the SEs can be described by a power function. Since the power function fits the PSF_z well down to the sub-10 nm-range (see red curve in Fig. 2.10(a)) it seems like the fast SEs contribute considerably in the short-range region, too. The scattering probability of the high energetic injected primary electron in the resist is quite low due to the low density and atomic numbers of the elements forming the resist. Especially for thin resists the contribution from forward scattered electrons is rather low, as it can be observed from the black curve in Fig. 2.10(a).

For the simulation the electron beam is assumed to have an infinitely small diameter. In reality, the beam diameter is in the range from a few to several tens of nanometers and this beam broadening has to be convolved into the PSF_z. The convolution of the PSF_z and the real beam results in a domination by the beam shape in the range from the point of injection (POI) to the power function takes over, as shown by the magenta data in Fig. 2.10(b). Since the beam profile influences the PSF_z only in the short-range, the shape of the PSF_z in the mid- and long-range is conserved. Therefore the same power function and Gaussian distribution can be used to fit these parts of the PSF_z. The region in close proximity to the POI is assumed to have a Gaussian shape and can be approximated by the same function used for the convolution. Although the shape of the simulated and not convolved PSF_z close to the POI is less important for the PEC, the deposited dose in this range is nevertheless not negligible and has to be taken into account. The EBL system I am using assumes, like many others, a Gaussian beam profile.

As mentioned before the shape of the simulated PSF_z considering SE generation is not sufficiently approximated by a combination of two Gaussian distributions. However, it is possible to fit these PSF_zs using a sum of two Gaussian distributions and a power function. Therefore, the energy density contribution in the mid-range caused by the SEs might be described by a power function.

Even though the double-Gaussian approximation of the PSF_z is not correct it has advantages as mentioned before. For example the convolution of a Heaviside step function (Θ) and a Gaussian distribution have the Gaussian error function as an analytical result. This advantage is for example exploited in the section 2.2.3 for the calculation of the normalized deposited energy density. Using Θ to describe the edges of the design pattern and having a PSF_z consisting only of Gaussians leads immediately to an analytical result for the dose distribution after the exposure.

The convolution itself can be transformed into a multiplication in the Fourier space by exploiting the convolution theorem [50]. For the practical implementation of a PEC this is an important fact since the Fourier transformation of a simulated PSF_z and an arbitrary pattern, followed by a multiplication and transformation back into real space can be implemented fast. However calculating the analytical result by using the double-Gaussian model can be even faster and less resource demanding than performing three Fourier transformations. For the analytical approach it is important to approximate the PSF_z in such a way that the amount of deposited energy is equal to the energy that is calculated using the numeric PSF_z. If the energy conservation is not fulfilled, the PEC will return incorrect DFs and the correction will be inaccurate.

2.3.3. Experimental validation

After having discussed the contribution of SEs to the PSF_z theoretically, the question remains whether SEs influence the exposure result. In order to investigate this I designed two test patterns and processed them. These patterns are especially designed to be very sensitive to the mid-range proximity effect, between 10 nm and 2 µm, since their feature and gap sizes are in this particular range. The PEC is done by pattern fracturing and relative dose assignment using the software BEAMER. I investigated two different PEC proposals based on two PSF_zs: one is obtained using PENELOPE including SE generation and tracing, the other one using SceletonX-v2011 without SE tracing. All patterns were corrected with both PSF_zs and processed to analyze the difference.

Pattern The first test pattern consists of an array of square groups. Each group is composed of equally sized squares, arranged on a grid with equal distances. From group to group along one array axis the square size decreases from 300 nm to 40 nm and along the other array axis the gap between the squares increases from 40 nm to 400 nm, as illustrated in Fig. 2.11. The distance between the square groups in the array has been chosen to be 50 µm, to reduce the influence from backscattered electrons between neighboring groups. After performing PEC, the pattern is fractured and relative DFs are allocated to these pattern fragments. For the exposure these relative DFs are multiplied by the base dose. The whole array pattern is exposed several times at different positions on the substrate with increasing base doses. After development, metal deposition and lift-off the resulting patterns are evaluated. In order to characterize the result, I define a quantity called the base dose discrepancy. It is determined by the difference between the base dose necessary to obtain at least one of the squares in the whole array and the base dose needed to obtain

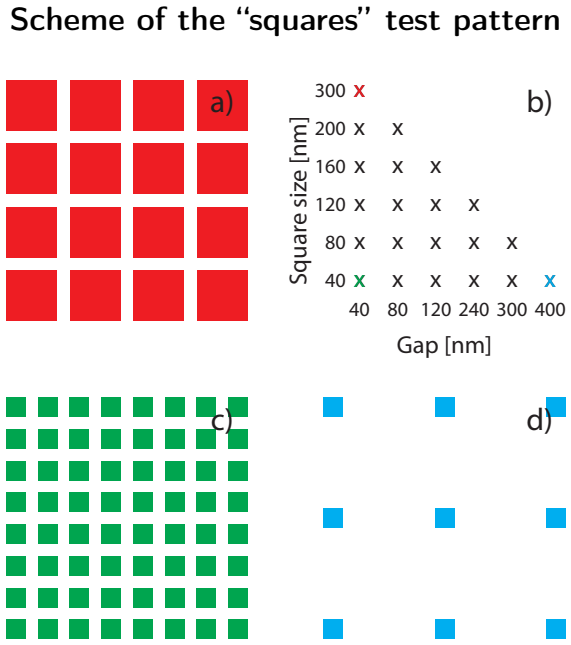

Figure 2.11.: Scheme of the "squares" test pattern used to determine the base dose discrepancy for PSF_zs calculated by different MCS packages. The pattern consists of groups of squares with different sizes and gaps as displayed in (b). (a), (c) and (d) three distinct examples of these squares groups.

all squares in all groups. One expects that the square group with smallest and most separated squares need a higher dose, than the larger less separated ones. Therefore the base dose discrepancy is an excellent measure for the PEC and the underlying PSF_z, as an ideal PEC should lead to a base dose discrepancy of zero. This means that the same base dose is required for the whole pattern array, independent of size and spacing of the squares. In literature the term base dose uniformity is often used as an antonym to base dose discrepancy. A high uniformity corresponds to a low discrepancy and vice versa. Using the correct PSF_z and a proper PEC algorithm a high base dose uniformity can be achieved.

The second pattern is designed to allow an estimation of the base dose uniformity at first glance. It consists of 10 µm long stripes with decreasing width from 300 nm to 5 nm in steps of 5 nm, spaced by increasing gaps from 5 nm to 300 nm. The described pattern design is shown in Fig. 2.12 and will

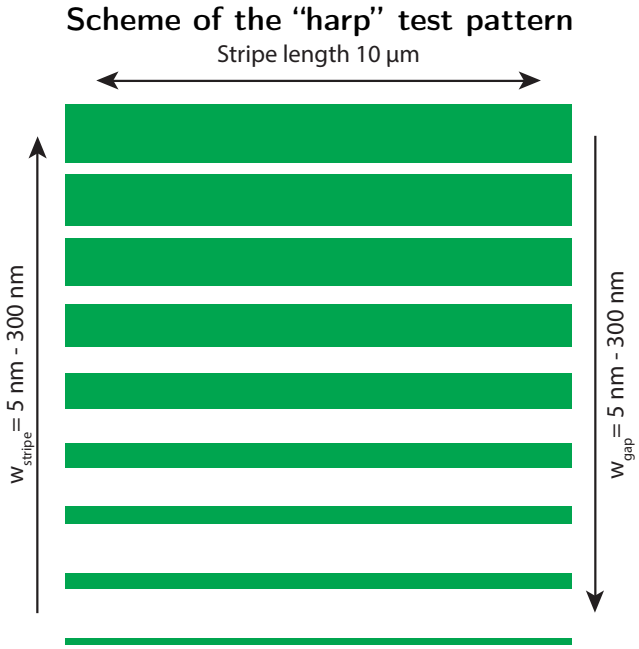

Figure 2.12.: Scheme of the "harp" test pattern consisting of exposed stripes (green) and spaces with decreasing stripe width and increasing spacing. This pattern allows an estimation of the dose uniformity at first glance, by counting the number of properly processed stripes and spaces.

be referred to as "harp pattern". Exposing thin stripes and narrow gaps at the same time is challenging. A thin stripe require a high dose compared to the thick stripes defining a narrow gap, since the contribution by the SEs is pattern density dependent. The more accurate the PSF_z is the more stripes and gaps should be resolved. Therefore a difference in the number of properly processed stripes and gaps depending on the chosen PSF_z is expected. By defining a minimum required feature size the process window can be defined using the harp pattern.

Fabrication To ensure the comparability of both experiments using the squares and the harp pattern, the patterns were processed at the same time on the same sample under equal conditions. On one sample all patterns are separated by a few tens of microns to prevent contributions from the neighboring patterns.

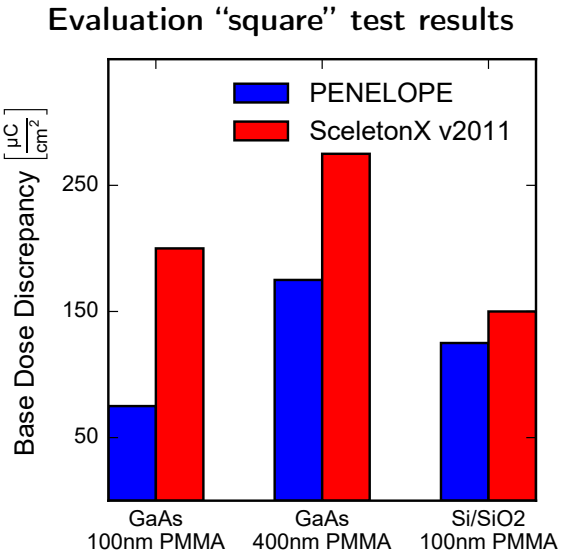

Figure 2.13.: Base dose discrepancy determined by using the squares pattern for different substrate/resist combinations. For the PEC two PSF_z were used: the blue bars illustrate the results from the PSF_z taking SE generation into account, the red ones show the results neglecting SE generation.

I investigated three different material compositions: two GaAs substrates, covered with 100 nm and 400 nm PMMA, respectively, and a Si substrate with 300 nm thermally grown SiO_2 on top, coated with 100 nm PMMA. Using PENELOPE, the PSF_zs for the Si/SiO_2 substrates are practically the same as the ones shown in Fig. 2.9(b) for Si. The exposures have been performed using 100 keV acceleration voltage. The base dose has been varied from 225 µC cm^{-2} to 950 µC cm^{-2} for the GaAs substrates and from 500 µC cm^{-2} to 1200 µC cm^{-2} for the Si/SiO_2 substrate in steps of 25 µC cm^{-2}. After the exposure the resist was developed using MIBK:IPA 1:3 (volume ratio) for 10 s and rinsed with IPA for 30 s. To transfer the pattern from the resist to the substrate, 10 nm AuPd was evaporated on the samples followed by lift-off.

Evaluation The sample inspection was done semi-automatically inspected with a scanning electron microscope (Zeiss Merlin). The resulting image data were computationally post-processed to ease the comparison.

Analyzing the pattern consisting of squares shows a nearly equal base dose is needed to develop the 300 nm squares, independent of the PSF_z used for

the PEC. Investigating further the smaller squares, at the transition from 80 nm to 40 nm size, the patterns corrected with the PSF_z simulated without SE generation and tracing need a much higher base dose increase than the ones corrected with a PSF_z taking the SE generation into account. This difference translates directly to a higher base dose discrepancy for the PSF_z without considering SEs (see Fig. 2.13). On the GaAs substrate a remarkable difference in base dose discrepancy for PEC with and without SE simulation can be observed. The advantage of the PENELOPE PSF_z, considering the SE generation and tracing, is most pronounced for GaAs covered with 100 nm PMMA. In our test this material combination results in the smallest base dose discrepancy. For the Si/SiO_2 substrates, no significant improvement is achieved as the base dose discrepancy is almost the same for both PSF_zs. This can be interpreted as mid-range effects as the SE generation have no pronounced impact on the exposure result for Si/SiO_2 substrates. The correction quality for these substrate materials is more dependent on the correct ratio between forward and backward scattering. The result shows that both simulation packages calculate this ratio equally well.

For the harp pattern, the difference in pattern quality between the PSF_zs used for the PEC is more pronounced on the GaAs than on the Si/SiO_2 substrate. I observe a more clearly processed harp pattern if the design was corrected with a PSF_z considering SE generation. As shown in Fig. 2.14 for GaAs covered with 100 nm PMMA exposed using a base dose of $550\,\mu C\,cm^{-2}$ two smaller gaps and two thinner stripes can be observed if the PSF_z is accounting for SE generation and tracing. The structure corrected with the PSF_z without SEs seems to be already overdosed, as the small gaps are closed. However, for an equal base dose, thinner stripes seem to be underexposed, since they are not transferred to the sample.

These results show that SE generation and tracing has a significant influence on the process results and cannot be neglected. Especially for small features and gaps of less than 100 nm in the same pattern the consideration of SEs is necessary to achieve better dose uniformity. However the effect is more pronounced for GaAs than for the Si/SiO_2 substrate.

Using the harp pattern, the process window is a measure to compare the PSF_zs and PEC algorithms. Based on the designed size of stripes and gaps, I define a process window for the harp pattern. In Fig. 2.15 the thinnest stripe (blue) and the narrowest gap (red) which were intact after metal lift-off are plotted for different doses. The shown results were processed on a GaAs sample coated with 100 nm PMMA. The process window (black marker) will be defined as those doses where the thinnest properly fabricated stripe is maximum 30 nm wide and the narrowest gap has to be 30 nm or smaller. These conditions are

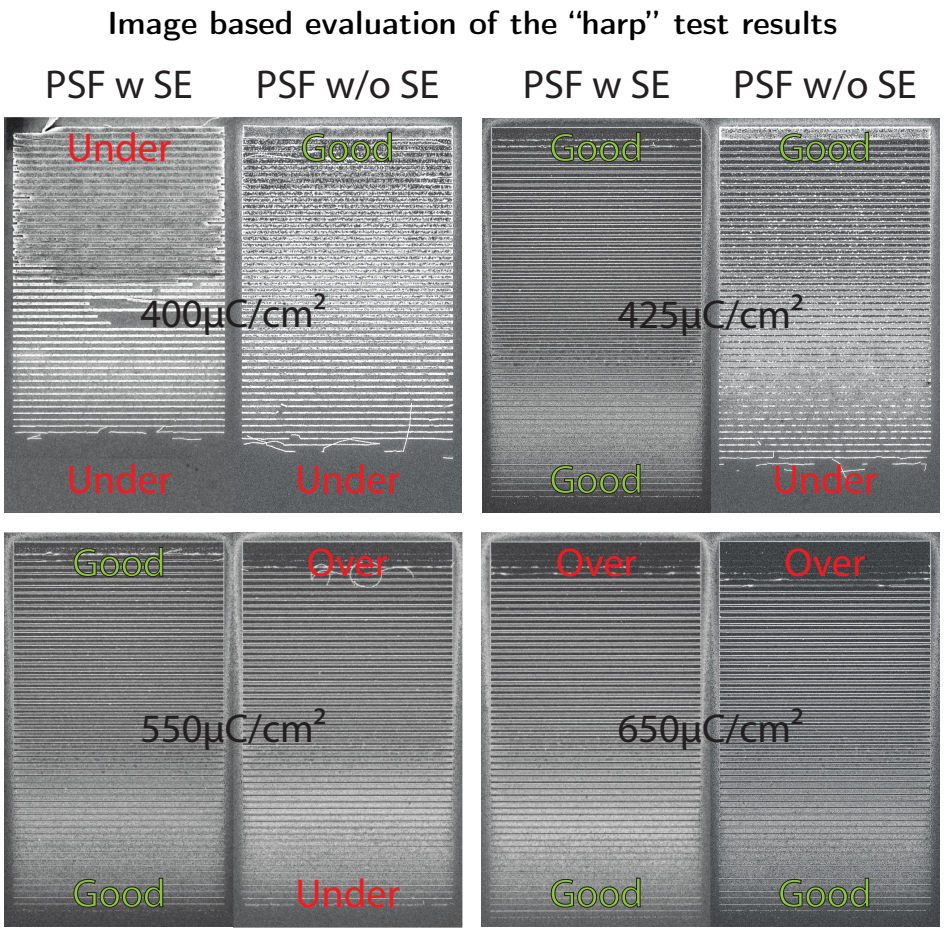

Figure 2.14.: SEM micrographs of processed harp test patterns after metal lift-off. The patterns were PE corrected using different PSF_zs and base doses for 100 nm PMMA on GaAs. The quality of the correction is determined by investigating how small continuous gaps and stripes can be fabricated. In the images under- or overexposed regions are marked with the red tags "Under" or "Over" respectively. Properly fabricated areas are marked with a green tag "Good". The analysis shows a better uniformity and larger process window for the PE corrected patterns using the PSF_z with SE generation and tracing.

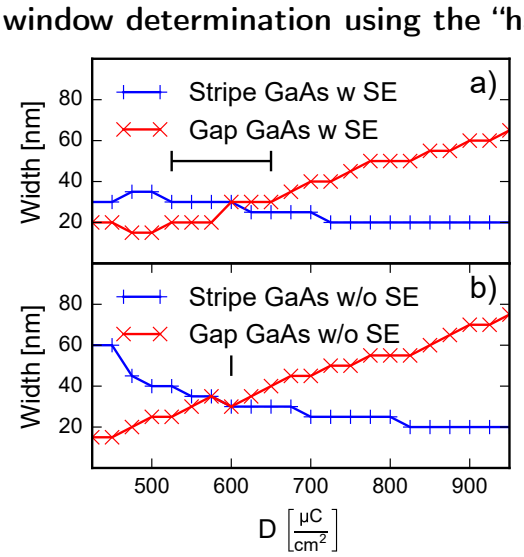

Figure 2.15.: Design width of the smallest properly fabricated stripe and gap for increasing base doses using a PSF_z (a) considering, (b) neglecting SE generations for the PEC. The process window for 30 nm designed stripe and gap is indicated as black range bar.

fulfilled for the harps corrected using a PSF_z considering SE generation over a wide range of doses from 525 µC cm^{-2} to 650 µC cm^{-2}. The patterns corrected using a PSF_z neglecting SE generation and tracing fulfill the conditions only at a single dose of 600 µC cm^{-2} in the studied dose range. Following the definition of the process window a significant improvement of the process window can be observed using proximity effect corrections (PEC) based on a PSF_z considering SE generation and tracing.

2.3.4. Conclusion

We generated point spread functions (PSFs) with two different Monte-Carlo simulation (MCS) packages: PENELOPE and SceletonX-v2011, that deviate significantly in the mid-range regime, between 10 nm and 2 µm. We could attribute this deviation to the generation and tracing of secondary electrons as individual particles, which are explicitly simulated in PENELOPE. By switching off the SE generation and tracing module in PENELOPE it generates a similar PSF_z as SceletonX-v2011. I developed two test patterns for benchmarking the PSF_zs, one with squares and one with stripes of varying size and gaps.

The results clearly show that enhanced mid-range corrections of the PSF_z used by PEC improve the results on GaAs substrate. This emphasizes the significance of secondary electron generation and tracing for proper pattern processing. However, the results also indicate that the PSF_zs used for PEC are still not sufficient to ensure base dose uniformity for all patterns investigated, in particular on the Si/SiO_2 substrate, which might be due to the insulating nature of the 300 nm thick oxide layer.

2.4. Experimental PSF investigation

The determination of a PSF using Monte-Carlo simulations and extracting a PSF_z for a slice at a certain resist height is an established method. The PSF_z can be used for 2D PEC for common materials like silicon and III-V semi-conductors. For these substrate materials the validity of simulated PSF_zs was proven experimentally by different methods [27, 40, 51, 52]. The PSF_zs for less well studied and more exotic materials like sapphire or multi-layer heterostructures can be determined by simulation as well, however the experimental validation is often missing.

A number of experimental methods using different approaches to measure a PSF_z are published in literature [27, 40, 51, 52]. All common methods measure in or across the center of the exposed area, therefore these techniques are limited by the resist resolution or their exposure sensor size, rather than by the beam diameter. In the following sections a method based on a donut or ring-like pattern is discussed, which I developed to validate PSF_zs experimentally. In the center of the ring a small disk is placed and used as sensor to measure the normalized exposure $\mathcal{E}_{z,\mathrm{norm}}$.

2.4.1. Method and concept

The intention of the development of the ring-test is to validate a simulated PSF_z covering the whole spatial range described by the PSF_z. In the proof of concept described here I was able to validate a PSF_z for 100 nm resist on Si experimentally down to 160 nm radial distance from the point of injection (POI). As schematically depicted in Fig. 2.16, the exposed pattern consists of a ring (blue) and a disk (red) in the center as a rotational symmetric sensor of $\mathcal{E}_{z,\mathrm{norm}}$. Due to the PE, energy is deposited in a certain range around the POI including the center of the ring where the sensor is placed. Thus, the whole ring contributes to the normalized deposited energy density $\varepsilon_{1,z,\mathrm{norm}}$ accumulated in the center $\varepsilon_{\mathrm{ring}}$. To measure the amount of energy density deposited in the

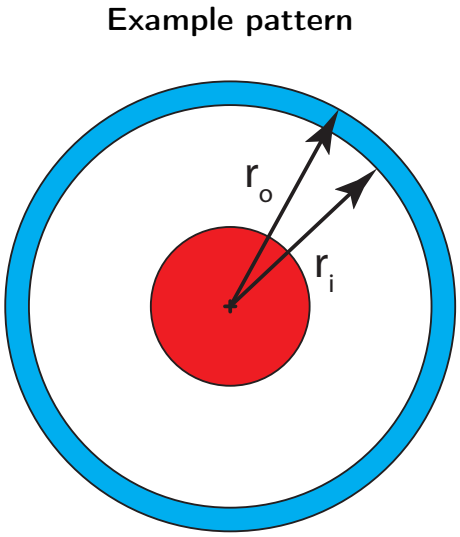

Figure 2.16.: Scheme of a ring-test example pattern. The red disk is used as a sensor to measure the energy density contributed by the blue ring. The inner radius r_i and the outer radius r_o are iterated to probe the whole PSF_z.

sensor $\varepsilon_{\mathrm{sens}}$ the whole pattern is exposed in a negative tone resist and the disk is biased with a dose high enough to achieve a thickness after development which is measurable by an atomic force microscope (AFM).

As mentioned in chapter 1 a negative resist behaves opposite to a positive resist. In the exposed regions increases the molecular weight of the molecules of the negative resist and therefore dissolves slower than the unexposed areas. Hence the exposed regions endure the development and a pattern can be created.

Additionally to the bias of the sensor the ring contributes more deposited energy density in the center causing an increased resist thickness after development compared to a free standing disk. This resist thickness difference is proportional to $\varepsilon_{\mathrm{ring}}$. In order to probe the whole PSF_z the ring radius as well as the width is varied.

The inner radius r_i and the outer radius r_o of the concentric rings are chosen to probe the whole PSF_z. To obtain a proper measurement resolution using a finite dose and to limit the time needed to expose the pattern, the outer ring radius is set to be $r_o = 1.15\ r_i$ until the ring width $w_r < 8\,\mathrm{nm}$. For $r_i \leq 40\,\mathrm{nm}$ the ring radius is fixed to $w_r = 8\,\mathrm{nm}$. Exposing rings with a small

width assures that only the intended parts of the PSF_z contribute to the $\varepsilon_{\mathrm{sens}}$. Especially in the mid- and short-range part of the PSF_z it is important to avoid a saturation of the sensor caused by an unnecessary background originating from large exposed areas. Therefore the ring width has to be small. Since the deposited energy density decreases with increasing r, I try to compensate by increasing the dose as well as increasing the ring width continuously. For example exposing a ring with $r_i \approx 43\,\mu\mathrm{m}$ and $r_o \approx 50\,\mu\mathrm{m}$ on Si contributes approximately the same $\varepsilon_{\mathrm{ring}}$ in the sensor center as a ring with a $r_i = 20\,\mathrm{nm}$ and $r_o = 28\,\mathrm{nm}$. On the other hand in the mid-range regime the contribution is substantially lower. Comparing the same small ring with another one with a $r_i \approx 1.15\,\mu\mathrm{m}$ and $r_o \approx 1.32\,\mu\mathrm{m}$ the $\varepsilon_{\mathrm{ring}}$ is 20 times lower and needs to be compensated by dose.

A similar test, which was developed in parallel by Czaplewski *et al.* [27], uses a different approach. First of all, their test pattern facilitates a cross as sensor of $\mathcal{E}_{z,\mathrm{norm}}$. This is a valid simplification if the rings are considerably larger than the cross. A second difference to my approach is the design of the ring. They keep the outer radius r_o constant and set it to a value significantly larger than the expected PSF_z radius. In order to probe the PSF_z r_i is modified and thereby the ring width as well as the exposed area.

For the determination of the $\varepsilon_{\mathrm{ring}}$ and $\varepsilon_{\mathrm{sens}}$ as well as the corresponding $\mathcal{E}_{z,\mathrm{norm},S}$ a flood exposure of the patterns is assumed. For an arbitrary pattern $\varepsilon_{1,z,\mathrm{norm}}$ can be calculated by convolving the pattern, dose factor map (DF) and the $\mathrm{PSF}_{z,\mathrm{norm}}$ according to Eqn. (2.4):

$$\begin{aligned}\varepsilon_{1,z,\mathrm{norm}}(x,y) &= \big(p(x,y)\cdot \mathrm{DF}(x,y)\big) * \mathrm{PSF}_{z,\mathrm{norm}}(r)\\ &= \int_\tau\int_\upsilon \big(p(\tau,\upsilon)\,\mathrm{DF}(\tau,\upsilon)\big)\\ &\qquad \cdot \mathrm{PSF}_{z,\mathrm{norm}}\left(\sqrt{(x-\tau)^2+(y-\upsilon)^2}\right)\,\mathrm{d}\tau\,\mathrm{d}\upsilon. \qquad (2.27)\end{aligned}$$

For a concentric ring around the point of origin O (p_{ring}), exposed with a constant DF - as in the ring-test - the normalized deposited energy density contribution $\varepsilon_{\mathrm{ring}}$ at O can be calculated using Eqn. 2.27:

$$\begin{aligned}\varepsilon_{\mathrm{ring}}(r_i,r_o) &= \int_\tau\int_\upsilon \big(p_{\mathrm{ring}}(\tau,\upsilon)\,\mathrm{DF}\big)\,\mathrm{PSF}_{z,\mathrm{norm}}\left(\sqrt{\tau^2+\upsilon^2}\right)\,\mathrm{d}\tau\,\mathrm{d}\upsilon\\ &= 2\pi\int_{r_i}^{r_o} \mathrm{DF}\;\mathrm{PSF}_{z,\mathrm{norm}}(\varrho)\;\varrho\,\mathrm{d}\varrho. \qquad (2.28)\end{aligned}$$

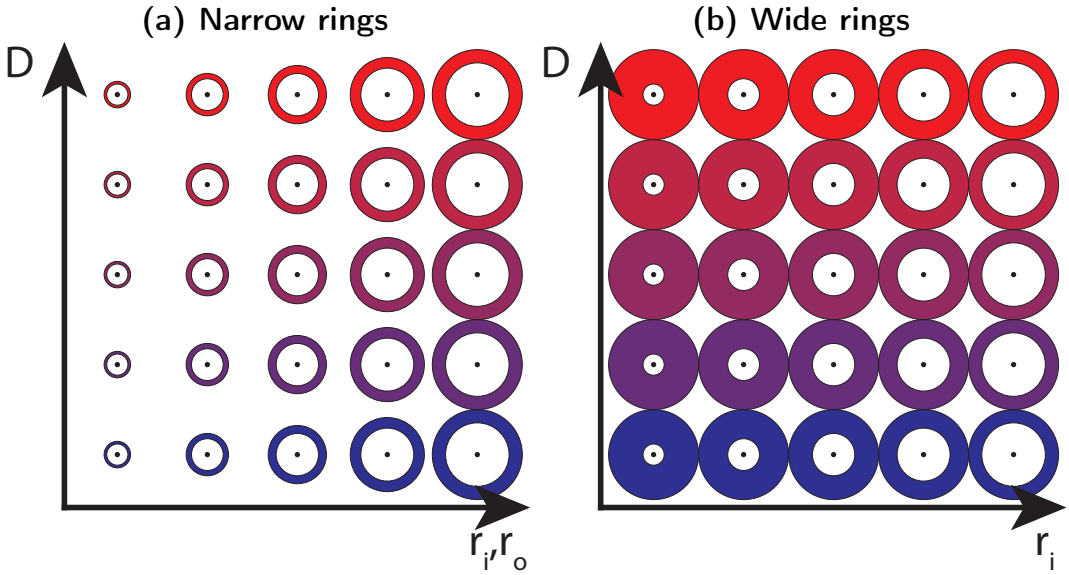

Figure 2.17.: (a) Sketch of the pattern for the narrow rings approach. Along the horizontal-axis is the inner ring radius r_i and the outer ring radius r_o increase proportionally. Along the vertical-axis is the dose increased. (b) Sketch of the pattern for the wide rings approach. While r_o is kept constant r_i is increased along the horizontal-axis. Along the vertical-axis is the dose increased. Comparing both approaches a notable difference in the exposed area for small r_i can be observed.

r_i is the inner radius and r_o is the outer radius of the exposed ring. It is important to remember that Eqn. 2.28 is a convolution and therefore describes the energy density deposited at O equivalent to an average injected electron. The $\varepsilon_{\text{sens}}$ for an isolated sensor can be calculated using Eqn. (2.28) and $r_i = 0$ and $r_o = r_S$ with r_S as the sensor radius.

The resist needs to be exposed with a certain dose D to generate a measurable result. In order to describe the modification of the resist I again use the $\mathcal{E}_{z,\text{norm}}$ (see Eqn. (2.3)). Further it is useful to predict the estimated resist thickness after development directly from the simulation results provided by BEAMER, if the resist contrast curve is known.

Due to the difference in the ring design the analysis for Czaplewski's and my approach is slightly different. All exposed areas within the PSF_z radius around the sensor influence the energy density deposited in the sensor. Exposing narrow rings, as in my approach, results in sampling of an specific part of the PSF_z

with the radius of the ring and an uncertainty dominated by the particular ring width. Each ring can be used as an independent measurement point. For the measurement a matrix of patterns is exposed in one direction r_i and r_o are increased and orthogonally the dose is varied as shown in Fig. 2.17(a). In Fig. 2.17(b) a possible scheme of the pattern matrix for Czaplewski approach is shown. In his approach r_o is kept constant while only changing r_i. This leads to a larger exposed area averaging over almost the complete PSF_z for small r_i. For the analysis measurements for different r_i have to be subtracted from each other leading to a differential analysis of the results.

The large exposed areas provoke a high deposited energy density background especially for small r_i as shown in Fig. 2.18(b). This background has to be compensated by reducing the dose applied to the ring D_{ring}. Depending on the used resist a minimum D_{ring} is required to avoid issues originating from the current stability, the pattern generator speed of the EBL system and shot noise effects due to the low number of exposing electrons [53].

Using my approach facilitating narrow rings D_{ring} is not a limiting factor. In practice both approaches could be used to measure the mid- and long-range part of the PSF_z and are equivalent.

2.4.2. Calibrated exposure sensor

In contrast to the well known Donut Test [51] this new method uses a disk as sensor to measure the influence from the exposed ring on the $\mathcal{E}_{z,\mathrm{norm},S}$ in the center of the sensor. Before the PSF_z can be studied the test system needs to be calibrated. For the calibration of the sensor I measured the contrast curve of the resist on different samples to check the reliability of my process. As described earlier, the contrast curve pattern consists of large squares exposed with a constant dose. In the center of the square a maximum in the deposited energy density is achieved. After development the resist height in the center of the pattern is related to the dose, creating a contrast curve.

Usually the resist vendors provide a contrast curve for their resists, however they are often measured for lower acceleration voltages. Further the processing conditions like environment temperature and humidity are different. Sometimes we are using different developer solutions, too. As a consequence I need to measure the contrast curve myself to be sure the data matches the conditions I am working with. Additionally the contrast curve can be used as confirmatory measurement.

Using the contrast curve it is possible to define the working point of the sensor. To ease the data analysis the working range for the sensor is chosen to be in the linear part of the contrast curve (see Fig. 2.19) of the used negative

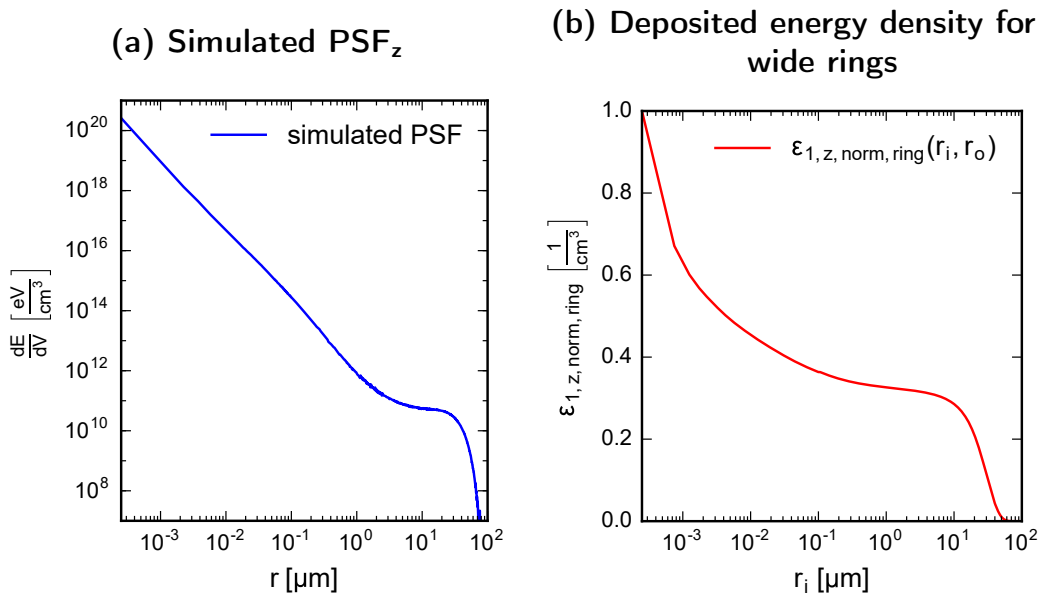

Figure 2.18.: (a) PSF$_z$ simulated for 100 nm PMMA on Si extracted at 50 nm from substrate surface and a layer thickness of 20 nm. (b) $\varepsilon_{\text{ring}}(r_i, r_o)$ calculated using Eqn. (2.28), a normalized version of (a) and $r_o = 100\,\mu\text{m}$.

resist. The normalized exposure bias $\mathcal{E}_{z,\text{norm},S,i}$ needed to achieve the initial resist thickness of the sensor h_i as well as the corresponding normalized target exposure $\mathcal{E}_{z,\text{norm},S,f}$ and thickness h_f are determined from the contrast curve. Since the $\varepsilon_{1,z,\text{norm}} = 1$ in the center of a large square, the normalized exposure is equivalent to the dose. $\mathcal{E}_{z,\text{norm},S,i} = 156\,\mu\text{C}\,\text{cm}^{-5}$ and $\mathcal{E}_{z,\text{norm},S,f} = 172\,\mu\text{C}\,\text{cm}^{-5}$ are extracted from Fig. 2.19 curve 1 using a linear fit in order to get $h_i = 20\,\text{nm}$ and $h_f = 40\,\text{nm}$. These values are originating from an earlier test sample and are used for the design of the ring-test. Curve 2 in Fig. 2.19 is the contrast curve measured on the sample used for the experimental validation discussed later in this chapter.

In the following discussion I am plotting the simulation results as $\mathcal{E}_{z,\text{norm}}$ instead of the $\varepsilon_{1,z,\text{norm}}$. Consequently, the presented results are relative to the doses used in the contrast curve. This allows a more direct comparison of the simulation results to the expected resist height after development, which is the quantity I will measure in my experiment. However, to prevent confusion I will use the term dose D only to describe the applied dose and the exposure $\mathcal{E}_{z,\text{norm}}$ to describe the deposited areal energy density in a resist slice after applying D

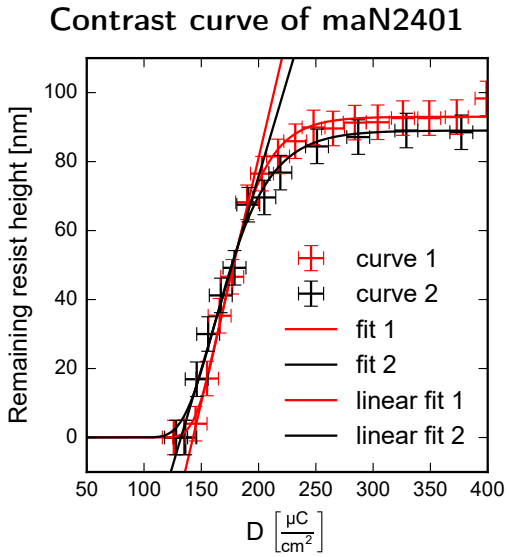

Figure 2.19.: Contrast curve of 100 nm thick negative tone resist maN2401 from micro resist technology GmbH on silicon. Measured two times on different samples and both are approximated by a sigmoidal as well as a linear fit to emphasize the agreement and the linear behavior for $20\,\mathrm{nm} \leq h \leq 60\,\mathrm{nm}$.

to the pattern.

The sensors are 2 µm in diameter and therefore small compared to the areas exposed for the contrast curve. Hence, EBL simulations, done with BEAMER, are used to determine the base dose $D_B = 232\,\mu\mathrm{C\,cm^{-2}}$ needed to achieve $\mathcal{E}_{z,\mathrm{norm},S,i}$ and h_i in the center of the sensor.

In order to get a simulation independent conversion curve the sensor is calibrated. The ring-test pattern contains a row of isolated disks exposed with different doses used for this purpose. The dose range ($220\,\mu\mathrm{C\,cm^{-2}}$ to $290\,\mu\mathrm{C\,cm^{-2}}$) is chosen to reproduce the linear part of the contrast curve taking the isolation of the sensor into account. By measuring the height of the disks after development using a Bruker Dimension ICON AFM and associating it with the corresponding $\mathcal{E}_{z,\mathrm{norm}}$, originating from the applied D, the calibration curve of the sensor is determined.

In Fig. 2.20 the expected resist thicknesses after development, which were extracted from EBL simulations using BEAMER, are compared with the measurement results. The slopes of the simulated and measured calibration curves are in good agreement, however the height for $\mathcal{E}_{z,\mathrm{norm},S,f}$ extracted from

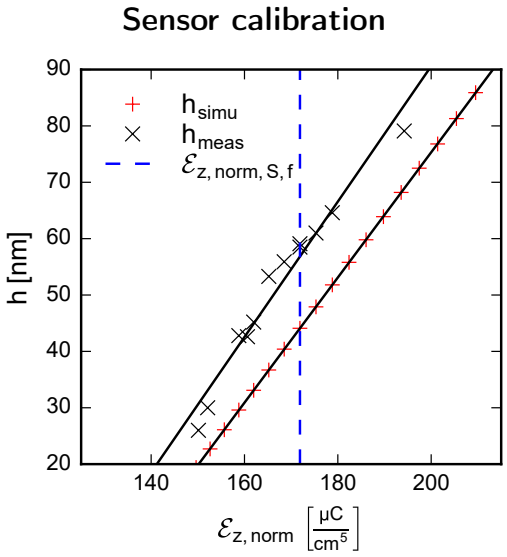

Figure 2.20.: Sensor calibration curve for 100 nm thick maN2401 on silicon comparing simulation results and measured thicknesses. The dashed blue line indicates the $\mathcal{E}_{z,\mathrm{norm},S,f}$ emphasizing the resist thickness offset of the measured sensors.

the calibration curve is $h_{f,meas} \approx 57\,\mathrm{nm}$ instead of $h_{f,simu} \approx 44\,\mathrm{nm}$.

The observed offset might be caused by processing effects. For the ring test design, curve 1 in Fig. 2.19 was used. However between designing and performing the test the contrast curve changed (see curve 2 in Fig. 2.19). Comparing the contrast curves in detail a decrease in contrast and an increase in sensitivity can be observed for curve 2. These symptoms can point towards overaged resist. Unfortunately, the used resist bottle I used was already out of shelf life time.

The 13 nm offset is no problem since the contrast curve in Fig. 2.19 shows a linear behavior of the resist between 20 nm and 70 nm. Further the sensor calibration curve is sufficiently linear around $h = 60\,\mathrm{nm}$, too (see Fig. 2.20).

2.4.3. Theoretical validation

The concept of the ring-test is to validate a simulated PSF_z, therefore a PSF_z is needed. For the theoretical as well as the experimental validation of the ring-test. A well studied and controllable test system is beneficial for the proof of concept, thus 100 nm thick maN2401 resist layer on silicon is used. Unfortunately, the

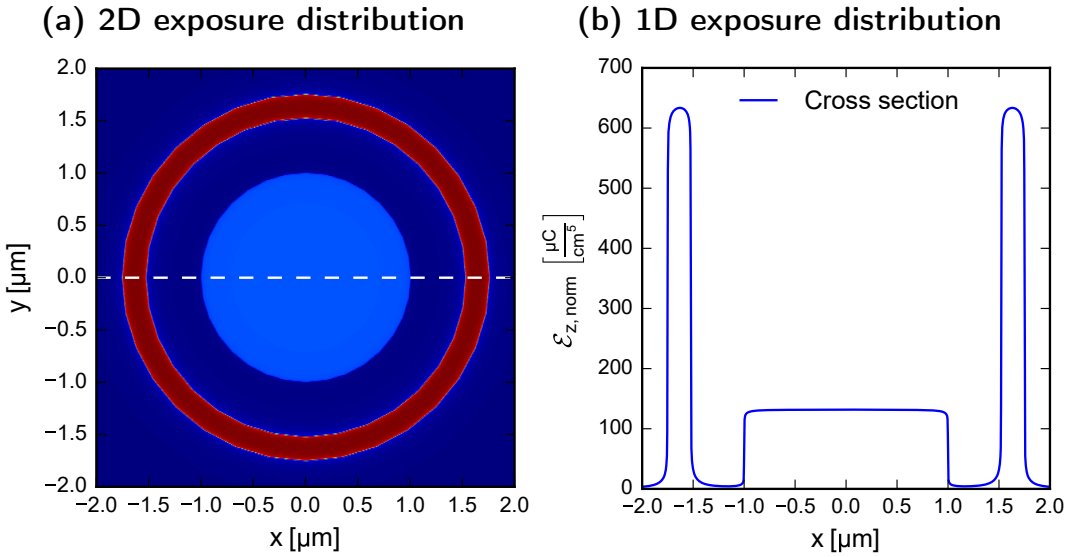

Figure 2.21.: (a) 2D exposure distribution $\mathcal{E}_{z,\mathrm{norm}}(x, y)$ of a typical sensor-ring pair. The sensor is exposed with D_B and the ring is exposed with $5D_B$. (b) Cross section $\mathcal{E}_{z,\mathrm{norm}}(x, y = 0)$ along the white dashed line in (a).

exact composition and the density of maN2401 is not published, however it is known to be novolak resin based. Due to the similarities in the molecular formulas of novolak and PMMA, PMMA is used as an approximation for maN2401. The PSF_z used for the validation was simulated using PENELOPE assuming a 100 nm thick PMMA resist layer on silicon, extracted at center of the resist. The resulting PSF_z is shown in Fig. 2.18(a).

Even tough the following validation of the ring-test method is based on simulations I will use the term expose for applying a certain dose to a pattern. In order to determine the amount of energy density deposited in the sensor originating from each individual ring, an ensemble of approximately 60 sensor-ring pairs with increasing ring diameter and width are simulated. The ring dimensions are listed in table 2.2. All sensors are 2 µm in diameter and are exposed with $D_B = 232\,\mu\mathrm{C\,cm^{-2}}$ while the rings are exposed with $D_{ring} = 5\,D_B$. The rings having smaller radii as 1 µm overlap with the sensor after exposure, however this overlap is considered during the design. In Fig. 2.21(a) the simulated 2D exposure distribution for a typical sensor-ring combination is shown. The blue curve in Fig. 2.21(b) is a cross section along the white dashed line in Fig. 2.21(a). The difference in the dose applied to sensor and

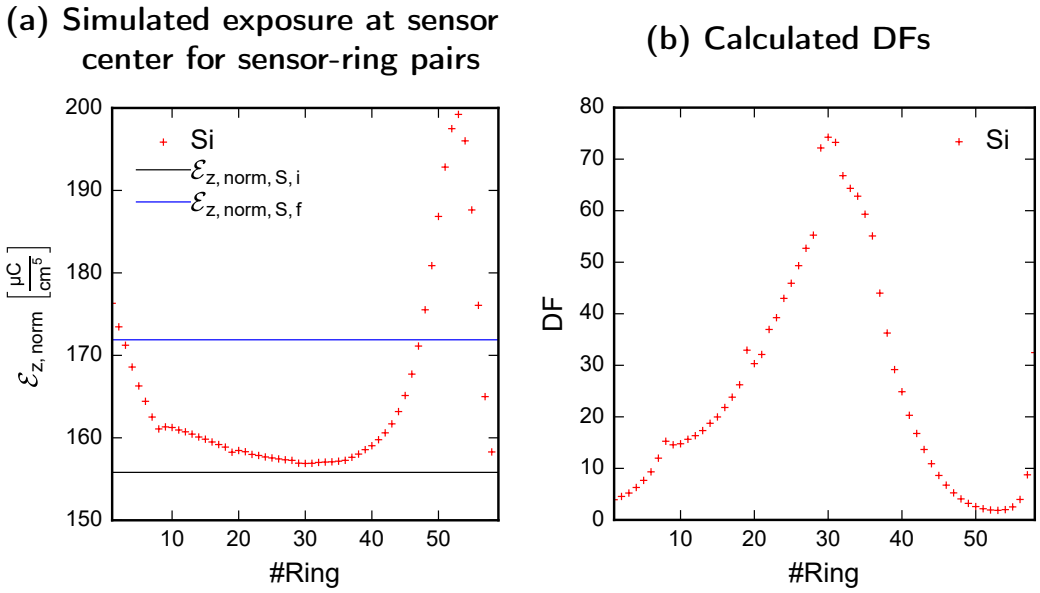

Figure 2.22.: (a) Simulated exposure at sensor center for increasing ring diameter (ring radii are listed in table 2.2). (b) Calculated DFs for each ring needed to achieve the thickness $h_f = 40\,\mathrm{nm}$ in the center of the sensor.

ring transfers into a clear difference in the energy density as well as exposure accumulated in sensor and ring. The DF of 5 between sensor and ring is chosen to minimize the influence of rounding effects caused by the simulation software, since the contribution of the rings close to ring 30 are small. All sensor-ring pairs are simulated individually and the exposure in the center of the sensor is extracted and plotted in Fig. 2.22(a). The black line indicates the bias $\mathcal{E}_{z,\mathrm{norm},S,i}$ of the sensor. The difference between the simulated exposure in the sensor center (red crosses) and the sensor bias (black line) is caused by scattered electrons originating from the rings. Additionally, the $\mathcal{E}_{z,\mathrm{norm},S,f}$ (blue line) is indicated in Fig. 2.22(a). The difference between the simulated exposure in the ring center and the $\mathcal{E}_{z,\mathrm{norm},S,f}$ is used to calculate the DFs to match the $\mathcal{E}_{z,\mathrm{norm},S,f}$ with each sensor-ring pair. The DF are calculated using the following equation:

$$\mathrm{DF} = 5\frac{\mathcal{E}_{z,\mathrm{norm},S,f} - \mathcal{E}_{z,\mathrm{norm},S,i}}{\mathcal{E}_{z,\mathrm{norm},S} - \mathcal{E}_{z,\mathrm{norm},S,i}} \tag{2.29}$$

with $\mathcal{E}_{z,\mathrm{norm},S}$ as the simulation results illustrated as red crosses in Fig. 2.22(a).

# Ring	r_i [um]	r_o [um]	# Ring	r_i [um]	r_o [um]	# Ring	r_i [um]	r_o [um]
1	0.020	0.028	21	0.327	0.376	41	5.357	6.161
2	0.023	0.031	22	0.376	0.433	42	6.161	7.085
3	0.026	0.034	23	0.433	0.498	43	7.085	8.148
4	0.030	0.038	24	0.498	0.573	44	8.148	9.370
5	0.035	0.043	25	0.573	0.658	45	9.370	10.775
6	0.040	0.048	26	0.658	0.757	46	10.775	12.392
7	0.046	0.054	27	0.757	0.871	47	12.392	14.250
8	0.053	0.061	28	0.871	1.001	48	14.250	16.388
9	0.061	0.070	29	1.001	1.152	49	16.388	18.846
10	0.070	0.081	30	1.152	1.324	50	18.846	21.673
11	0.081	0.093	31	1.324	1.523	51	21.673	24.924
12	0.093	0.107	32	1.523	1.751	52	24.924	28.663
13	0.107	0.123	33	1.751	2.014	53	28.663	32.962
14	0.123	0.142	34	2.014	2.316	54	32.962	37.906
15	0.142	0.163	35	2.316	2.664	55	37.906	43.592
16	0.163	0.187	36	2.664	3.063	56	43.592	50.131
17	0.187	0.215	37	3.063	3.522	57	50.131	57.651
18	0.215	0.248	38	3.522	4.051	58	57.651	66.299
19	0.248	0.285	39	4.051	4.658	59	66.299	76.243
20	0.285	0.327	40	4.658	5.357	60	76.243	87.680

Table 2.2.: List of inner r_i and outer r_o radii of the used rings.

All DFs calculated using Eqn. (2.29) are depicted in Fig. 2.22(b). The $\mathrm{DF}_{max} = 74.3$ is reached for ring 30, which corresponds to $r_i \approx 1.2\,\mu\mathrm{m}$. Especially, in the mid-range region (ring number 10 to 30) the DFs increase continuously. The increase of the ring widths is not compensating for the decreasing contribution from the rings in that region. After ring 30 the trend is reversed and the DFs decrease again until the end of the mid-range part of the PSF_z is reached around $r_i \approx 4.7\,\mu\mathrm{m}$ (ring number 40). By comparing the DFs plotted in Fig. 2.22(b) and the investigated PSF_z shown in Fig. 2.18(a) the observed change in the trend can be explained by analyzing the slope of the PSF_z. It decreases from $r \approx 1\,\mu\mathrm{m}$ corresponding to ring number 29 and is lowest between $r \approx 5\,\mu\mathrm{m}$ (ring 40) and $r \approx 30\,\mu\mathrm{m}$ (ring 53). In the long-range part the increase of the ring width is overcompensating the decrease in the energy density contribution from the ring.

The calculated DFs plotted in Fig. 2.22(b) are used for a second simulation run. Again, each sensor-ring pair is exposed individually applying $D_B = 232\,\mu\mathrm{C\,cm^{-2}}$ for the sensor. The rings however are exposed with the

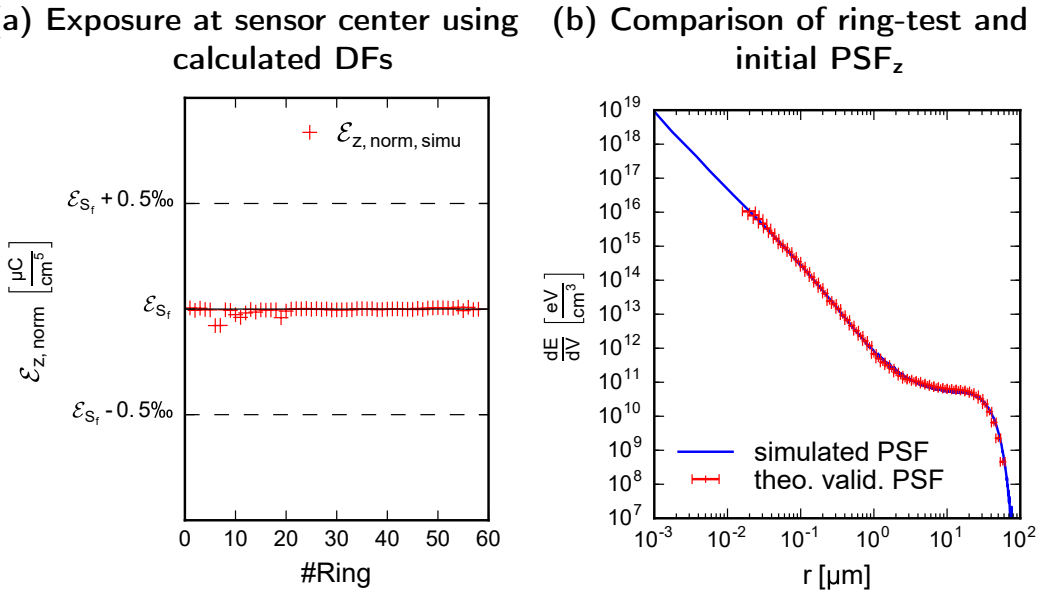

Figure 2.23.: (a) Simulated exposure at the sensor center using the calculated DFs. (b) Comparison of the ring-test and initial PSF$_z$. The ring-test PSF$_z$ matches the initial PSF$_z$ validating the explained method theoretically.

corresponding DF calculated using Eqn. (2.29) instead of a constant value. The accumulated exposure $\mathcal{E}_{z,\mathrm{norm},S}$ is extracted at the center of the sensor and is shown in Fig. 2.23(a). All extracted data points are close to the intended value $\mathcal{E}_{z,\mathrm{norm},S,f} = 172\,\mu\mathrm{C\,cm^{-5}}$ within $3\sigma = 0.007\,\mu\mathrm{C\,cm^{-5}}$. These particular low uncertainty is far below the 1 % beam current stability of the EBL systems I had access to and is therefore negligible.

The negligible 3σ value achieved in the second simulation run implies a negligible uncertainty for the calculated DFs used for the simulations, too. From the DFs the PSF$_z$ can be calculated as follows:

$$\mathrm{PSF}_z(r) = \frac{1}{DF(r)\,V_{\mathrm{ring}}(r)}. \tag{2.30}$$

Where $V_{\mathrm{ring}} = \pi\,(r_o^2 - r_i^2)\,t_{\mathrm{bin}}$ corresponds to the volume of the exposed ring within the layer z with the thickness t_{bin} from which the PSF$_z$ was extracted.

In Fig. 2.23(b) is the initial PSF$_z$ plotted and the PSF$_z$ determined from the theoretical validation is overlaid. Both agree within the uncertainty caused by the ring width, proofing the capabilities of the ring-test. In the next step the

# Ring	h_{simu} [nm]	h_{meas} [nm]	$\mathcal{E}_{z,\text{norm},S,\text{simu}}$ [µC cm^{-5}]	$\mathcal{E}_{z,\text{norm},S,\text{meas}}$ [µC cm^{-5}]	$\frac{\mathcal{E}_{z,\text{norm},S,\text{meas}}}{\mathcal{E}_{z,\text{norm},S,\text{simu}}} - 1$ [%]
16	56.83	75 ± 7	171.89	187 ± 19	8.7
18	56.83	67.8 ± 3.4	171.89	181.0 ± 9.1	5.3
20	56.83	63.8 ± 3.2	171.89	177.7 ± 8.9	3.4
22	56.84	63.5 ± 3.2	171.90	177.4 ± 8.9	3.2
24	56.84	62.0 ± 3.1	171.90	176.2 ± 8.8	2.5
26	56.84	60.6 ± 3.0	171.90	175.0 ± 8.8	1.8
28	56.84	58.2 ± 2.9	171.90	173.0 ± 8.7	0.7
30	56.85	66.6 ± 3.3	171.91	180.0 ± 9.0	4.7
32	56.85	62.2 ± 3.1	171.90	176.4 ± 8.8	2.6
34	56.85	65.3 ± 3.3	171.90	178.9 ± 8.9	4.1
36	56.84	64.2 ± 3.2	171.90	178.0 ± 8.9	3.6
38	56.84	59.0 ± 3.0	171.90	173.7 ± 8.7	1.0
40	56.83	59.0 ± 3.0	171.89	173.7 ± 8.7	1.0
42	56.83	58.0 ± 2.9	171.89	172.9 ± 8.6	0.6
44	56.83	58.4 ± 2.9	171.89	173.2 ± 8.7	0.8
46	56.83	59.9 ± 3.0	171.89	174.5 ± 8.7	1.5
48	56.83	57.4 ± 2.9	171.89	172.4 ± 8.6	0.3
50	56.83	55.7 ± 2.8	171.89	171.0 ± 8.5	−0.5
52	56.82	56.0 ± 2.8	171.88	171.2 ± 8.6	−0.4
54	56.82	57.7 ± 2.9	171.88	172.6 ± 8.6	0.4
56	56.83	57.1 ± 2.9	171.89	172.1 ± 8.6	0.1

Table 2.3.: Comparison of simulated and measured resist heights as well as exposures and a list of exposure ratios.

test is validated experimentally, too.

2.4.4. Experimental validation

After development for approximately 20 of the sensor-ring pairs the resist height is measured using the same AFM (Bruker Dimension ICON) as used to measure the calibration curve. For the measurements I assume an uncertainty of 5% for the height measurement. I started with measuring the sensor for ring 56 ($r_i \approx 44\,\mu\text{m}$) and measured every second sensor-ring pair down to ring 16 ($r_i \approx 160\,\text{nm}$). Since the measurement for the sensor-ring pair 16 was difficult the measurement uncertainty is increased to 10% for this data point. For smaller rings I was not able to measure the resist height reliably. This limitation might be caused by a combination of the quality of the AFM tip and resist process

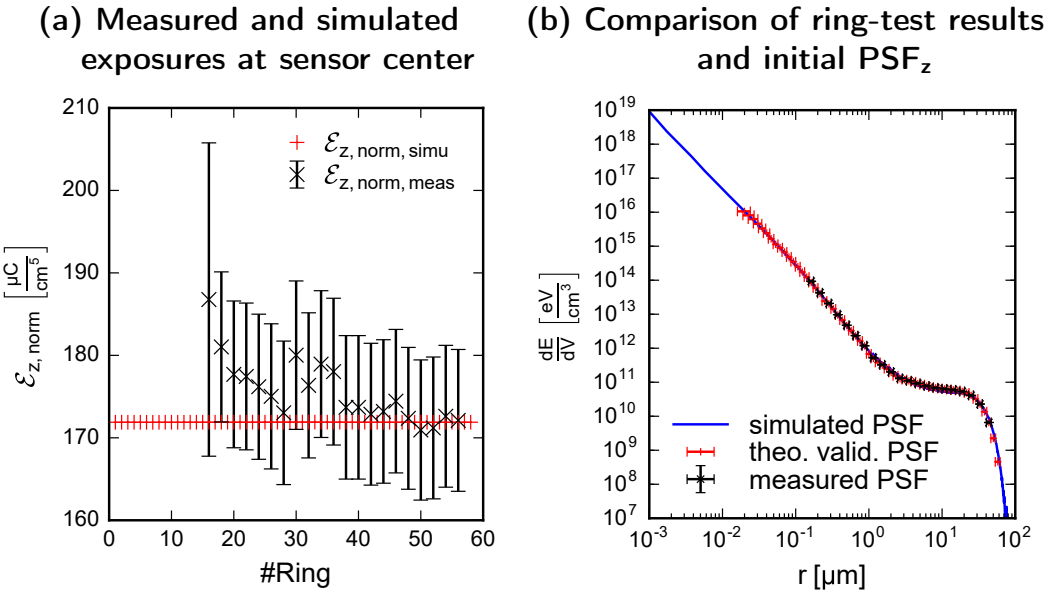

Figure 2.24.: (a) Comparison of the measured and simulated exposures at the sensor center. For small rings increases the $\mathcal{E}_{z,\mathrm{norm},S,\mathrm{meas}}$. (b) Comparison of the simulated PSF$_z$ for 100 nm PMMA on silicon, with the data generated during the theoretical validation and the experimental results. In the measurable range all three curves are in good agreement.

effects leading to an increased ring width. The measurement results are listed in table 2.3 and are compared to the corresponding simulated heights. In the same table are the derived exposures $\mathcal{E}_{z,\mathrm{norm},S,\mathrm{simu}}$ and $\mathcal{E}_{z,\mathrm{norm},S,\mathrm{meas}}$ as well as the ratio of the exposures stated. The height to exposure conversion is done by using the sensor calibration curve shown in Fig. 2.20.

In Fig. 2.24(a) are $\mathcal{E}_{z,\mathrm{norm},S,\mathrm{simu}}$ and $\mathcal{E}_{z,\mathrm{norm},S,\mathrm{meas}}$ plotted for the investigated ring-sensor pairs. The observed uncertainty is derived from the measurement accuracy of the resist height measurement. Both data sets agree with each other, however for decreasing ring diameters increases the deviation of the measurement results from the simulation results. The deviation seems to be systematically since $\mathcal{E}_{z,\mathrm{norm},S,\mathrm{meas}}$ is increasingly larger than $\mathcal{E}_{z,\mathrm{norm},S,\mathrm{simu}}$ for smaller rings. This behavior might be caused by resist processing effects influencing the developer exchange and therefore the measured resist height. Further it might be caused by the AFM since the rings are close to the sensor and the tip has to move over both the ring and the sensor. Due to the steep

transition from ring to sensor the sharpness of the used tip might be not sufficient or the feedback loop of the AFM might be not fast enough to reach the sensor.

From the DFs used for the theoretical validation is the corresponding PSF_z calculated according to Eqn. (2.30). The PSF_z for the measurement is derived by introducing the ratio $\mathcal{E}_{z,\mathrm{norm},S,\mathrm{meas}}/\mathcal{E}_{z,\mathrm{norm},S,\mathrm{simu}}$ into Eqn. (2.30), resulting in:

$$\mathrm{PSF}_z(r) = \frac{\mathcal{E}_{z,\mathrm{norm},S,\mathrm{meas}}}{\mathcal{E}_{z,\mathrm{norm},S,\mathrm{simu}}} \frac{1}{DF(r)\, V_{ring}(r)}. \tag{2.31}$$

All three PSF_zs, the simulated, the theoretically validated and the measured are shown in Fig. 2.24(b). They all agree within their uncertainties. The error bars radial position are determined from the ring width of the individual rings. The energy density uncertainty of the measured PSF_z are derived from the measurement accuracy of the height measurement.

Further tests should be done to check the systematic deviation of the sensor resist height for the smaller rings as well as a structure density dependent study of the proximity effect (PE) using the ring-test. The structure density dependency could be measured by using ring sections instead of rings. In order to keep the setup as radial symmetric as possible the ring sections should be equally distributed around the sensor. The applied dose in the sections will be increased compared to the rings with the same r_i and r_o since the reduced pattern coverage has to be compensated in order to achieve the same exposure in the sensor center.

After proving the abilities of the ring-test method to validate a simulated PSF_z it could be used to check PSF_zs for less well studied materials. For example PSF_zs for thick insulators like bulk sapphire or multilayer material stack like partially processed semiconductor heterostructures could be validated since the proximity effect in those substrates seems to be not fully represented in the PSF_z simulated by common Monte-Carlo simulation (MCS) software.

3. Resist properties

The fundamental working principal of EBL is to modify a resist on a material stack with a beam of accelerated electrons. To fabricate small structures several process steps besides the exposure itself are required. These well-controlled steps are important, since the final resolution is strongly depending on each of them. The whole process can be divided in the following categories: sample preparation, resist application, pre-exposure bake, exposure, post-exposure bake and development followed by pattern transfer. Depending on the used resist the pre- and post-exposure bake can be skipped. For a proper lithography result each step of the process has to be done properly. For example, the resist film homogeneity after spin coating affects the achievable feature size, since exposure and development depend on a homogeneous resist thickness. To achieve high-resolution EBL, it is crucial to understand physical limitations and to control the fabrication process. In this chapter I am discussing the latter. The proximity effect, a physical limitation of EBL, was investigated and explained in chapter 2.

3.1. Resists

The resist as the electron beam sensitive material is the central component of EBL. Before I am going to discuss two prominent resist representatives, I would like to explain some basic characteristics of resists and how to categorize them.

3.1.1. Classification

EBL resists are classified by their development tone into positive resists and negative resists. For a positive tone resist an increase of the solubility in a developer solution after being exposed to an electron-beam, is characteristic. During the exposure the resist molecules suffer from main-chain scissioning causing a reduction of their molecular weight. The lighter fractions of the resist molecules are dissolved in the developer. Thus the resist in the exposed areas will be removed during development while the unexposed regions are ideally

not affected. On the contrary a negative tone resist a cross-linking of the resist molecules is caused by the injected electrons. This leads to an increase in molecular weight and a decrease of solubility in the developer. In this case the exposed area withstand the developer while the unexposed regions are dissolved [2].

Each of the resist classes offers a subgroup of chemically amplified resists. For standard resists, the modification during the exposure is caused directly by the inelastically scattered electrons. In contrast, chemically amplified resists include acid generators that produce reactive acids upon irradiation. These acids modify the resist through catalytic processes and can diffuse several nanometers in the resist. Thereby the required dose to change the solubility of the resist in the developer decreases. As a drawback, the omnidirectional acid diffusion does not only lead to an increased sensitivity, but also causes a reduced resolution. During my research I studied standard resists, therefore I am concentrating on discussing them.

3.1.2. Contrast curve

Sensitivity and contrast are two important characteristics of EBL resists. The sensitivity describes the amount of dose needed to alter the resist and a high sensitivity corresponds to a low required dose.

The contrast is a measure for the dose difference between the resist is not considerably effected by the exposure and the resist is completely modified. In other words the contrast describes the abruptness of the transition in solubility caused by the exposure. It becomes visible and measurable in the sharpness of the transition from the dissolved area to the not-dissolved resist regions during development.

Both values for sensitivity and contrast can be determined via a contrast curve. Measuring contrast curves is done by exposing several large areas in the order of 250 µm with increasing dose. Before and after development, the thickness of the exposed resist has to be measured. Plotting the normalized resist thickness h_n versus logarithmic dose D results in a step-like or s-like curve. In Fig. 3.1 two contrast curves I measured are shown, one for the positive tone resist PMMA and one for the negative tone resist HSQ.

As mentioned before are contrast curves often provided by the resist manufacturer using a certain process, however they rarely matching the processing conditions on-sight. The contrast curve depends on several parameters as for example:

- energy of the injected electrons

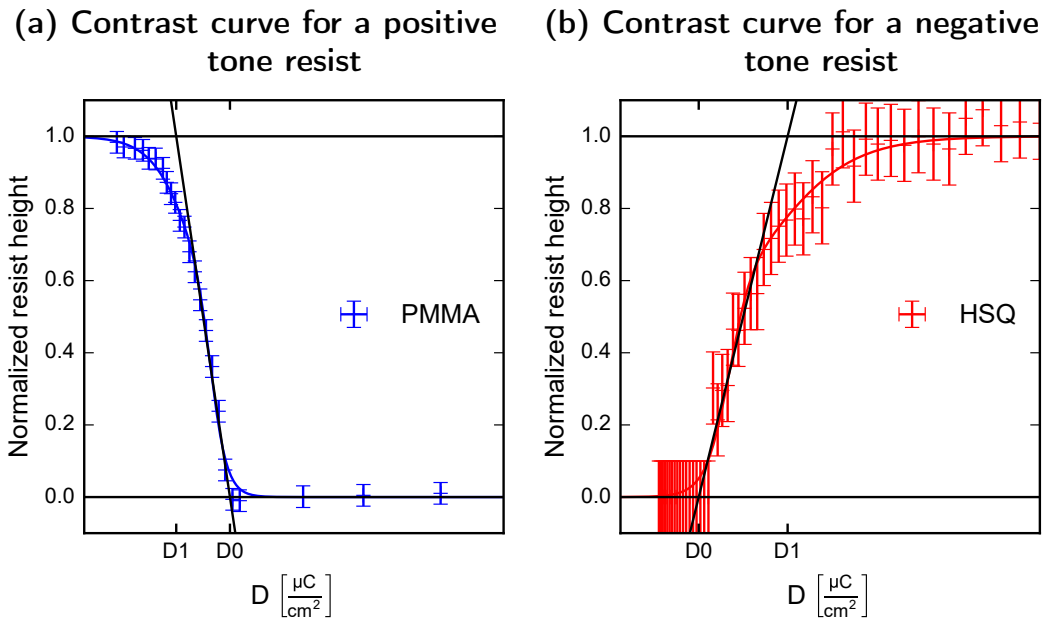

Figure 3.1.: (a) Contrast curve for the positive tone resist PMMA. The dose to clear D_0 as well as the second dose used for the calculation of the contrast D_1 are indicated. Both doses are determined by fitting the linear part of the contrast curve. For this contrast curve the contrast of PMMA was calculated to be $\gamma_{PMMA} = 5.0$ using Eqn. (3.1). (b) Contrast curve for the negative tone resist HSQ. The onset dose D_0 and D_1 indicated. The contrast was calculated to be $\gamma_{HSQ} = -3.0$. D_1 and γ_{HSQ} are determined identically as for PMMA. For both resist the fit line of the linear part of the contrast curve is drawn in black. The steepness of these fit lines is related to the contrast γ. Comparing the contrast curves (a) and (b) a higher γ for PMMA can be assumed by comparing the slopes of the linear fits.
The dose error is 1 % derived from the exposure current stability. The height error is dominated by the measurement reproducibility and interpretableness of the measurement results generated by the used Veeco Dektak profilometer. Especially for measurements of HSQ with a maximum thickness of 30 nm the measurements results were difficult to interpret, therefore the error was set to 10 % of the maximum thickness. For the PMMA contrast curve the height error was set to be 3 %.

- used developer
- development time
- developer temperature

For sensitive resists even the room temperature, the humidity or the time between exposure and development can have an influence. In order to understand a certain process it is often helpful to characterize the resist by measuring the contrast curve.

For a positive resist the contrast curve starts with $h_n = 1$ for $D = 0$ decreasing rapidly to zero after crossing a certain dose value, as shown in Fig. 3.1(a). The sensitivity is defined as the large area dose to clear (LADTC) (see section 2.2.1), which is the dose where h_n reaches zero.

The contrast γ is also determined from the contrast curve. It is introduced to characterize the dose difference needed to make the transition from being not affected by the developer to being dissolved, and is defined as,

$$\gamma = \frac{1}{\log\left(\frac{D_0}{D_1}\right)}. \tag{3.1}$$

D_0 is the dose to clear and D_1 is the dose where the linear extrapolation of the contrast curve slope crosses the $h_n = 1$ threshold (see Fig. 3.1(a))

For a negative tone resist the shape of the contrast curve is mirrored compared to the positive tone resist. It starts with $h_n = 0$ for $D = 0$ and increases rapidly after crossing a certain dose, as shown in Fig. 3.1(b). To define the sensitivity of a negative resist is more difficult since the slope of the contrast curve decreases after reaching a certain resist thickness and thereafter it is asymptotically approaching $h_n = 1$.

To define the contrast of a negative resist Eqn. (3.1) is used again. D_0 is the onset dose, which is the lowest dose where $h_n \neq 0$ can be measured. D_1 is determined in the same way as for the positive tone resist. It is determined by extrapolation the linear slope crossing the $h_n = 1$ threshold (see Fig. 3.1(b)). The sign of the contrast calculated via Eqn. (3.1) denotes the tone of the resist, and with increasing $|\gamma|$ the steepness of the slope of the contrast curve increases, too. For a negative tone resist the D_1 can be used as sensitivity. Even though if the resist is exposed with D_1 the remaining resist after development is less than the initial thickness after spinning.

High-contrast resists are interesting for high-resolution or high-density patterning. A high contrast allows small unexposed regions in immediate vicinity to exposed areas not suffering from dose background generated by scattered

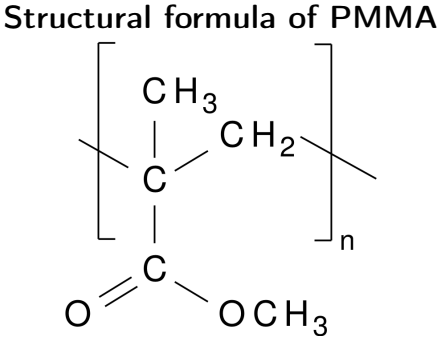

Figure 3.2.: Structural formula of unexposed PMMA [58].

electrons. Additionally a high-contrast resist suffers less from lateral development. However, high-contrast resists are usually less sensitive, causing long writing times.

Low-contrast resists are used in gray-scale lithography or for lower resolution and fast patterning due to the higher sensitivity. The lower contrast yields a broader dose range resulting in approximately the same resist thickness. Gray-scale lithography in combination with resist re-flow techniques are for example used for nano-imprint stamp fabrication [54].

3.1.3. Poly(methyl methacrylate) (PMMA)

PMMA is a popular positive tone resist in academic research. It features a resolution down to 10 nm [55, 56] and is soluble in standard organic solvents like acetone [57] or n-ethyl pyrrolidone (NEP) [32]. PMMA (see structural formula in Fig. 3.2) consists of long polymer chains of MMA dissolved in a solvent like anisole or chlorobenzene. With increasing chain length the molecular weights M_w and contrast increases while the sensitivity decreases. Different M_w are available to comply with wide range of applications.

The dependency of contrast and sensitivity on the molecular weight is caused by the exposure mechanism of PMMA, called main chain scissioning [3]. An accelerated electron interacts with a part of the PMMA chain and deposits energy or ionizes the chain. The activated PMMA has enough energy to cause the chain to split into two parts with radicals as chain termination. Radicals are not stable and therefore they react to reach a stable state. Due to the main chain scissioning the molecular weight of the chain is reduced [2]. By exposing an area with a sufficient dose, many short chain fragments are generated. These fragments can be dissolved selectively by a developer because of their low

molecular weight, while long chain parts are not affected [2]. Therefore PMMA with a lower initial molecular weight is more sensitive. Additionally the contrast is less for PMMA with a lower M_w since the dissolution rate of the unexposed polymers is not negligible.

The development of exposed PMMA is a selective solving process. The developer solution is chosen so that smaller PMMA fragments are solved and longer unexposed chains are less affected. A typical developer for PMMA is methyl isobutyl ketone (MIBK) [2]. Depending on the temperature, time and developer, contrast and sensitivity of the development process are controllable. To increase the contrast, isopropyl alcohol (IPA) can be added to MIBK [2, 59]. An even higher contrast can be achieved by using a co-solvent system of water and IPA as developer. This is particularly interesting, since both water and IPA are not suitable as developer however in a mixture they are [60].

During the development the developer penetrates the PMMA film, turns it from glass like into a gel and dissolves it [61]. This process is depending on the molecular weight as well as the glass transition temperature T_g. The shorter the PMMA chain fragments and the lower T_g are, the faster the developer can penetrate and dissolve the film [53, 62]. During the exposure both the molecular weight and T_g are reduced. Therefore the contrast can be improved by reducing the development time and temperature, since only shorter fragments are removed. The shortest fragments can be observed in close proximity to the point of injection (POI), therefore the fabrication results are more dependent on the shot placement than on the resist chemistry, allowing better control. Unfortunately, short and cold development reduce the sensitivity, too.

A typical pattern transfer process for PMMA is lift-off. For this type of process two layers of PMMA with a different M_w are coated on top of each other. The bottom layer has a lower M_w to generate an undercut during the development. During the material deposition the undercut will not be covered by material. This surface can be attacked by a remover dissolving the PMMA and lifting-off the unnecessary material. Due to its lift-off capabilities and the compatibility of the processing chemicals involved PMMA performs well in many different lithography applications, since the late 1960s [63].

3.1.4. Hydrogen silsesquioxane (HSQ)

HSQ is an inorganic negative tone EBL resist known for its high-resolution capabilities [64]. The high-resolution abilities of HSQ result from the small cube-like molecules with a silicon atom in each corner bound to oxygen atoms forming the edges of the cube. Finally, at each corner a hydrogen is bound to the silicon, forming the fourth covalent bond to it [25]. In Fig. 3.3 a proposed

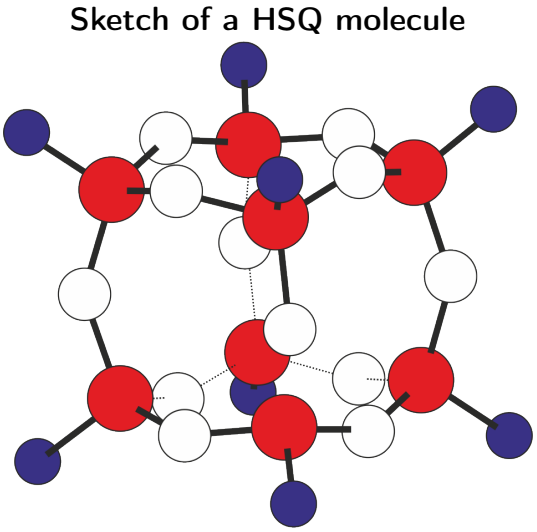

Figure 3.3.: Sketch of the proposed structural form of unexposed HSQ [25].

structure is presented. The stoichiometric formula is $H_8Si_8O_{12}$ and is available dissolved in MIBK [65].

During the exposure the molecular cages break up by the energy deposited by the accelerated electrons. The Si-O bonds are affected as well as the Si-H bonds generating radicals. Those react with each other and form new Si-O-Si bridges leading to large silicon-oxide SiO_x networks with a high molecular weight [25]. This process is called cross-linking. The cross-linked regions are not soluble in the developer because of their higher molecular weight.

With increasing dose the exposed HSQ becomes increasingly SiO_x-like and adopts its physical properties and chemical inertness. In order to develop HSQ, hydroxides are used to remove the unexposed resist. Tetramethylammonium hydroxide (TMAH) or sodium hydroxide (NaOH) are popular developers (see table 3.1). Commonly, TMAH with a concentration of less than 3 % or concentrated (25 %) TMAH are used. The higher TMAH concentration the higher the contrast (see table 3.1). The third type is the so-called salty developer, consisting of an aqueous solution of NaOH 1 % and sodium chloride (NaCl 4 %) and can also be characterized as a high-contrast developer [66, 67].

The contrast and sensitivity of HSQ processes depend on the development temperature, time and developer. Since the tone of HSQ is inverse to PMMA, contrast and sensitivity behave inverse, too. By increasing the developer temperature the contrast can be enhanced. Additionally, the pre-exposure bake conditions influence contrast and sensitivity significantly, too. In the

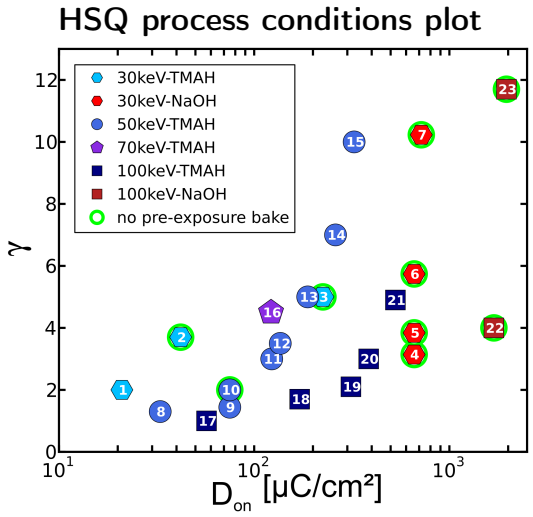

Figure 3.4.: Compilation of the HSQ contrast values γ versus onset dose D_0 for different developer conditions, baking temperatures and electron-beam energies as obtained from literature. References are given in table 3.1.

graph in Fig. 3.4 contrast values γ for several HSQ processes are plotted versus the corresponding onset dose D_0. The contrast and sensitivity values are extracted from contrast curves obtained from literature. More process details and references are summarized in table 3.1. The processes differ in developer conditions, baking temperatures and electron-acceleration energies.

For increasing TMAH concentration in the developer the onset dose D_0 increases. Using salty developer leads to an even higher D_0. The influence of the pre-exposure bake temperature on contrast and onset dose can be extracted from the plot in Fig. 3.4 as well as table 3.1. For increasing baking temperature the contrast decreases [68], independent of the developer. The contrast change is initiated by thermal activation of the resist due to the heating applied to remove the solvents before exposing the sample. Alternatively, the solvents are removable without heating by keeping the sample in ambient conditions for several days [69] or evaporating the solvents in a vacuum chamber [70, 71]. With this different approach it is possible to achieve high contrasts, too. The contrast values resulting from measurements without applying a pre-exposure bake are green encircled in Fig. 3.4.

# in Fig. 3.4	V_{acc} [kV]	γ	D_0 [µC cm^{-2}]	Baking condition	Developing	Ref.
1	30	2.0	21	150 °C 2 min and 220 °C 2 min	2.38 % TMAH	[72]
2	30	3.7	42	4 days drying air and RT	2.38 % TMAH	[69]
3	30	5.0	225	drying air and RT	25.0 % TMAH	[73]
4	30	3.1	660	no bake	1.0 % NaOH	[67]
5	30	3.8	660	no bake	1.0 % NaOH + 1.0 % NaCl	[67]
6	30	5.7	660	no bake	1.0 % NaOH + 2.0 % NaCl	[67]
7	30	10.0	718	no bake	1.0 % NaOH + 4.0 % NaCl	[67]
8	50	1.3	33	220 °C 2 min	0.26 N TMAH	[74]
9	50	1.4	75	150 °C 2 min and 220 °C 2 min	0.26 N TMAH	[75]
10	50	2.0	75	no bake	0.26 N TMAH	[74]
11	50	3.0	123	180 °C 40 min oven	2.5 % TMAH	[68]
12	50	3.5	136	180 °C 40 min oven	5.0 % TMAH	[68]
13	50	5.0	188	180 °C 40 min oven	12.5 % TMAH	[68]
14	50	7.0	261	180 °C 40 min oven	25.0 % TMAH	[68]
15	50	10.0	325	90 °C 40 min oven	25.0 % TMAH	[68]
16	70	4.5	122	120 °C no time published	2.38 % TMAH	[76]
17	100	1.0	57	not published	2.38 % TMAH	[77]
18	100	1.7	171	not published	10.0 % TMAH	[77]
19	100	2.1	313	170 °C 5 min	2.38 % TMAH	[77]
20	100	3.0	386	not published	17.5 % TMAH	[77]
21	100	4.9	529	not published	25.0 % TMAH	[77]
22	100	4.0	1690	no bake	1.0 % NaOH	[66]
23	100	12.0	1960	no bake	1.0 % NaOH + 4.0 % NaCl	[66]

Table 3.1.: Compilation of fabrication parameters for the HSQ processes compared in Fig. 3.4. All developers are aqueous solutions.

The partially high contrast values in Fig. 3.4 are another reason to use HSQ as high-resolution EBL resist. For example, a line grating with a ratio of lines and space of 0.5 (so-called filling factor $F = 0.5$) and a line width less than 5 nm was exposed using ultra-thin HSQ [64]. Due to its performance, HSQ is also used to benchmark the resolution abilities of EBL tools.

Unfortunately, HSQ shows unintended process effects. During my research I observed cross-linked resist close to exposed pattern, for high filling factors F and high doses. In Fig. 3.5(a) the red marked area is exposed and green highlighted region shows residual resist after the development. Due to a $F = 0.7$, an increased energy background caused by the proximity effect is expected. Even though this background is low compared to the deposited energy in the exposed regions it is high enough to allow a partial cross-linking of the HSQ. The energy is less than the corresponding resist sensitivity of the process, however some residuals are left after developing. This effect is called footing or scamming [2]. Taking a closer look, the surface in the unexposed area is uneven and rough compared to the exposed one (see Fig. 3.5(b)) supporting the hypothesis of underdeveloped resist. Decreasing to $F = 0.4$ the residuals are reduced like shown in Fig. 3.5(c) and (d). The lower amount of residuals allow to observe the two wedges exposed in the center and the transition from no residuals to residuals. Investigating this transition more detailed in Fig. 3.5(d) the edge is irregular and rough.

As last process step buffered oxide etch (BOE), a solution of ammonium fluoride (NH_4F) and HF in water, is often used to remove the patterned HSQ after material deposition or substrate etching [75, 78]. Depending on the resist thickness and the feature size, the so-called aspect ratio, sometimes ultrasonic agitation is applied to improve the results. Removing HSQ with HF limits the application to compatible substrates. For example quartz substrates or oxides in general will be etched during the resist removing step.

Bilayer HSQ

To use the advantages of HSQ on non-HF-compatible substrates, bilayer resist systems are an interesting approach. Commonly, HSQ is used as top layer to maintain the negative tone and the high resolution. Different bottom layers were reported in order to support the removal of the cross-linked HSQ. One of the first HSQ bilayer resists was presented by van Delft *et al.* in 2000 [75]. The bilayer was realized by spin coating a 900 nm thick layer of Novolak resin underneath a 140 nm thick HSQ top layer. Nevertheless, the assortment of materials is not limited to resists, for instance, metals can be used as sacrificial layer, too. They are more rigid than resists and resist intermixing can be

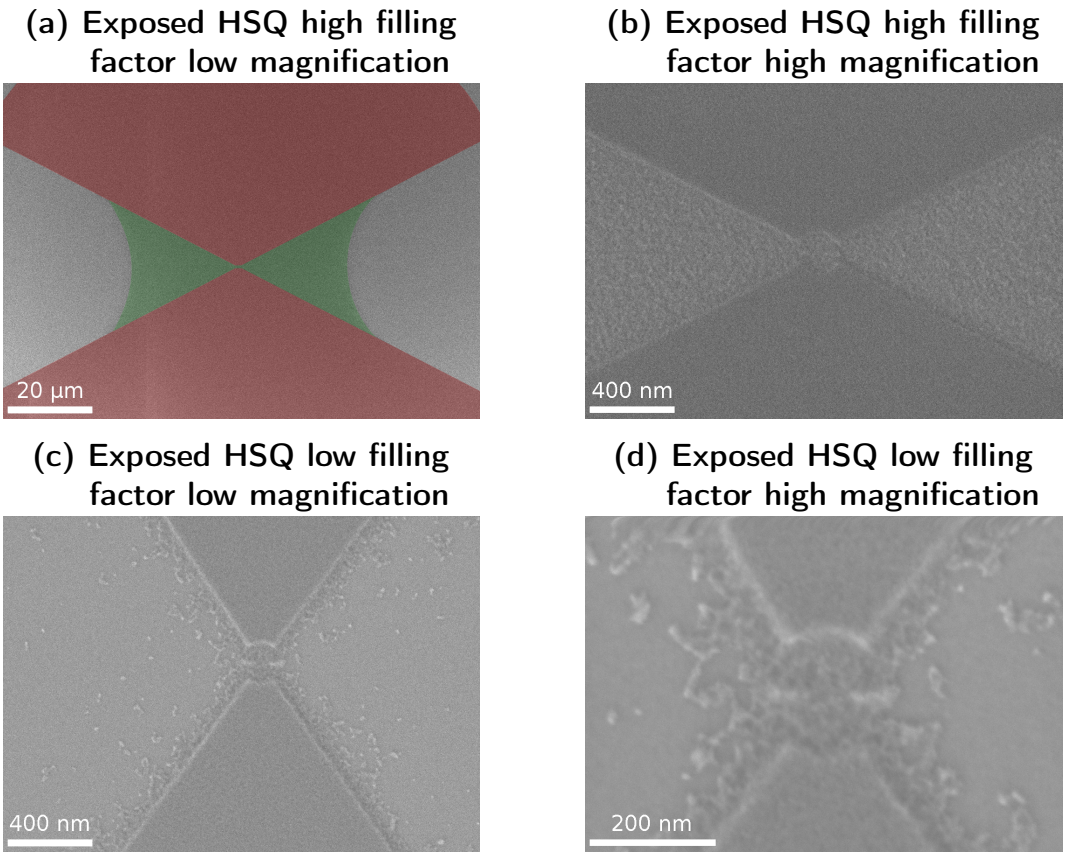

Figure 3.5.: (a) Overview SEM micrograph where the exposed region is tinted red and the observed scamming is accented green. In (b) the same part of the sample is shown like in (a) with higher magnification and no coloring. (c) A different pattern with a lower F however still scam is observed and it is unsymmetrical distributed. By increasing the magnification further the exposed bow-tie antenna in the center of the pattern can be found in (d).

excluded.

Chromium sacrificial layer An interesting sacrificial layer is chromium, due to its physical and chemical properties. It can be deposited by evaporation or sputtering and has a low etch rate in fluorine based RIE. Furthermore it works, if needed, as an in-situ discharging layer, because of its electrical conductivity. The chemical behavior of chromium is favorable, since it is not attacked by the HSQ developer TMAH. Stade *et al.* [70] fabricated metallic

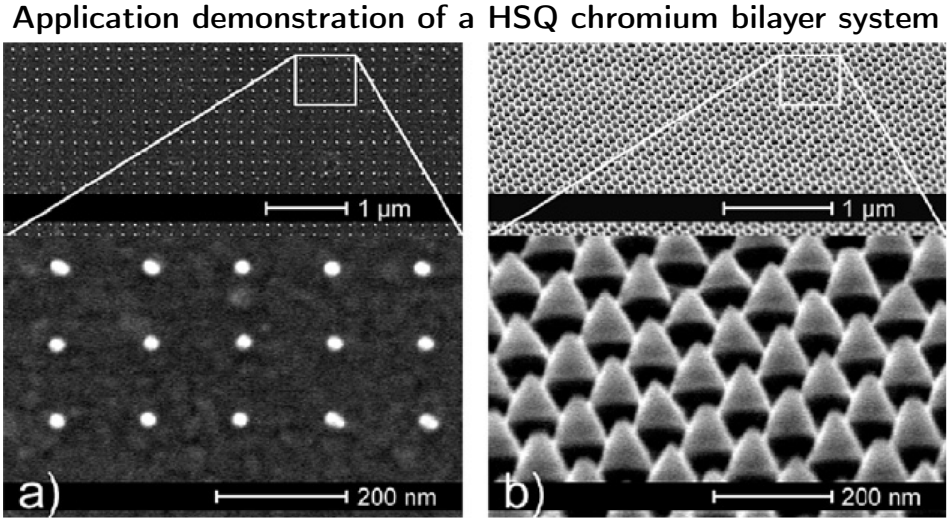

Figure 3.6.: fabrication result utilizing chrome as sacrificial layer beneath the HSQ. (a) top view SEM image of the developed sample (b) angled view SEM picture of the achieved gold cones after etching. (Reprinted with permission from Stade *et al.*, Microelectron. Eng **84**, 1589 (2007) Copyright 2007, Elsevier)

nanostructures using a 120 nm thick HSQ top layer coated on a 7 nm thick chromium sacrificial layer on top of their gold target layer. Depending on the desired process properties a pre-exposure bake can be applied to the HSQ. The sample is exposed and afterwards developed in an aqueous TMAH solution with a concentration depending on the required sensitivity and contrast. To stop the development process the sample can be rinsed for example in deionized (DI) water or IPA. The pattern defined in the resist is transferred to the chrome layer by a wet chemical etching process, ion milling or dry etching. Stade and coworkers ion milled both the chrome and the underlying gold layer simultaneously. Finally, the HSQ can be removed by dissolving the chromium layer in chrome etch, an aqueous solution of ceric ammonium nitrate and nitric acid [79]. The reported results show well defined nanostructures (Fig. 3.6 [70]).

Resist Sacrificial Layer The conventional approach is to use a resist as sacrificial layer. Since both resist layers are exposed by the electrons it is important to have different resist chemistry for both layers. In the first place the solubility of the bottom layer in the solvent of the top layer has to be considered to avoid resist intermixing during spin coating. Secondly the needed

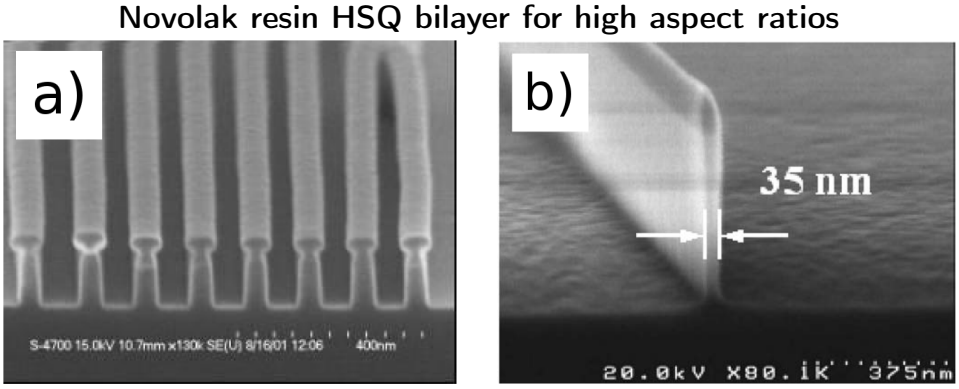

Figure 3.7.: Novolak resin as sacrificial layer beneath HSQ for gratings with low edge roughness (a) (Reprinted with permission from Jamieson *et al.*, Proc. SPIE **4690**, 1171 (2002)) and high aspect ratio resist patterns (b) (Reprinted with permission from Xiao and Yang, J. Vac. Sci. Technol. B **24**, 2940 (2006) Copyright 2006, American Institute of Physics)

dose for HSQ should not result in a degradation of the sacrificial layer and thus hampering its lift-off. The third challenge is the development process. HSQ offers already two developing processes applying TMAH or a solution of NaOH and NaCl. Either choice might help to avoid dissolving the bottom resist layer, otherwise the HSQ peels off or is washed away.

Novolak resin Novolak resists are based on a phenol-formaldehyde resin matrix [79, 80, 81] and are often used in photo lithography. They are interesting as sacrificial layers, since these resists can be spin coated as thick layers in a single step and they are soluble in organic solvents. Unfortunately, Novolak resin is soluble in TMAH like unexposed HSQ, hence it has to be hard-baked before spin coating the HSQ to prevent the sacrificial layer from dissolving during development. After the exposure and development of the HSQ, the pattern can be transferred into the bottom resist layer via an oxygen plasma. With this bilayer system an aspect ratio > 15 at a line width of 35 nm was achieved, which is depicted in Fig. 3.7. These aspect ratios are enabled by the mechanical stability of the cross-linked Novolak resin and allow a pattern transfer into the sample by ion milling or other etching methods. In the end the resist stack is removable by dissolving the hard-baked Novolak resin residuals in organic solvents. Difficulties with solubility of the Novolak resin may arise as a result of thermal treatment during hard bake [82].

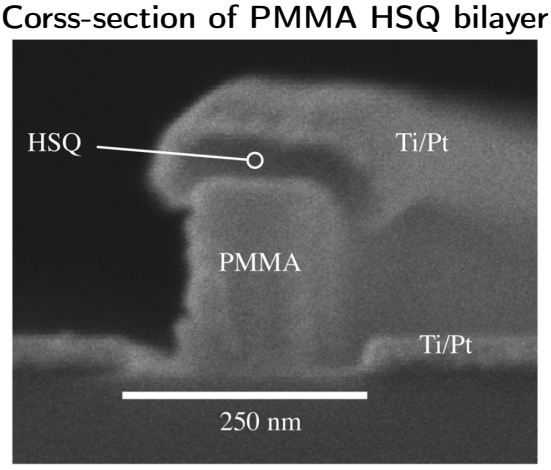

Figure 3.8.: Cross-section of a developed PMMA HSQ bilayer resist coated with Ti/Pt, emphasizing the integrity of the sacrificial layer before lift-off. (Reprinted with permission from Thoma and Macityre, J. Vac. Sci. Technol. B **30**, 06F305 (2012) Copyright 2012, American Institute of Physics)

PMMA PMMA is a resist commonly used as sacrificial layer underneath HSQ [32, 69, 72, 82, 83, 84, 85]. It has proper adhesion capabilities, is easy to handle and one of the best-investigated EBL resists. Thus it is a proper choice to start a new development. Especially in this case the chemical properties fit well to those of HSQ. For example, it is not effected by TMAH and can be etched easily by oxygen plasma. Further, it can be stripped in standard organic solvents. The only possible issue of a HSQ/PMMA bilayer is resist intermixing during spin coating, since HSQ is dissolved in MIBK and MIBK is a common developer for PMMA [2]. For this reason a PMMA with a higher molecular weight is advantageous and the bake before spinning the HSQ on top of the PMMA is important [32]. In literature several different doses have been reported, depending on the acceleration voltage, the resist thickness and the type of developer [3, 86, 87]. All three development methods mentioned before, low- and high-contrast TMAH as well as salty developer, can be employed depending on the application. During rinsing it turned out to be important to avoid organic solvents, because the solubility of the PMMA bottom layer is increased after the exposure. The subsequent PMMA etching is usually done by pure oxygen plasmas under various conditions. In order to dilute the plasma or to add a sputtering component, Ar can be added. A showcase resist profile after etching the pattern into the PMMA and metal deposition is presented in

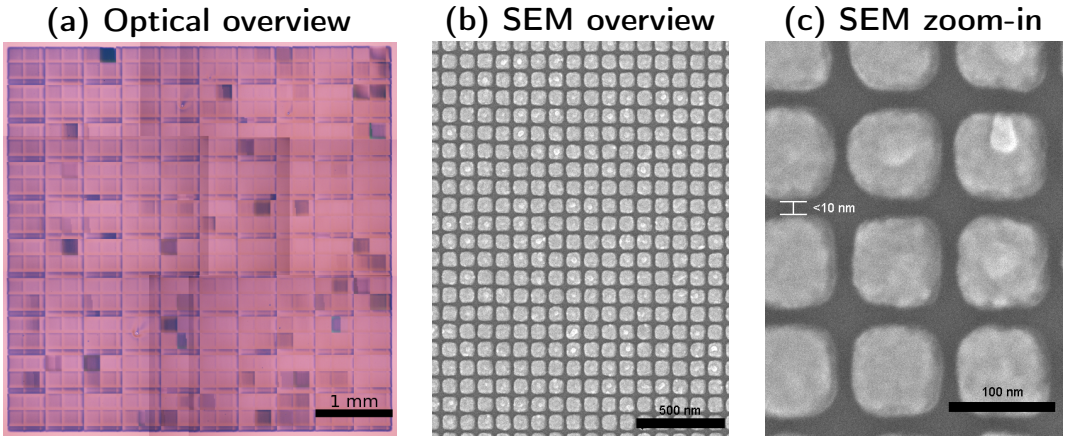

Figure 3.9.: (a) Overview image emphasizing the large-area applicability of the PMMA HSQ bilayer process [1]. SEM micrograph demonstrating the pattern uniformity (b) and resolution (c).

Fig. 3.8. After ectching the PMMA further processing steps - depending on the application - can follow, for example material deposition or etching of the underlying substrate. The last step is to remove the residual resist stack by an organic solvent like NEP. To improve the dissolving of PMMA it can be heated up to 80 °C and - depending on the sample - ultrasonic agitation can support the resist stripping.

By applying a HSQ/PMMA bilayer resist I was able to fabricate sub-10 nm gaps, which was the highest resolution shown on HSQ bilayer systems at that time. With that technique it is possible to create gapped metal quasi-films of arbitrary physical dimensions, preserving this high resolution. In Fig. 3.9(a) a patterned gold film with an edge length of 5 nm consisting of 100 nm squares separated by gaps smaller than 10 nm is shown. The pictures in Fig. 3.9(b) and (c) demonstrate the uniformity of the gaps and their widths. Before such a resolution has been only achieved by processing HSQ single layer resists [78]. Such quasi-films are useful to study, for instance, optical properties at the percolation threshold. More information about this process can be found in the second part of this thesis in section 6.2.

[1] The visible non-uniformities and field borders are machine dependent negligible changes in the pattern periodicity optically amplified by interference. More information regarding the process can be found in section 6.2

3.2. Post-processing

After transferring the designed pattern into the resist the post-processing starts. In principle it is possible to use lift-off techniques to create structures on the substrate by adding material or transfer the developed pattern into the substrate by etching.

3.2.1. Lift-off

During my research I focused on densely packed metallic nanostructures using lift-off techniques. Lift-off is often used for the fabrication of small metallic particles, since this technique can be combined with many materials [86]. In principle any material which can be deposited by physical vapor deposition methods. During the material deposition a homogeneous layer is accumulated on the substrate. In the resist-free regions the material sticks directly to the substrate and in the other areas it lays on top of the resist. For the lift-off of the resist supported areas a gap at the flank is needed where the remover can attack the resist. As a consequence the flank profile and the difference between resist height and deposited material thickness are important. If the flank has no undercut or is not at least straight, material will cover it and hamper the lift-off.

Sometimes it is possible to improve the lift-off result by applying ultrasonic agitation, increasing the remover temperature or using a solvent with better wetting properties [3]. For PMMA, NEP is a remover featuring a higher inflammation temperature and an improved wetting compared to acetone.

Harsh lift-off conditions are avoidable by a proper undercut. Using a bilayer resists, for instance a PMMA bilayer can provide a proper undercut [2]. The bottom layer is a resist with a lower M_w and is therefore more sensitive than the top layer. The molecular weight of the top layer PMMA offers a better contrast and is therefore able to define small structures more reliably. Since the dose has to be high enough to properly develop the top layer the bottom resist is overexposed. The developer causes the formation of a cave and the top layer becomes freestanding accounting the mechanical stability of the PMMA. Using physical vapor deposition methods with a long distance between source and sample the undercut area is protected from material deposition and the remover can attack the resist.

A second approach is to use two different resists based on an independent chemistry like the in section 3.1.4 explained bilayer systems combining HSQ with a sacrificial layer.

The highly reactive oxygen rich atmosphere in the plasma allows the substitution of further Si-H bonds by Si-O-Si bridges and the developed resist is getting increasingly SiO_x-like [88]. After material deposition the PMMA is dissolved in a suitable remover and the HSQ covered with material is washed away. Again the result can be improved by using harsh lift-off conditions.

3.2.2. Etching

After transferring the pattern into the resist, it is possible to use it as mask for material removing techniques like ion milling, wet-chemical etching or RIE [86].

Ion milling is achieved by accelerating ions with a high mass like argon ions onto a substrate. The particles are extracted out of a plasma and accelerated onto the target. With their high momentum the ions blast parts out of the substrate. Redeposition of the removed material is limiting factor of this technique [86].

RIE is comparable to ion milling however the inert particles are exchanged by reactive once like oxygen or fluorine. The chemical component of the process helps to improve the selectivity between resist and underlaying material. An advantage of RIE over ion milling is the volatileness of the reaction products solving the redeposition issue, however not all materials can be etched by RIE [86].

For wet-chemical usually a high selectivity between resist and etched material can be achieved, however the etching is often isotropic. The isotropy is causing under-etching, which changes the lateral dimension of the pattern, additionally the process kinetics strongly depend on the etching depth. The deeper and narrower a trench gets, the more difficult saturated etchant can be exchanged [86].

3.3. Conclusion

During the processing steps many different effects influence the lithography result, therefore it is important to control each of them as good as possible. The number of possible processing effects prove the observed difficulties to study the physics behind the EBL technique. Investigated phenomena are always blurred and superimposed by process artifacts. To avoid some of the effects it is common to investigate the resist directly after developing. By omitting the post-processing the accompanying process effects are avoided, too. SEMs are often used to investigate structures fabricated with EBL, since they feature high resolution and can change the magnification fast. Unfortunately positive

tone resists suffer system inherently from degradation while investigating the resist with a SEM. Negative tone resists do not suffer from radiation degradation during SEM investigation since the cross-linking is promoted by further exposure.

HSQ is an interesting resist featuring high resolution, however resist removal and processing effects for dens patterns are an issue to overcome. Both issues can be solved by using bilayers of HSQ and an underlaying sacrificial layer.

Electron-beam-lithography

A versatile tool for solving challenging nanofabrication tasks

4. Vortex holograms for transmission electron microscopy

Transmission Electron Microscopy (TEM) is an advanced microscopy technique with resolution in the sub-nm range [89]. The accelerated electrons are sent through a thin sample and interact with the atoms. By raster-scanning the beam space-resolved images are possible. With the right conditions atoms are resolvable. Besides the resolution TEM posseses manifold analysis methods [90].

4.1. Motivation

A common TEM analysis method is electron energy loss spectroscopy (EELS) [90]. The material properties are investigated by measuring the energy lost by the interaction of the high energetic electrons and the specimen. Schattschneider *et al.* presented a method to measure energy-loss magnetic chiral dichroism (EMCD) using EELS with electrons having an orbital angular momentum (OAM) different from zero [91]. EMCD allows to measure magnetic properties of the material atoms, like spin and orbital magnetic momentum [92], combined with high spatial resolution.

Verbeeck *et al.* proposed a method to generate electrons with OAM using a vortex beam, a helical wavefront with a phase singularity in the middle. Vortex beams are constructed by illuminating holograms with electrons [93], which coherently form a wavefront in a conventional TEM. The pattern I used for fabrication is shown in Fig. 4.1 and is a calculated in-line hologram. The following explanation is a recreation of the calculations presented by Verbeeck *et al.* [93]. In order to separate the incident and the reconstructed beam, a tilted plane wave $\Psi_{\text{ref}} = \exp(i2\pi k_\perp \cdot r_\perp)$ is used [94]. The complex wave function $\Psi_t = \exp(il\phi)f(r)$ carries the topological charge $l = \pm 1$ we are interested in. By interference $I_{\text{holo}} = |\Psi_{ref} + \Psi_t|^2$ the intensity distribution in the hologram is calculated. By applying a threshold the intensity distribution turn to the

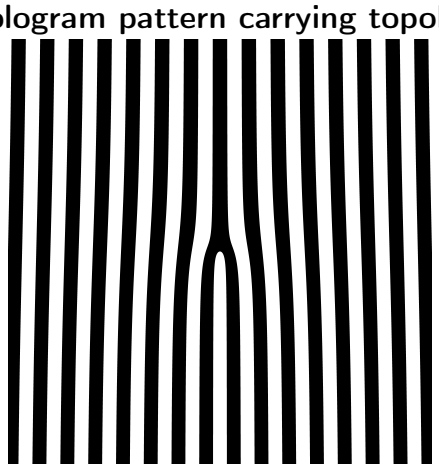

Figure 4.1.: Hologram pattern calculated for carrying topological charge $l = \pm 1$.

resulting pattern shown in Fig. 4.1.

The vortex hologram looks like a line grating. In the lower half the pattern is slightly distorted compared to the upper half, resulting in a fork-like structure in the center of the pattern. The calculation result does not show discontinuities or steps long the line edges.

This type of hologram was reported by Verbeeck and coworkers in Ref. [93] using $d = 100\,\mathrm{nm}$ thick Pt foil. The pattern was cut into the foil by focused ion-beam milling (FIB), achieving a line width of $w_{\mathrm{FIB}} \approx 300\,\mathrm{nm}$ and an aspect ratio height to feature width of 1:3.

The vortex hologram is challenging to fabricate by EBL, since the filling factor of the pattern is $F \approx 0.5$ and it has the fork-like structure in the center. Another issue is the trade-off between resolution and material thickness. On one hand the smaller the lines get the better the beams with different OAM are separated. On the other hand the material thickness is limited by the aspect ratio of the resist features. Further the material thickness influences the opacity of the hologram and therefore the interference quality. Line width and possible material thickness depend on each other since the reachable resist aspect ratio is reduced with decreasing area of support [86]. In order to fabricate an useful sample the process has to be optimized to the limit.

To transfer the OAM to the electrons, they have to travel through the hologram. The utilized substrate has to be transparent for the electrons, which is achieved by using thin membranes. From the lithographic point of view fabrication on a membrane is interesting. The reduction of a bulk substrate to a 30 nm thin membrane leads to nearly no back-scattering, therefore the

proximity effect (PE) is dominated by forward-scattering. As a result the dose increases, the resolution limitation caused by forward-scattering can be tested and thus it is possible to fabricate structures with EBL with nearly no PE. The process is described in the following sections.

4.2. Sample preparation

To achieve vortex holograms with a sub-100 nm grating period with EBL a lift-off process is developed. As substrate a 30 nm thin silicon-nitride (SiN) membrane is utilized to keep the scattering probability low and to have robust membrane for the fabrication process [90].

4.2.1. Substrate and handling

The substrate is a $d_{\mathrm{mem}} = 3\,\mathrm{mm}$ wide and $h_{\mathrm{mem}} = 200\,\mu\mathrm{m}$ thick Si disk covered with $h_{\mathrm{SiN}} = 30\,\mathrm{nm}$ SiN. Nine square windows with an edge length of $l_{\mathrm{mem}} = 100\,\mu\mathrm{m}$ are etched into the substrate revealing freestanding SiN membranes. These substrates are commercially available.

Since the membranes are small and fragile, standard processing steps are challenging. For example, spin coaters use vacuum to fix the sample and would thereby destroy the membranes. I solved this issue by fastening the substrate with tape. Another problem caused by the substrate size was the sample holder of the lithography system. The smallest loadable samples in the JEOL JBX-6300FS in Stuttgart have to be at least 5 mm broad, since they are loaded from the back-side and clamped to a reference slit.

I developed a special sample holder to handle the membrane substrates in the EBL tool (see Fig. 4.2). The holder consists of a 1 cm × 1 cm large and 1 mm thick aluminum square with a hole in the center. At the front side around the hole a 200 µm deep stage for the substrate is milled. Into the back side four trenches are milled connecting the corners with the center to evacuate the back side of the membrane. If air would remain underneath the membrane, the low-pressure in the EBL system could destroy it. To fix the substrate on the aluminum plate, two beryllium-bronze springs are screwed into the holder. By avoiding blind holes, gas emission from the holes are prevented. The top surface of the plate is clamped to the reference plane like an ordinary sample, therefore the surface and the milled stage have to be plane and coplanar to reduce exposure errors. An additional advantage of the holder is the improved handling of the sample also during further processing steps. Due to the round shape, the small thickness and the chamfer at the edge, the handling of the

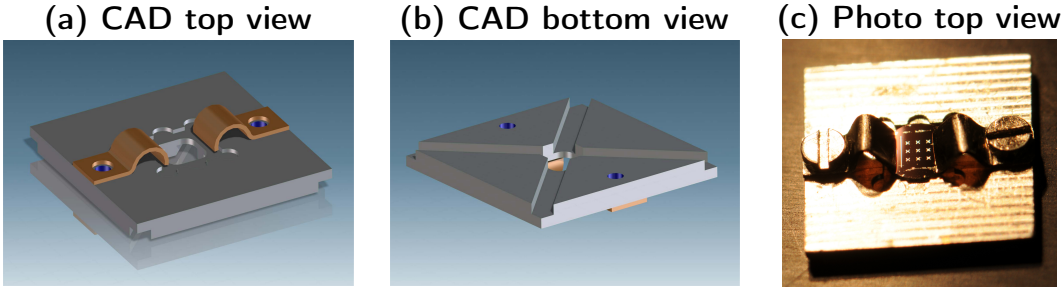

Figure 4.2.: CAD design of the membrane sample holder. (a) Iso top view, (b) iso bottom view. (c) Photograph of the holder with sample.

bare substrate during processing is challenging. To avoid handling issues I mounted the substrate to my holder directly after spin coating.

The membrane is protected in the sample holder, however forces perpendicular to it, which can occur during moving the sample in solvents are still a potential threat. Only careful handling can protect the sample, for instance gently moving the substrate in liquids and the membrane has always to be perpendicular to the surface of the liquid while taking it out of the beaker. Moreover ultrasonic agitation is omitted.

4.2.2. Process flow

To avoid unnecessary damaging of membranes and to keep the clean surface which the supplier provides, I skip the cleaning step. The first step is therefore spin coating. Because of the sample fragility a tape is used to mount it onto the coater as previously explained. As resist, a single PMMA layer with a molecular weight $M_w = 950\,k$ and a thickness of $h = 65\,\mathrm{nm}$ is used. The primary goal was to achieve a grating with filling factor $F = 0.5$ and as small as possible line width, therefore the thin resist is necessary.

Afterwards the sample is mounted into the home-made holder and loaded into the lithography system. For the exposure the electron acceleration voltage $V_{\mathrm{acc}} = 100\,\mathrm{kV}$ and the current $I = 100\,\mathrm{pA}$ are chosen. Moreover the high-resolution mode is applied, using the objective lens with a shorter working distance realizing a higher numerical aperture (NA). These settings result into a beam diameter better than 5 nm The distance between two shots is 16 nm and dose $D = 1100\,\mu\mathrm{C\,cm^{-2}}$. Since the substrate is very thin and therefore practically transparent for the 100 keV electrons, back-scattering is negligible. The same holds for PMMA since the atomic number of the involved elements is low and so the scattering angles are low, too. If back-scattering has not

to be corrected and the resist only causes little forward-scattering, proximity effect correction (PEC) can be omitted. Therefore the pattern is exposed like in Fig. 4.1, without any correction.

The exposure is followed by the development process. To preserve the better handling properties of the home-made sample holder the substrate stays mounted. As developer MIBK:IPA 1:3 is used. The usual stirring with the sample during the $t = 50\,\mathrm{s}$ development is skipped to protect the membranes. Then the sample is moved into a beaker with IPA to rinse the developer for $t = 15\,\mathrm{s}$. To avoid marks the sample is dried by gently evaporating the IPA using a nitrogen air gun.

Subsequently, the sample holder is exchanged by one of the same type however dedicated for the evaporation process. This holder exchange is a protective measure to avoid contamination by material pealing off from it. The sample with holder is mounted into an evaporation chamber plus two tungsten (W) boats. One is filled with titanium (Ti) and the other with a gold palladium alloy (AuPd). In the first step the sample is coated with a 5 nm Ti adhesion layer followed by 30 nm AuPd. The material is thermally evaporated through resistive heating of the W boats. Gold palladium provides a smaller grain sizes than pure Au, which is interesting for high-resolution lift-off processes, however the effective atomic number (Z) of the alloy is lower. Z and the material density ρ are influencing the thickness needed to reach an opaque film for the accelerated electrons in the TEM.

After the evaporation the holder including the sample is transfered into a beaker with NEP, heated up to $T = 80\,^{\circ}\mathrm{C}$ and stored there for $t = 2\,\mathrm{h}$. The used 100 keV electrons and the thereby caused low forward-scattering angle lead to steep side walls without undercut, which complicates the lift-off. Usually ultrasonic agitation would be the key to success, however the membrane would not survive. The alternatives are megasonic agitation and syringe supported lift-off. Due to the persistence of the residual AuPd I used both. The megasonic bath uses a higher frequency of $f_{\mathrm{MS}} = 1\,\mathrm{MHz}$ instead of $f_{\mathrm{US}} = 50\,\mathrm{kHz}$ and is not damaging the 30 nm thick SiN membranes. A syringe is used to gently flush hot remover parallel over the sample and thereby sweeping away residual material. Finally the sample has to be cleaned again, by applying a sequence of baths in acetone and IPA followed by drying with nitrogen.

An SEM image of a successfully fabricated filter is depicted in Fig. 4.3(a). With the explained process it was possible to achieve a grating with 40 nm line and gap width, reproducing every detail including the fork-like structure in the center. One of the vortex filter I produced was inspected with a TEM utilizing the high resolution and the result is presented in Fig. 4.3(b).

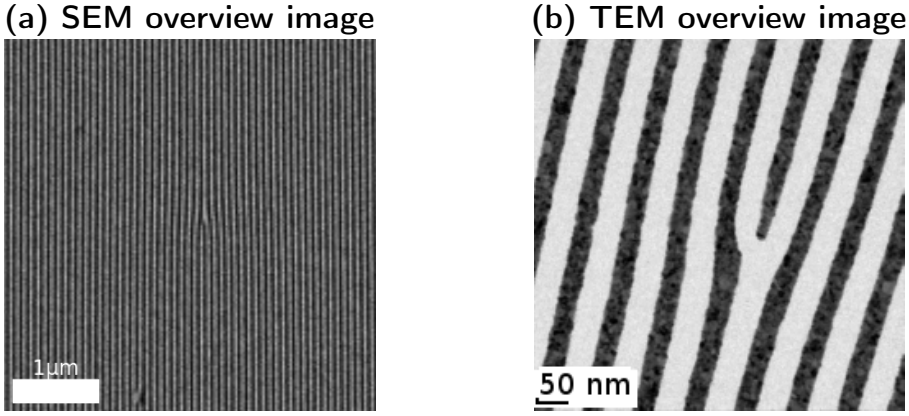

Figure 4.3.: Fabrication result of a filter: (a) SEM overview picture emphasizing the grating uniformity. (b) TEM overview image proofing pattern quality in near proximity of the vortex. The TEM image was taken by Dr. Behnaz Rahmati from the Stuttgart Center of Electron Microscopy (StEM) at the MPI-FKF.

4.3. TEM results

The fabricated filter was inserted into the column of a TEM and the beam was analyzed. The following measurements were performed by Dr. Behnaz Rahmati using the Zeiss SESAM owned by the StEM center in the Max-Planck-Institute for Solid State Research in Stuttgart Germany. Comparing Fig. 4.4(a) and Fig. 4.4(b) shows a clear influence of the grating. It clearly causes interference, however the beam does not show the expected and reported ring shape for the non-zero diffraction orders [93]. The expected donut shape was explained by the chiral wavefront of the interfering electrons.

To investigate whether the interfered beam is carrying topological charge despite the fact that it does not show a minimum intensity in the center, a thin iron film (20 nm) on a manganese-oxide substrate was studied. With EELS it is possible to observe the electronic transitions $2p_{1/2}$ to 3d (L_2-edge) and $2p_{3/2}$ to 3d (L_3-edge) in Fe [95]. Using a vortex beam the intensity of the transition for left-hand and right-hand rotation are not equal. The difference of the spectra is the dichroic signal [96]. Such spectra are presented in Fig. 4.5. Unfortunately, the signal difference was only observed at one position on the sample (compare Fig. 4.5(a) and Fig. 4.5(b)) and was not reproducible. After several tests and different setup positions in the column of various TEMs the project was stopped.

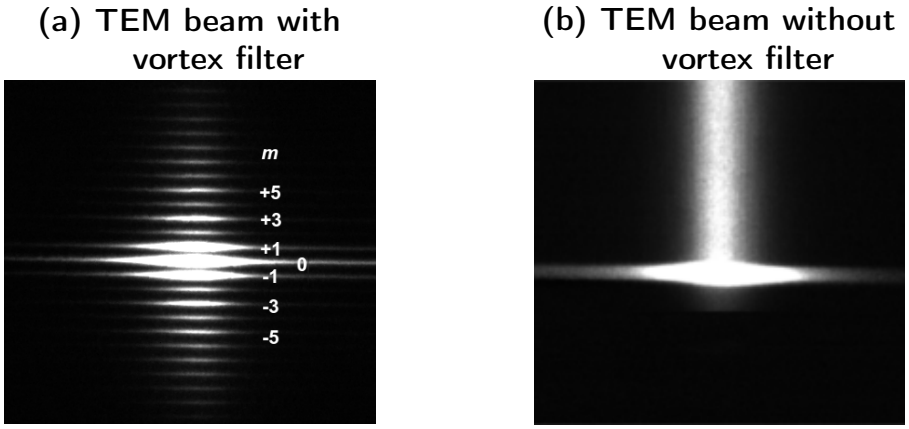

Figure 4.4.: Comparison of the spectral image of (a) the vortex filtered beam and (b) the uninfluenced beam. The TEM images were taken by Dr. Behnaz Rahmati from the Stuttgart Center of Electron Microscopy (StEM) at the MPI-FKF.

In the original paper from Verbeeck *et al.* which inspired our collaborators the hologram pattern was transfered into a 100 nm Pt foil [93]. The Z and ρ for Pt and Au are close however the thickness of the Au hologram I fabricated is only 30 nm. In order to understand the difference of the Pt and the Au hologram I performed Monte-Carlo simulations investigating the opacity of Pt and Au films of various thicknesses. For the simulations I use PENELOPE again. This time I am comparing the number injected electrons with the number of reflected, absorbed or transmitted electrons. In Fig. 4.6(a) the simulated transmittance, reflectance and absorbance of Au layers with increasing film thickness on a 30 nm SiN membrane are shown. To reduce the transmission through the film by 10 %, a film thickness of approximately 500 nm would be needed. Form Fig. 4.6(b) it can be seen, that the 30 nm thick AuPd grating on a SiN membrane, which I fabricated, has a transmittance of 99.6 % for 100 keV electrons. A 100 nm thick free standing Pt layer has a transmittance of 98.3 %. The difference is not large however might be enough to allow the observation of vortex with the Pt filter and not with the Au hologram.

4.4. Optimization

Unfortunately, the project was stopped and therefore I had no opportunity to further improve the process. During the process development phase I was not aware of several possibilities to improve the lithography. Starting from the

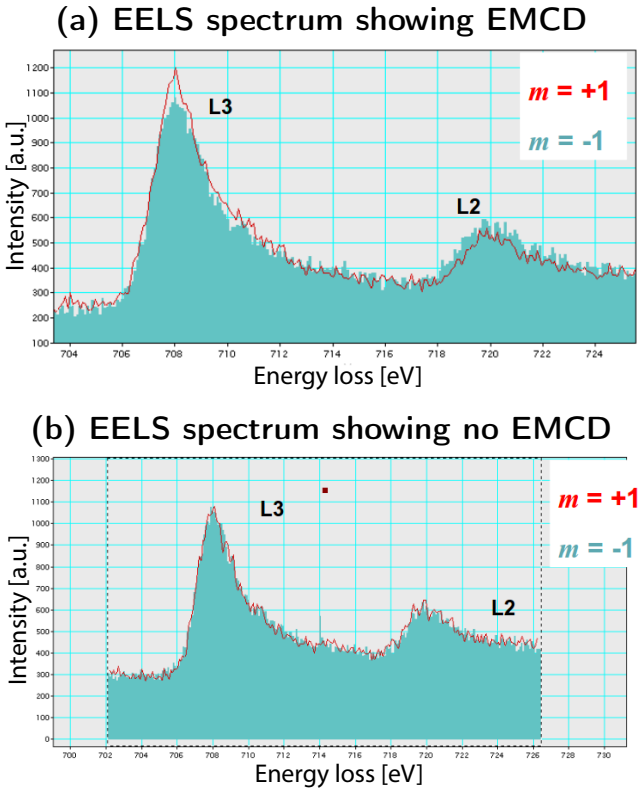

Figure 4.5.: (a) EELS spectrum of Fe on MgO showing chirality dependence of the $L_{2,3}$ edge signal. (b) EELS spectrum of the same sample measured at a different position showing no chirality dependence. The EELS spectra were taken by Dr. Behnaz Rahmati from the Stuttgart Center of Electron Microscopy (StEM) at the MPI-FKF.

pattern, it is possible to increase the processing contrast by using an undersize-overdose exposure scheme. In this case the line width is reduced, however the periodicity is kept constant and the dose is increased to compensate the reduced line width. This approach leads to higher contrast, since the increased dose causes shorter resist fragments in the exposed region, reducing the influence of developer diffusion. Another approach to increase the contrast is to change the developer to IPA:H_2O and try to improve the resolution or reach the same line width with a thicker resist.

The next aspect to optimize is the evaporation material and its thickness. Instead of AuPd, pure gold improves the opacity for the electrons and by increasing the evaporation rate the grain size is reduced. A thicker Au layer

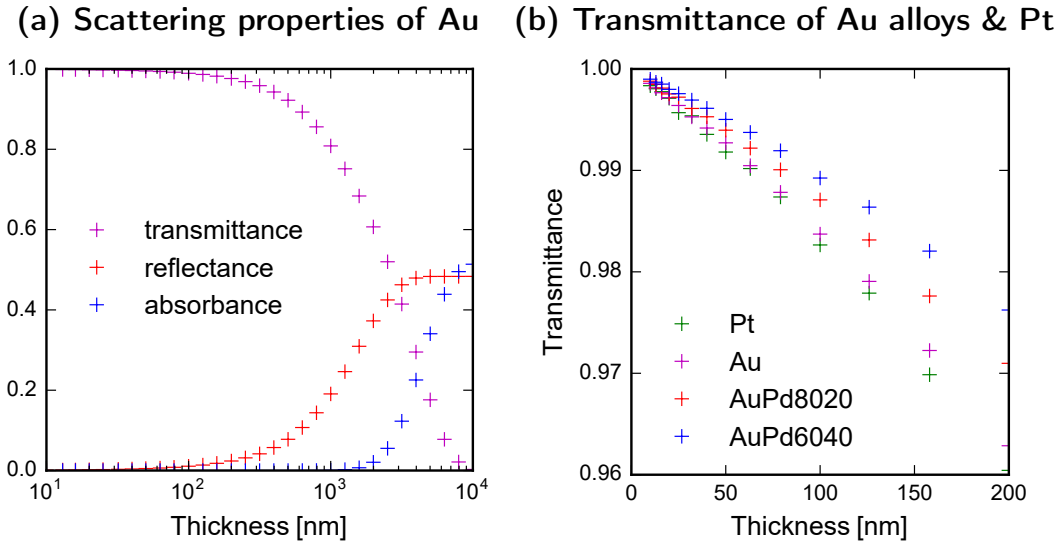

Figure 4.6.: (a) Simulated opacity of increasingly thick gold films for 100 keV electrons. For gold films thinner than 1 µm absorption is negligible. (b) Comparison of the transmittance for different gold alloys and Pt below 200 nm film thickness.

would increase the opacity of the lines in the grating, too. Unfortunately, for a thicker Au layer the resist has to be made thicker, too. This reduces the resolution, since the aspect ratio of PMMA is limited by its mechanical stability, and especially for thin structures the achievable aspect ratio decreases. To improve the lift-off performance, one approach is to change the resist. Instead of a thin layer of PMMA, it is possible to use a PMMA bilayer system to create an undercut, however this again compromises the aspect ratio. At the end of the day there is the question how to find a compromise between Au thickness and line width, however I am sure both can be increased at least somewhat. Unfortunately, it seems like the material thickness has to be increased by orders of magnitude (see Fig. 4.6). Even with gold, ten micron film thickness are needed to achieve an opaque film. It might be possible to get results for thinner metal layers however for a 90 % transparent grating, the required gold film thickness still would be 500 nm. Using evaporation and lift-off this thickness would be hardly possible to achieve featuring narrow and dense features.

5. Optical investigation of pseudo-randomly ordered nanodisks

In this chapter I will discuss the fabrication of large areas covered by randomly distributed nano disks. Two different methods will be investigated. First, I will briefly introduce hole-mask colloidal lithography (HCL) a cost-effective method to produce large areas covered with nano disks. Further I will explain how to fabricate such patterns using EBL and pseudo random numbers and present the samples I fabricated.

Khunsin *et al.* investigated the dipole orientation of nano disks forming amorphous nanostructures while they are excited resonantly by light [97]. They mapped the near-field distribution of many disks at their dipole resonance using an apertureless scanning near-field microscope (aSNOM). Their investigation revealed an unexpected directionality of the dipole orientation over a large distance. Their samples were fabricated using HCL. SEM micrographs of the investigated samples are shown in Fig. 5.1. The question is whether it is possible to see a manifestation of the effect in far-field measurements and if the result depends on the lithography method. In this thesis I will only comment on the lithography techniques used to produce such structures.

5.1. Hole-mask colloidal lithography

HCL is an alternative lithography method allowing large-scale parallel fabrication of structures, however it has certain pattern limitations. This approach was reported by Fredrikson *et al.* in Ref. [98]. The subsequent description is based on their publication. For HCL the substrate is coated with a sacrificial polymer layer, such as PMMA, and treated with a short oxygen plasma to increase the hydrophilicity of the surface. A charged electrolyte is then spread over the sample, followed by distributing oppositely charged polystyrene (PS) spheres from a solution. The opposite charges on the spheres and in the electrolyte cause them to stick together, however the spheres themselves are repelled from

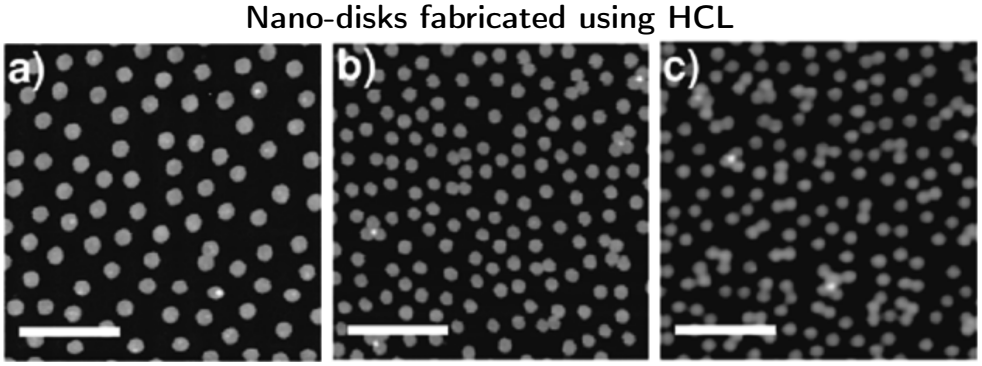

Figure 5.1.: SEM micrographs of disks randomly distributed on fused silica substrates with (a) 5 disks/µm^2 (b) 10 disks/µm^2 (c) 15 disks/µm^2 made by HCL. The scale bars in the SEM images correspond to (a) 1 µm (b) 1.5 µm and (c) 2 µm. The samples where fabricated by the group of Prof. Alexander Dmitriev at the Chalmers University of Technology in Gothenburg and the SEM images were taken at the MPI for solid state research in Stuttgart.

each other. Electrostatic attraction and repulsion cause the spheres to form a pattern with short-range order [99]. Not attached spheres and residual solvent are rinsed away. Afterwards a thin masking layer is evaporated onto the sample. By tape-stripping the PS spheres are removed, leaving a hole-mask on top of the PMMA sacrificial layer. With an oxygen plasma the uncovered PMMA is etched away and the mask can be used for lift-off. Through the holes the material of interest is evaporated onto the substrate, followed by lifting-off the mask using a remover for the sacrificial layer. The result is a large area covered by randomly distributed disks.

The size distribution of the disks depends on the size distribution of the polystyrene spheres, and the next-neighbor distance is defined by the particle density in the solution. In Fig. 5.1 three HCL results are shown with different disk densities ρ_{disks} (5 disks/µm^2, 10 disks/µm^2 and 15 disks/µm^2).

5.2. EBL nanodisks

For large areas, EBL is time-consuming and economically ineffective due to the sequential fabrication. Nevertheless, EBL features a high degree of control compared to HCL. In order to compare HCL and EBL, I fabricated ordered and randomly distributed disk arrangements with the same structure density

like the HCL samples (5 disks/µm^2, 10 disks/µm^2 and 15 disks/µm^2).

5.2.1. Pattern design

The ordered nanodisks arrays were designed using a square lattice, with a lattice constant a given by,

$$a = \frac{1}{\sqrt{\rho_{\text{disks}}}}, \tag{5.1}$$

where ρ_{disks} is the density of disks per square micron. At each point of the 1.5 mm × 1.5 mm grating, a disk with a diameter $d = 190$ nm is placed. To improve the homogeneity, proximity effect correction (PEC) was also applied at the edge of the pattern.

The pattern design for the randomly distributed disks was more time-consuming. As the first step, the boundary conditions have to be set. I decided to limit the minimum distance of two disk edges to be no less than 20 nm in order to minimize the formation of dimers. The algorithm for positioning the disks was developed together with my former colleague Dr. Moritz Esslinger. We generate two random numbers used as x and y coordinates and check if another disk is in the distance diameter plus 20 nm. If no other disk is in the precaution distance the coordinates are saved, otherwise they are dismissed. The whole process is repeated until the desired density is reached, meaning the counter of saved coordinates reaches the total number of disks for the design area. Especially for the dense structures it is possible that the planed number of disk does not fit into the area because of the not optimal order. As a stopping condition a counter is used to terminate the algorithm after a certain number of unsuccessful retries. The large area necessitates to divide the pattern into smaller pieces, allowing parallelization. To avoid overlaps at the boundaries of the segments a further condition is introduced into the code, whereby the distance of the disk edge to the field border has to be at least 10 nm. This condition leads to a small gap of 20 nm between the segments, however this is no issue, since the whole 1.5 mm×1.5 mm pattern area is divided only into 9 fields.

After creating the pattern, BEAMER is used for the PEC. The PEC is needed to achieve equal disk sizes over the whole exposed area. Due to the varying nearest-neighbor distance of the disks, the deposited dose in the short- and mid-range is inhomogeneous and therefore those contributions have to be taken into account during the PEC. BEAMER is used for the fracturing and the export of all data into the machine readable format, too. During the fracturing the designed pattern is decomposed into rectangles and trapezoids, which are

the building blocks our EBL-tool can expose. To improve the circularity of the disks a special fracturing method is used provided by BEAMER.

5.2.2. Sample fabrication

After creating the exposure files the sample is fabricated. As substrate, a 1 cm^2 large piece of high quality fused silica is employed to guarantee proper optical transparency over a large wavelength range [100]. As resist a PMMA bilayer is used to facilitate the lift-off as explained in section 3.2.1. The bottom layer is a 140 nm thick PMMA layer with $M_w = 200$ k covered by a 60 nm thick PMMA layer with $M_w = 950$ k. After spin coating the resists, the sample is covered with a conducting and water-soluble polymer (Espacer 300Z from Showa Denko) to prevent charging.

Subsequently, the sample is exposed, which takes several hours, due to the large covered area. Before developing the resist, the conducting polymer is removed by water. The developer is a mixture of MIBK:IPA 1:3 and the sample is immersed for 15 s. After development, the sample is rinsed for another 15 s in IPA to stop the development process. Finally, the sample is dried with compressed nitrogen.

Since the coverage for the pattern with $\rho_{\text{disks}} = 15\,\text{disks}/\mu\text{m}^2$ is close to 50 % the process window is diminished by the PE. The higher coverage compared to the other two designs causes an increased background. PEC is used to compensate the pattern, however the ratio of the deposited energy between the exposed disks and the background can only be slightly improved. In order to get the desired disk size the dose has to be sufficient to deposit the correct amount of energy in the disk to develop the resist. This causes a lower limit for the dose. As a consequence the lowest achievable background is limited by the coverage and the explained lowest possible dose still producing the correct disk size in the resist.

The ratio between the energy deposited in the exposed regions and the background transfers via the contrast curve into the process window. Due to the high coverage for the $\rho_{\text{disks}} = 15\,\text{disks}/\mu\text{m}^2$ pattern the contrast has to be increased to achieve the desired disk diameter. One of the fabrication aims is to have all patterns on one substrate, therefore I decided to use an undersize-overdose process scheme as explained in section 4.4 in order to improve the contrast.

In the next step the sample and two W boats filled with Ti and Au are mounted into the evaporation chamber. By resistive heating the material is melted and evaporated. The first layer is 1 nm Ti for a better adhesion, followed by 30 nm Au as the functional layer. To remove the residual material the sample

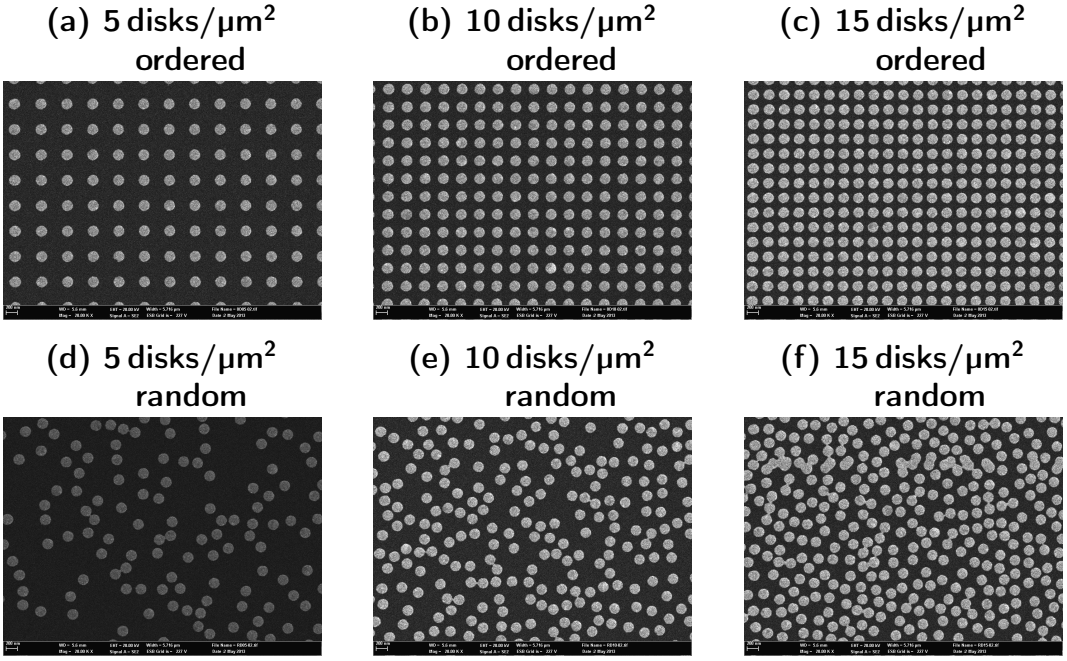

Figure 5.2.: (a) to (c) Ordered nanodisks arrays on a square lattice. (d) to (f) randomly distributed nanodisks fabricated by EBL. All SEM images are from the same sample. The disks are fabricated on a fused silica substrate with different disk densities, (a)+(d) 5 disks/µm^2, (b)+(e) 10 disks/µm^2, (c)+(f) 15 disks/µm^2.

is immersed in the remover NEP for three hours at 80 °C. After rinsing the sample in acetone and IPA, it is dried with compressed nitrogen. Images of all six pattern of ordered and randomly distributed disks with three densities each, are presented in Fig. 5.2.

5.3. Sample comparison

Investigating the SEM images of the HCL samples in Fig. 5.1 and the random samples in Fig. 5.2(d) to Fig. 5.2(f) the overall sample quality seems to be good and equivalent. While the circularity of the disks and their size distribution depend on the PS spheres and the evaporation angle for the HCL sample, EBL rely on the mentioned fracturing.

Comparing the low-density pattern fabricated by HCL (Fig. 5.1(a)) to its EBL counterpart (Fig. 5.2(d)), the former appears to be more evenly distributed. This sort of short-range-order is known and was attribute to the electrostatic

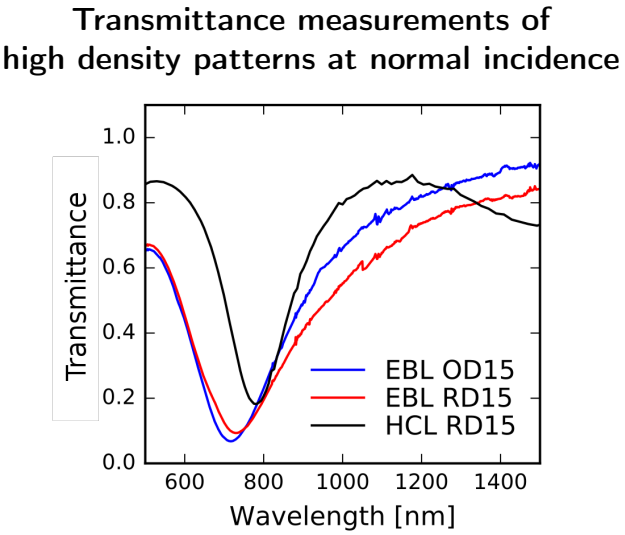

Figure 5.3.: Transmittance spectra measured for the HCL, the ordered and randomly distributed EBL samples with a disk density of 15 disks/µm^2.

repulsion between the charged PS spheres [99]. For higher disk densities the samples are looking equivalent. The images taken from the EBL random pattern appear to show fewer agglomerations of disks, neglecting one line in Fig. 5.2(f), which might be caused by field stitching during the exposure.

5.4. Optical transmittance measurement

The transmittance measurements presented in this section were performed in the department of Prof. Dressel at the University of Stuttgart using a Wollam variable-angle spectroscopic ellipsometer (VASE). All measurements are done by my collaborator Dr. Stefano De Zuani.

In Fig. 5.3, transmittance measurements at normal incidence for all three samples with a density of 15 disks/µm^2 are presented. The dip in transmittance is attributed to absorption due to the localized surface plasmon resonance (LSPR) of the disks. The LSPR peak mainly depends on the size, shape, material properties of the nano-particles as well as the surrounding material [18]. A different wavelength of the minimum is observed for the sample fabricated by HCL compared to those made by EBL. This difference can be explained by a deviation in the disk diameter. The ordered and random EBL pattern seem to have the resonance at almost the same position, which emphasizes the

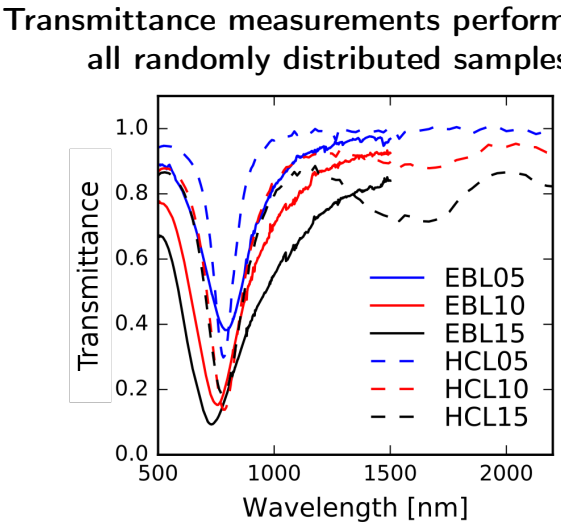

Figure 5.4.: Transmittance measurements for all randomly distributed samples fabricated by HCL (dashed line) or EBL (solid line).

quality of the fabrication process, especially the PEC.

Comparing the spectra taken from the EBL fabricated pattern, the observed resonances are almost identical. The absorption for randomly distributed disks for larger wavelength is higher. This broadening of the resonance peak might be explainable by the varying nearest-neighbor distance. The different distances between the disks lead to differences in the coupling of the resonators and therefore to a broader spectrum.

The transmittance spectra taken at normal incidence for all random pattern are presented in Fig. 5.4. All three HCL samples appear to have their resonance at the same wavelength, which is not the case for the EBL samples. This suggests a better disk uniformity in the HCL sample than in the EBL one.

Having a closer look at the infrared part of the spectra it appears that the HCL samples show a second dip in the transmittance. This dip might be caused by another LSPR originating from disk agglomerations. With decreasing disk density the dip is getting shallower and disappears for the lowest density. This supports the trend already observed in the SEM images shown in Fig. 5.1. Since the dip is not present in the EBL samples at all, the impression taken from the SEM pictures depicted in Fig. 5.2(e) to Fig. 5.2(f) is confirmed: The EBL samples show only a negligible amount of dimers. The forming of dimers was suppressed by design as explained in section 5.2.1. Nevertheless our algorithm allows gaps between the disks as small as 20 nm, however it became increasingly

difficult achieving the required disk density preventing dimers.

5.5. Conclusion

The sample quality of both approaches, HCL and EBL, is comparable and very high. While HCL offers a higher disk uniformity, EBL is able to prevent the formation of dimers more effectively. By improving the fracturing of the disks and by using the undersize-overdose approach to increase the development contrast for the sparser patterns, too, it might be possible to get a more uniform disk size with EBL, too. The presented EBL samples were fabricated using PEC to reduce the deposited energy background and to compensate for local fluctuations in the deposited energy caused by the locally inhomogeneous disk distribution. A reduced background provides an improved control of the disk size and the correction of local energy inhomogeneities prevents the formation of dimers. Comparing the variability of the compatible materials, both approaches are equal, however for the large-area fabrication HCL is much more cost- and time-effective. If a suppression of dimers or control of the disk positioning is necessary, EBL is advantageous.

6. Optical properties of quasi-films

Hövel *et al.* discussed in their work [101] the optical behavior of gold thin films at the percolation threshold. When gold is evaporated onto a substrate, the film growth starts with a formation of small islands. By depositing further material, the islands grow until they touch each other and form a percolating network. The changeover from isolated islands to a conducting network is abrupt and the transition is called percolation threshold. Densely packed nano-structures close to percolation are interesting for second-harmonic-generation of light (SHG) [102, 103]. For SHG, the field enhancement between the particles is used to double the frequency of the incident light. Besides this application, it is interesting to study the transition itself. For example, the influence on the optical properties of gold at the threshold have been studied [101].

In collaboration with the department of Prof. Dressel at the University of Stuttgart we investigated metal quasi-films at the percolation threshold using optical methods. Prof. Dressel *et al.* are experienced in this field and have expertise in ellipsometric measurements. The aim of this collaboration is to analyze ordered patterns at the percolation threshold fabricated using EBL in contrast to the self-assembled islands, that have been studied before. My part in this collaboration is the fabrication of the densely packed metal quasi-films.

Angle-resolved optical investigations rely on a collimated beam. Focusing the beam with a high numeric aperture causes an averaging over all angles of incidence (AOI)s in the focus spot and therefore a loss of the angle information. The collimated beam of the Wollam VASE employed in this work is $d_{\mathrm{beam}} \approx 1\,\mathrm{mm}$. In order to measure only the patterned area and avoid background from the closed metal film, the patterned region has to have a size of several square millimeters. To simulate the crossing of the percolation threshold with defined and shape-controlled pattern, small gaps are needed like they occur during film growth. Especially the combination of large-area fabrication and high resolution as well as shape control is challenging. On one hand, the large area to be patterned requires a process with high sensitivity and high exposure currents to fabricate the samples in finite time. On the other hand, the pattern density and necessary resolution require a high-contrast process.

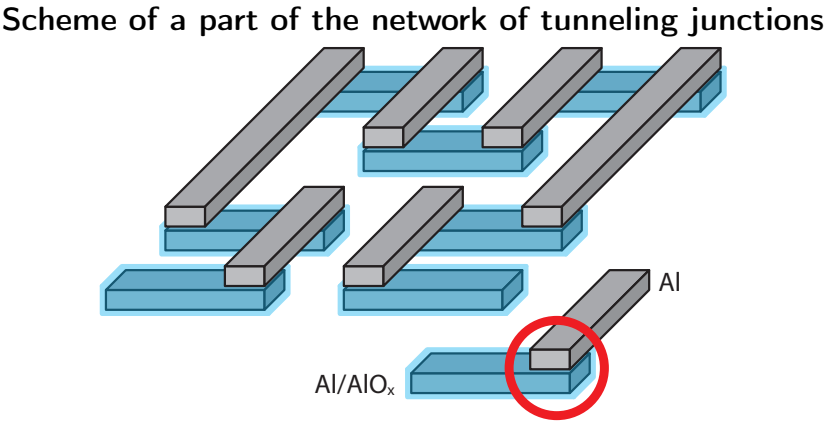

Figure 6.1.: Scheme of a part of the network of Al/AlO_x tunneling junctions following a Hilbert curve. In the lower right corner is a single Al/AlO_x tunneling junction depicted. During the fabrication the first contact is defined by evaporated aluminum. Followed by oxidizing the contact and finished by evaporating the second Al contact. The red ring highlights the actual Al - AlO_x - Al - tunneling junction. In the network all Al - AlO_x - Al - transitions form tunneling junctions.

6.1. Network of tunneling junctions

Our plan is to mimic the crossing of the percolation threshold by using a large-area network of tunneling junctions. In comparison to the evaporated thin films, the tunneling junctions of the EBL structured network correspond to the gap of the isolated metal islands. By changing the tunnel barrier, the resistance and the capacitance of the junction are changed. The threshold is crossed once the total current is dominated by the leakage, rather than by the tunneling.

6.1.1. Aluminum/aluminum-oxide tunneling junctions

Tunneling junctions can be created by fabricating a sandwich structure of Al and AlO_x. By connecting junctions a network can be created, as shown in in Fig. 6.1. The junction is fabricated by evaporating aluminum in an ultra-high-vacuum (UHV) evaporation chamber to avoid uncontrolled oxidation. Afterwards the sample is transferred into the oxidation chamber connected to the evaporation chamber maintaining the vacuum quality during the transfer.

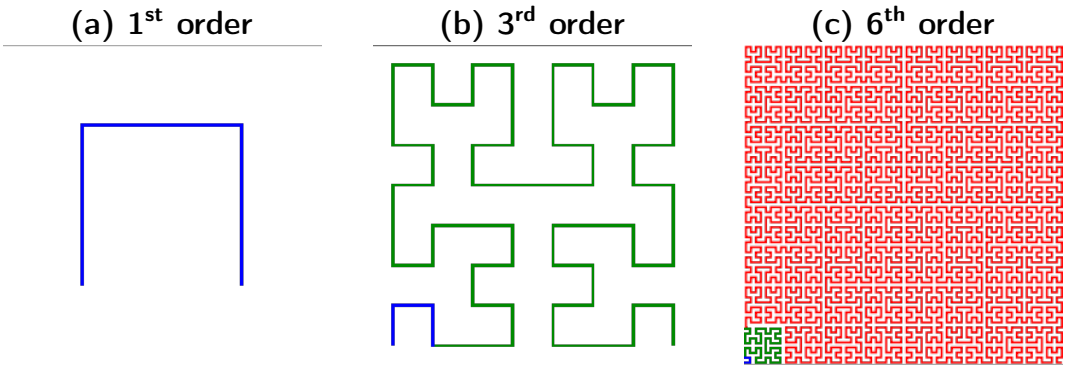

Figure 6.2.: Three different orders of the Hilbert curve to demonstrate the approximation of the square. a) first b) third c) sixth order. Since these images are generated using a recursive algorithm the order correspond the recursion depth. To emphasize the recursivity of the Hilbert curve in the higher order patterns a part is colored corresponding to the lower order patterns.

Depending on the oxygen pressure and oxidation time, the AlO_x tunneling barrier thickness is controlled. To finalize the junction, the second Al contact is evaporated on top, again in the evaporation chamber.

6.1.2. Hilbert curve

To connect the tunneling junctions, we choose the Hilbert pattern, which is a continuous fractal space-filling curve. It is able to approximate every point in a square infinitely close [104] (see Fig. 6.2) and is therefore useful to create a dense network of tunneling junctions. Since the Hilbert curve is continuous, a theoretical possibility exists to measure a non-zero DC conductivity. A finite conductivity is an indicator for a percolating network [101].

6.1.3. Shadow evaporation

The aim is to use the Hilbert pattern as a lattice for the tunneling junctions. By utilizing a shadow evaporation it is possible to separate the fabrication of the network into two evaporation steps by writing only one pattern by EBL. This evaporation technique uses a large resist aspect ratio and a tilt between the sample and the evaporation source. If the rotation and tilt angle of the sample is adapted to the pattern and resist aspect ratio, the substrate can be coated selectively. Trenches parallel to the plane of incidence of the material

beam are filled, while the bottom of perpendicular grooves is not reached by the material flux. This process is depicted in Fig. 6.3(a).

As a side effect of the evaporation angle and the resist height, an undesired shadow is caused by the end of the trench on the side closer to the evaporation source. To compensate this shadow, the lines in the pattern design are extended into that direction. Unfortunately, the same extensions limit the density of the network, since a thin separation is always needed, otherwise the result would be a fish net instead of a Hilbert curve. The resulting pattern with line width of 50 nm and minimum length of 150 nm plus the extensions is presented in Fig. 6.3(b). Since material only reaches the substrate in trenches parallel to the evaporation direction, in the first evaporation step one contact is created, then the Al is oxidized in a controlled manner and the sample is rotated by 90° within the tilted plane. Afterwards, the second contact is evaporated, which is orientated perpendicularly to the first contact and a network of tunneling junctions is formed.

6.1.4. Sample preparation

The substrate is a doped silicon wafer covered with 300 nm thermally grown silicon-dioxide. The SiO_2 layer leads to an insulating surface which is necessary for the optical investigation of the metallic nano-structures on top of the substrate. Without the insulating SiO_2 the metallic pattern would be short-circuited by the doped Si substrate.

For EBL, insulating substrates are disadvantageous. Electrons stopped within an insulating layer cannot be drained off, therefore building up a charge cloud. Depending on the amount of accumulated charge the lithography can be influenced negatively. It is actually possible to get a discharge. In our case the insulating layer is rather thin hence the probability for the electrons to be stopped within this layer is low. The doped bulk material underneath the thin insulating layer is conducting and can drain off the electrons to the grounded sample holder. In this configuration no considerable charging was observed.

On top of the Si/SiO_2 substrate, a 120 nm thick single layer of PMMA $M_w = 950\,\mathrm{k}$ is coated. The resist thickness is a compromise between pattern extension, evaporation angle and resolution. By increasing the resist thickness, the angle between the evaporation direction and the surface normal can be smaller, allowing shorter pattern extensions. Thicker resist can cause resolution limitations because of the increasing aspect ratio of resist and exposed features.

After spin coating the resist, the sample is transferred into the EBL tool and a higher order Hilbert curve with the green extensions shown in Fig. 6.3 is exposed into the resist. The pattern has to cover several mm^2, since the spot

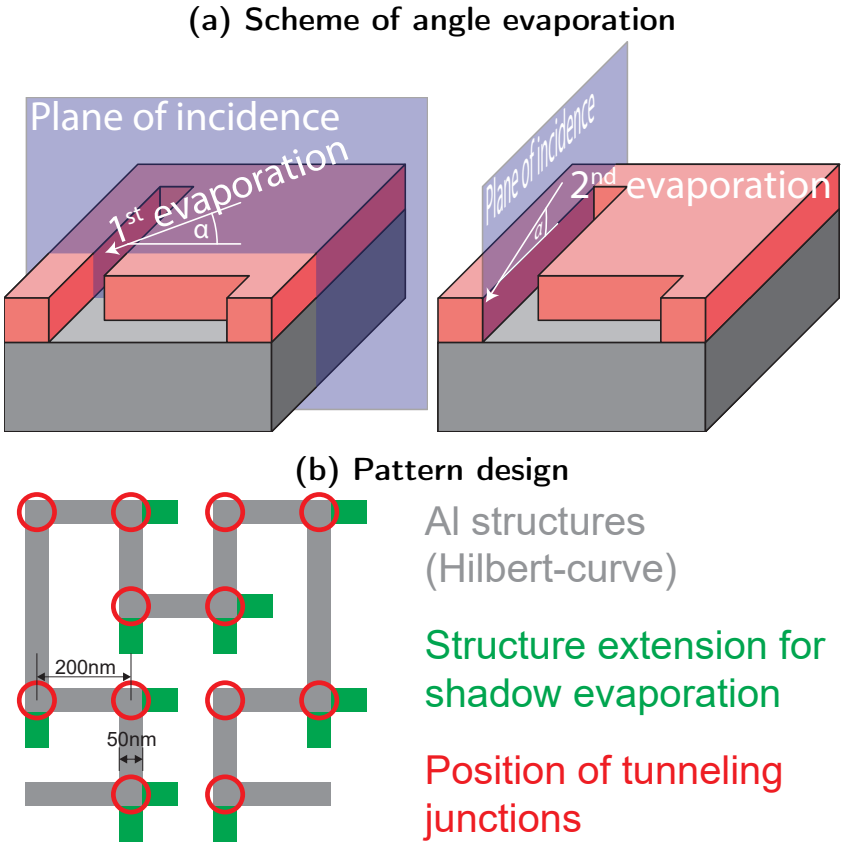

Figure 6.3.: (a) Cross-section of two high aspect trenches in the resist one parallel and one perpendicular to the evaporation direction. By choosing the right evaporation angle, only one of the trenches is filled with metal. (b) Scheme of the final exposure pattern with extensions for compensating the shadows in evaporation direction.

size of the ellipsometer, which will be used to investigate the sample later on, is about 1 mm in diameter. For the pattern definition I developed a recursive algorithm to generate a list of coordinates describing the pattern. The exposure is performed using a current of $I = 1\,\mathrm{nA}$ as a compromise between resolution and writing speed.

The exposure is followed by developing the resist in a 1 : 3 mixture of MIBK and IPA. To improve the contrast and to increase the process window I try cold development as explained in section 3.1.3 [105]. Mohammad *et al.* found an optimum development temperature at $T = -15\,^{\circ}\mathrm{C}$ for MIBK:IPA. I adjust the temperature of the developer in a beaker in a salt water reservoir cooled

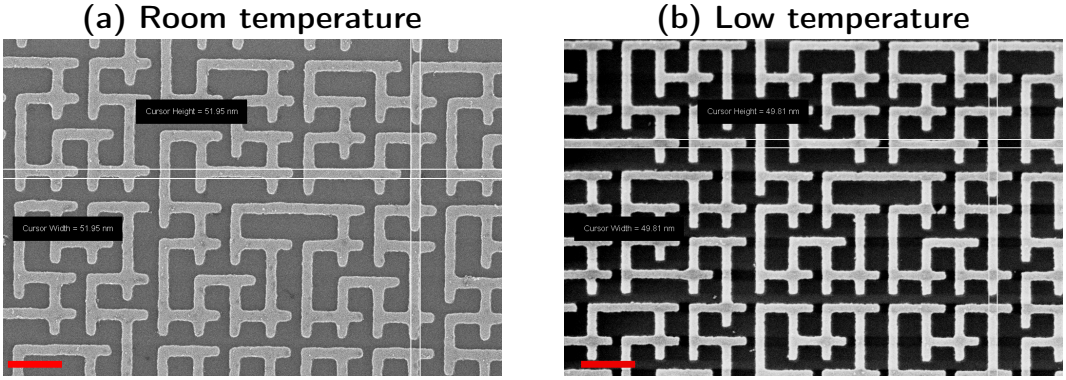

Figure 6.4.: (a) SEM micrograph of the center of a sample processed at room temperature. (b) Center of the same pattern developed at $T = -15\,°C$. The red scale bar corresponds to 300 nm.

by dry ice. To further increase the contrast, the development time is kept short ($t = 5\,s$). The improvement of pattern fidelity by cold development is shown in Fig. 6.4 by comparing two samples fabricated using normal incidence during metal deposition followed by lift-off. Fig. 6.4(a) shows a micrograph of the lithography of the center of a 100 µm test pattern developed at room temperature. In comparison the pattern in Fig. 6.4(b) was developed at $T = -15\,°C$ and shows significant improvement. The corners of the pattern are sharper for the sample developed cold, which indicates a higher contrast. After immersing the samples in MIBK:IPA, the development is stopped by rinsing for 15 s in IPA and dried with compressed nitrogen.

In the next step, the sample is transferred into the UHV evaporation chamber. For the first aluminum contact the sample is aligned so that the trenches are parallel to the expected evaporation direction and the evaporation angle relative to the sample surface is set to $\alpha = 36°$. After evaporating the first 40 nm thick Al layer, the sample is transferred into the oxidation chamber and oxidized for 20 min in a pure oxygen atmosphere at a pressure of $1.6 \cdot 10^{-1}$ mbar. Afterwards the sample is moved back into the evaporation chamber and turned by 90° within the tilt plane to evaporate Al into the other trenches. At the connection point of two perpendicular trenches a tunneling junction is formed.

Finally, the sample is transferred from the evaporation chamber into a beaker with NEP for the lift-off. To dissolve the PMMA the sample is kept in NEP at 80 °C for 2 h, followed by flushing and rinsing the sample several times in acetone and IPA. Afterwards the sample is dried with compressed nitrogen.

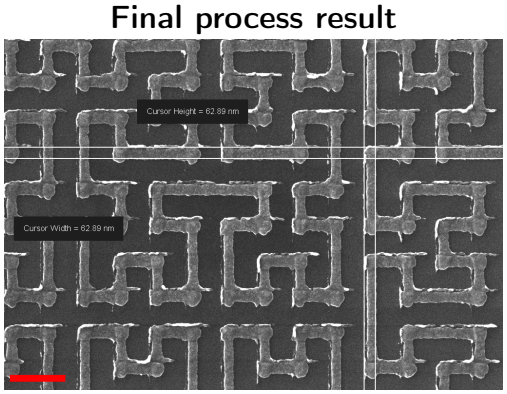

Figure 6.5.: SEM micrograph of a 100 µm × 100 µm Hilbert curve test pattern. The red scale bar corresponds to 300 nm.

6.1.5. Results and discussion

The process result after lift-off is depicted in Fig. 6.5 and is of proper lithographic quality. Only a few undesired residuals remained on the substrate and they are caused by a not exactly parallel adjustment of the exposed trenches and the evaporation direction. Sidewall evaporation leads to some further residuals at the edge of the rectangles. Aside from the residuals the result is promising and the contacts overlap nicely.

Unfortunately, the result is not reproducible. Especially the insufficient temperature control during the cold development and the short development time cause a narrow process window. The dose needed to achieve the correct line width, dose to size (DTS), is not constant. The DTS from one exposure to the next is varying enough to cause a complete lithography failure using the DTS estimated from the first dose test in the second exposure. In a nutshell the DTS variation is larger than the process window. This large spread of the DTS is an issue, since the final pattern has to cover several mm^2. Exposing this large pattern several times with different doses to cover the complete observed DTS range would exceed the acceptable writing time.

In retrospect, a better temperature stabilization during development and an increased development time could improve the process stability. Also, using a different developer, such as a co-solvent system (water and IPA) or undersize-overdose could increase the contrast enough to eliminate the need for cold development. To facilitate a DC measurement of the network, a state-of-the-art proximity effect correction (PEC) was performed. Several months after these discussed experiments I got access to the Monte-Carlo simulation (MCS)

package PENELOPE and was therefore able to calculate numerical point spread functions (PSF_zs). With the help of the simulated PSF_zs an improved PEC is possible. All issues together led me to abandoning this approach of investigating the percolation threshold with an ordered pattern of tunneling junctions.

6.2. Patterned quasi-films

The second approach to fabricate structures to investigate the percolation threshold aims at densely packed nano-particles. Due to the small gaps, the percolation of the metal film is suppressed. With the periodic and uniform patterned film I fabricated, my collaborator Dr. Stefano De Zuani investigated the optical behavior of film consisting of squares ranging from 100 nm up to several microns edge length. For all investigated samples the squares are closely packed, with a separation in the range of a few tens nanometers.

6.2.1. Concepts and design

In order to realize this approach I designed a large area pattern of squares separated by a minimal gap. For the process development a designed edge length $l = 100\,nm$ and a gap $w = 4\,nm$ was chosen, resulting in a pattern filling factor of 92 %. Exposing such a pattern using a positive tone resist would cause a long writing time and a high dose background due to the PE. The dose ratio between exposed and unexposed areas would be small requiring a exceptional high-contrast process to avoid loss of pattern details. In order to mitigate these issues a negative tone resist was used decreasing the filling factor and thereby the exposed area to 8 %. I decided to use the negative tone resist HSQ for this process. The cross-linked resist can be removed with HF-containing etchants, causing an incompatibility to for example glass substrates. To overcome this issue a sacrificial PMMA layer is introduced underneath the HSQ. The combination of HSQ and PMMA merges the high-resolution capabilities of HSQ with the organic solvent possibilities of PMMA [32]. A detailed explanation of the assets and drawbacks of HSQ as well as different HSQ bilayer systems can be found in section 3.1.4.

Due to the needed pattern inversion, the gaps are written instead of the squares, resulting in a fishnet like pattern. The gap width is chosen to be equal to the distance between two exposure shots. This forces the EBL tool to expose a single line, however I am still able to use an area dose for writing. Unfortunately not all EBL systems offer the possibility to set a line dose, therefore I chose to use an area dose. By forcing the tool to expose a single

pixel line, the highest resolution can be achieved, further I am able to control every shot during the exposure. A resolution-limiting factor for exposing single-pixel lines is the beam diameter, which depends on the beam current. The beam current of $I = 1\,\mathrm{nA}$ causes a beam diameter of approximately $d_{\mathrm{beam}} \approx 5\,\mathrm{nm}$ and guaranties an appropriate throughput.

Due to the uniformity and the large area covered by the pattern the PE causes an elevated uniform background exposure generated by the backscattered electrons. At the boundary of the pattern in a 50 µm to 100 µm wide region this background is decreasing towards the pattern edge. The pattern is at least $1.5\,\mathrm{mm} \times 1.5\,\mathrm{mm}$ in order to achieve a good signal-to-noise ratio by maximizing the patterned area in the region probed by the ellipsometric measurement using a collimated beam with 1 mm diameter. Due to the homogeneity of the background in the majority of the exposed area (everywhere besides in the boundary of the pattern) and the averaging caused by the large area measured simultaneously by the ellipsometer, no PEC was performed. Only the background exposure is considered by choosing a proper dose to achieve the desired gap width in the film. The large area averaging measurement using the ellipsometer is not going to be influenced by the negligible degradation of the pattern quality by skipping long-range PEC for the pattern boundary.

The observed short-range effects caused by the structure density change at the crossings are accounted for by skipping the shot at the crossing point, and the dose is gradually increased from the crossing. This local dose variation is possible by applying a multi-pass exposure, thereby the total dose is divided by the number of passes (in my case four), and the pattern is written four times. For each pass the exposed line is shifted by one nanometer in the direction of the line to compensate for the 4 nm shot pitch, improving the line-edge-roughness. The multi-pass exposure technique compensates small fluctuations in the beam positioning by averaging and thereby increasing the pattern fidelity.

6.2.2. Sample preparation

A doped silicon wafer with a thermally grown, 300 nm thick SiO_2 top layer was used as a substrate. The insulating surface is necessary for the optical measurements, and the conducting bulk prevents the decelerated injected 100 keV electrons to build up a considerable background charge.

To apply the bilayer resist system on the substrate, two sequential steps of spin coating are necessary. First, the substrate is covered with an 80 nm-thick sacrificial layer of PMMA with a $M_w = 950\,\mathrm{k}$, followed by a 4 min pre-exposure bake at 160 °C on a hotplate to prevent resist intermixing. This step is crucial since HSQ is dissolved in MIBK which is a developer for exposed PMMA. By

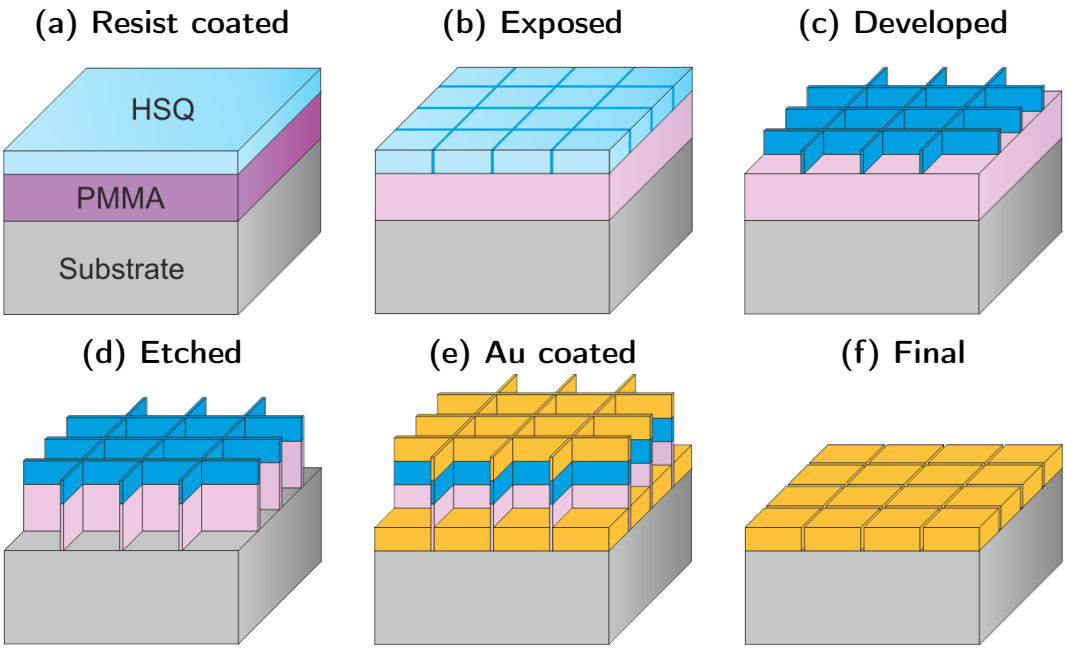

Figure 6.6.: Schemes of the fabrication steps of the HSQ PMMA bilayer process in sequential order. a) coated sample, b) exposed resist, c) development result, d) resist-covered sample after oxygen plasma etching of PMMA, e) metal distribution after evaporation, f) result after lift-off by dissolving the PMMA.

the use of the described baking procedure, the remaining solvents in the PMMA layer are removed and its stability against organic solvents is increased.

In a second spin coating step, a 30 nm-thick HSQ film is applied on top of the PMMA layer. A scheme of double-layer resist on the substrate is depicted in Fig. 6.6(a).

After finishing the coating the sample is transferred into an EBL system without any further treatment (see Fig. 6.6(b)). Since the exposed lines are narrow, a particularly high dose is necessary [106, 107]. We use a dose in the range of $D = 8000\,\mu\mathrm{C\,cm^{-2}}$ at an acceleration voltage of $V_{\mathrm{acc}} = 100\,\mathrm{kV}$.

The exposure is followed by the development of the HSQ top layer in Microposit MF322 (see Fig. 6.6(c)), which results in a fishnet-like grid. By optimizing the development time, the smallest gaps are observed for $t_{\mathrm{dev}} = 80\,\mathrm{s}$. To stop the development, the sample is rinsed in an overflow bath filled with deionized water for $t_{\mathrm{rinse}} = 30\,\mathrm{s}$. Using any organic solvent for rinsing would dissolve the PMMA immediately, as the PMMA is strongly overexposed.

In order to transfer the HSQ mask into the PMMA, an oxygen plasma in RIE tool is used. A scheme of the resulting resist structure is shown in Fig. 6.6(d). Since RIE is an advanced technique capable of selectively removing material it is the method to use for anisotropic ashing of the sacrificial layer. In contrast to Yang *et al.* [83], who used pure oxygen plasma, I apply an oxygen/argon plasma (1 : 1). As an oxygen plasma is highly reactive and therefore oxidizes PMMA efficiently the etch rate can be reduced by diluting the etching gas atmosphere with argon. Besides negligible physical sputtering Ar is not etching PMMA. The plasma etching step has to be optimized to generate as steep as possible sidewalls to prevent sidewall deposition during the metal deposition and to avoid an undercutting which would destabilize the resist structure. To achieve steep side walls in our Leybold LE301 RIE system we are using a low base pressure ($p = 3.6 \cdot 10^{-6}$ bar), RF-power of $P = 99$ W and a flow of $f_{\text{gas}} = 15$ sccm for each process gas.

Afterwards, metal is deposited on the sample by thermal evaporation depending on the desired application. In my case it was a nominally 5 nm thick Ti adhesion layer followed by 20 nm Au. As sketched in Fig. 6.6(e), the thickness of the evaporated material has to be substantially thinner than the PMMA layer thickness to execute the lift-off process successfully.

Finally, to dissolve the PMMA layer and to remove the HSQ mask with the metal, the sample is immersed in NEP at 80 °C for 1 h and sonicated for another 10 min (see Fig. 6.6(f)). To improve the lift-off result further ultrasonic cleaning is done and finally a special brush is used to gently remove the last persistent residuals.

6.2.3. Lithographic results

With the process parameters described above I was able to achieve the resolution down to the sub-10 nm regime. Fig. 6.7 shows images of a processed gold pattern on a Si/SiO_2 substrate. The structures consist of 100 nm squares with a gap smaller than 10 nm (see Fig. 6.7(c)). Fig. 6.7(b) emphasizes the large area uniformity. A square sample with an edge length of a 5 mm × 5 mm was fabricated, and an overview is shown in Fig. 6.7(a). The visible non-uniformities and field borders are machine dependent negligible changes in the pattern periodicity optically amplified by interference. Those irregularities were not observable and measurable in the SEM.

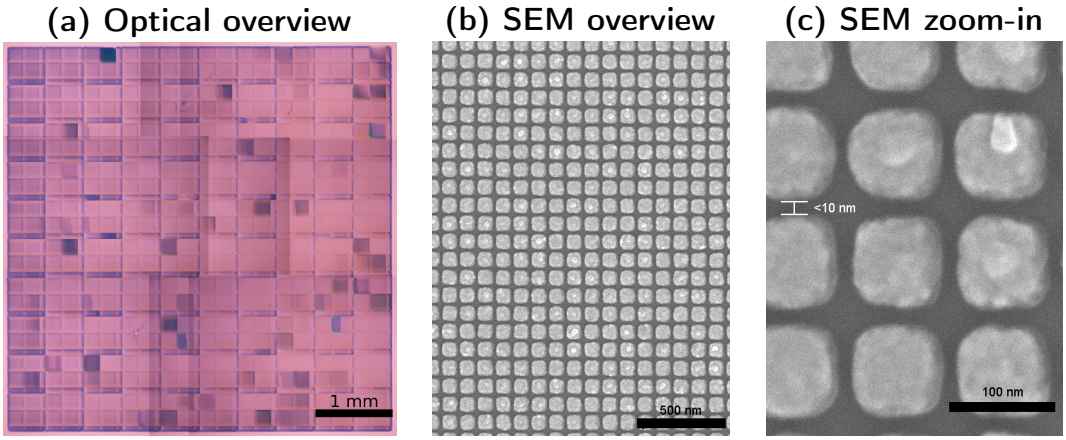

Figure 6.7.: (a) Light microscopy overview image of a 5 mm × 5 mm large area fabricated with the described bilayer process. (the image is combined of several overlaid pictures) (b) SEM micrograph of a small cutout of the processed sample emphasizing the pattern uniformity. (c) Zoom in into (b) proofing the achieved resolution.

6.2.4. Measurements and results

My samples contain large areas of squares and are measured optically in the department of Prof. Dressel at the University of Stuttgart. Most of the measurements are performed by my collaborator Dr. Stefano De Zuani and some I measured myself. The discussions are promoted and pushed further by Dr. Audrey Berrier and Dr. Bruno Gompf. Later presented simulations are performed and checked by Dr. Helga Kumric and Dr. Audrey Berrier [36, 37].

Measurement technique

The measurements are performed using a Wollam VASE with a Hg lamp as light source for measurements up to $\lambda = 2450\,\text{nm}$ and a Bruker Fourier-transform infrared spectrometer for measurements with a wavelength $\lambda > 2450\,\text{nm}$. For the measurements the wavelength λ is swept from visible to infrared. The VASE selects λ by a computer-controlled monochromator using two sets of gratings, one for the visible and one for the infrared regime. The monochromatic light is sent through a multi-mode optical fiber to detach the light generation from the goniometer. During the λ sweep the angle between light source and detector is kept constant. To preserve the information about the direction of $\vec{k}$, a collimated beam is used to illuminate the sample with a diameter of approximately $d_{\text{beam}} \approx 1\,\text{mm}$. As stated in the beginning, this spot-size is the

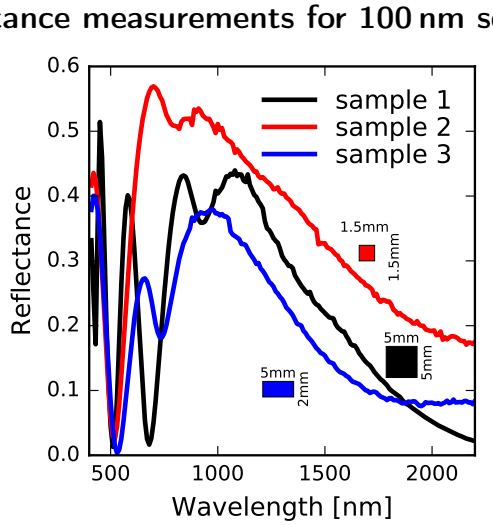

Figure 6.8.: Reflectance measurements (AOI $\alpha = 30°$) of all three samples patterned with squares of nominal 100 nm edge length. The structured area varies from sample to sample indicated by the color coded rectangles. (black: 5 mm × 5 mm, red: 1.5 mm × 1.5 mm and blue: 5 mm × 2 mm)

reason for the large patterned areas I fabricate. Focusing the beam would lead to an averaging over all AOIs causing a loss of information. Illuminating a small patterned area with a large spot would cause a lot of background noise originating from the illuminated not patterned regions. Due to the doped silicon wafer as substrate transmission measurements are not possible, therefore all presented data are captured in reflection with s-polarized light, unless stated differently.

Results and discussion

Three different batches of my samples are measured, all of them have the same material stack. The substrate is an n-doped silicon wafer covered with a 300 nm silicon-dioxide layer. By thermal evaporation a nominally 5 nm thick titanium adhesion layer followed by 20 nm gold are deposited. In Fig. 6.8 reflectance measurements are presented for areas covered by squares with a nominal edge length of 100 nm. Depending on the illuminated patterned area and the sample quality the results differ quantitatively. These measurements indicate that the patterned area of sample 2 might not be large enough. For

an AOI $\alpha = 30°$ the beam diameter increases along the plane of incidence to $d_{\text{beam}}, 30° \approx 1.15\,\text{mm}$ reducing the margin for the beam placement on the sample during the measurments. The elongated beam might have hit the unpatterned region causing a higher background reflectance. Qualitatively all three samples show the same pronounced reduction in reflectance over a broad frequency range in the infrared regime.

The first sample is a $5\,\text{mm} \times 5\,\text{mm}$ area covered with squares with an edge length of 100 nm. Fig. 6.9(a) shows a reflectance measurement covering different AOIs starting with $\alpha_i = 30°$ up to $\alpha_f = 70°$ and an increment of $\Delta\alpha = 10°$. All spectra show a similar behavior. In the visible range around $\lambda = 500\,\text{nm}$ the reflectance is decreased due to a surface plasmon resonance. At larger λ the reflectance increases, reaching a maximum, before decreasing again in the infrared. The reflectance of the smallest measured angle $\alpha_i = 30°$ drops to almost zero at $\lambda \approx 2200\,\text{nm}$. With increasing AOI the minimum in the infrared is getting shallower until it ranges from approximately 800 nm to the end of the measured range for $\alpha_f = 70°$.

Sample 2 consists of a smaller patterned area of $1.5\,\text{mm} \times 1.5\,\text{mm}$ to reduce EBL writing time. It was fabricated to reproduce the measurement results of sample 1 and to investigate the filling factor dependency of the reflectance. Additionally to the area filled with 100 nm squares, several areas filled with 200 nm, 300 nm, 400 nm, 500 nm, 600 nm, 700 nm, 800 nm, 1600 nm, 3200 nm and 6400 nm squares were fabricated.

The angle resolved measurements performed on both samples on the regions filled with 100 nm squares (see Fig. 6.9(a) and (b)) agree qualitatively besides the AOI $\alpha = 70°$. For this AOI sample 2 shows an inverted behavior: the minimum in the infrared regime turned to be a maximum instead. Actually, the measurement results of sample 1 AOI $\alpha = 70°$ and sample 2 AOI $\alpha = 60°$ agree better than the results for AOI $\alpha = 70°$. For an AOI of $\alpha = 70°$ the corresponding beam diameter $d_{\text{beam}}, 70° \approx 2.92\,\text{mm}$. Even with perfect alignment only approximately 65 % of the beam can fit the structured area. The measurement of sample 2 for an AOI of $\alpha = 70°$, which qualitatively behaves like a closed gold film [108], as well as the overall increased reflectance seem to confirm the mentioned hypothesis that the patterned area of sample 2 is too small.

The third sample is covered by several $2\,\text{mm} \times 5\,\text{mm}$ areas filled with 100 nm, 150 nm, 200 nm and 250 nm squares to reproduce the results from the first sample and to study the reflectance dependency of the filling factor using squares below 300 nm. In Fig. 6.9(c) the angle resolved comparison measurements are shown for the quasi-film consisting of 100 nm squares. The curve shapes are close to those we observed on sample 2 however the depth of the minimum is

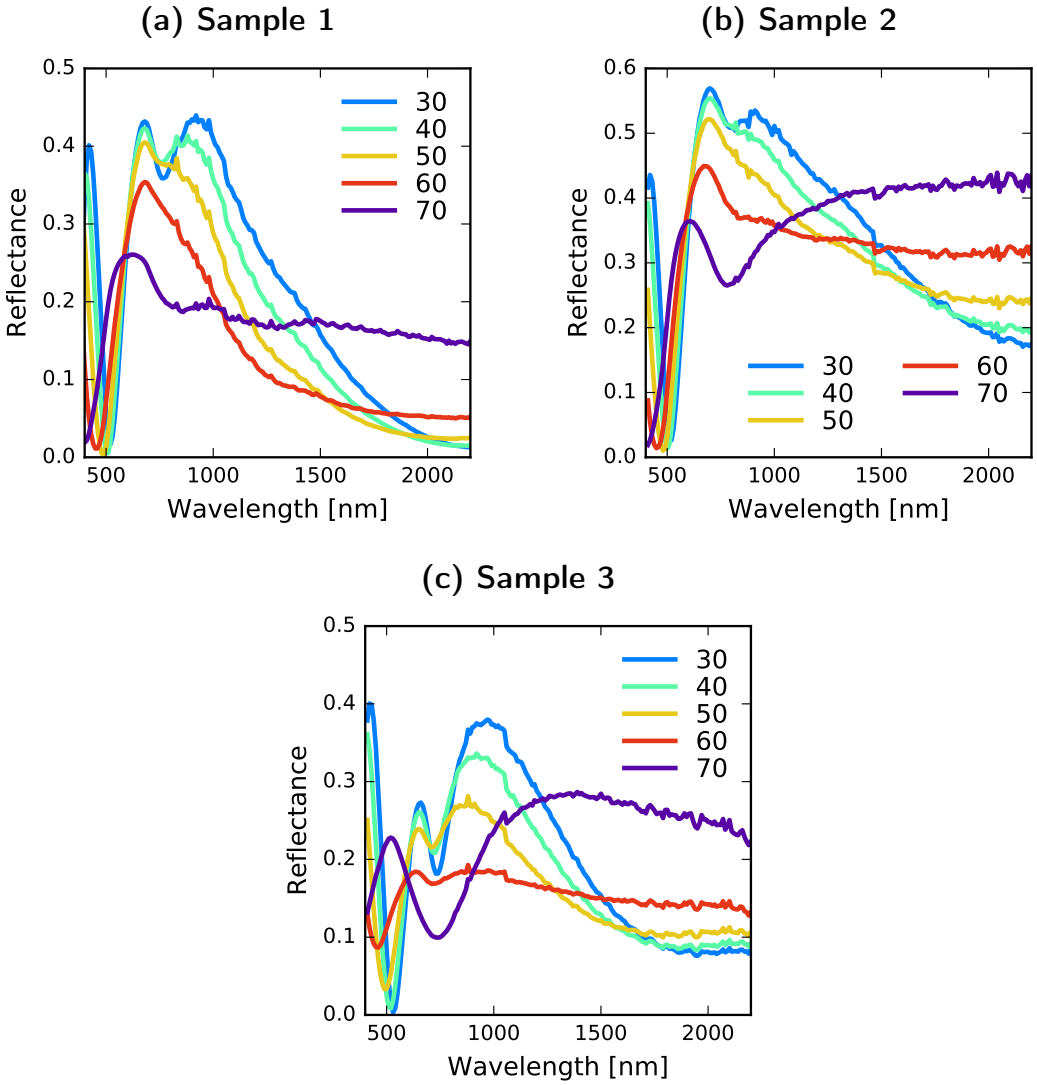

Figure 6.9.: Reflectance measurements performed on sample 1 (a) 2 (b) and 3 (c) for 100 nm squares for all AOIs between $\alpha_i = 30°$ and $\alpha_f = 70°$ in steps of $\Delta\alpha = 10°$ for wavelengths from $\lambda_i = 400\,\text{nm}$ to $\lambda_f = 2200\,\text{nm}$ with $\Delta\lambda = 10\,\text{nm}$.

closer to the results from sample 1.

The plot in Fig. 6.10 are reflectance measurements, with the AOI fixed to $\alpha = 30°$ and several fields each covered with squares of a different sizes. Investigating the measurements for the patterns filled with squares ranging from 100 nm to 300 nm, a steady increase of the minimum in the infrared range

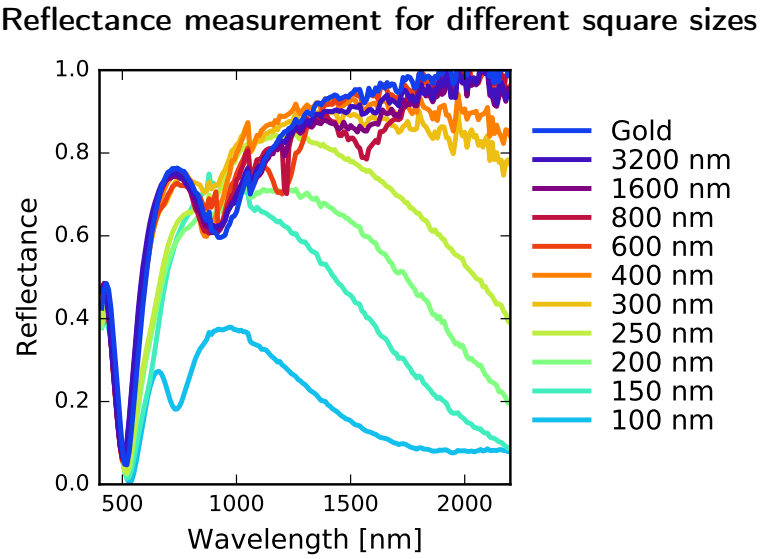

Figure 6.10.: Reflectance data recorded for a fixed AOI $\alpha = 30°$ on sample 2 and 3. Squares sizes in the measured areas range from 100 nm to 3.2 µm. As a reference the unstructured gold film was measured, too.

can be observed. For squares larger than 300 nm the measured reflectance spectra differ not significantly from the reference measured on a closed gold film for the observed measurement range. Complementary measurements spanning from $\lambda_i = 600\,\text{nm}$ to $\lambda_f = 7000\,\text{nm}$ performed and published by De Zuani *et al.* [37] revealed a red-shift of the reflectance minimum for increasing square sizes instead of an increase.

In order to understand the response of the samples, finite-difference time-domain simulations with the software Microwave Studio from CST are performed. With this technique the Maxwell equations are solved for the geometry depicted in Fig. 6.11(a). The material stack is reduced to a gold layer with a thickness of 20 nm in air neglecting the substrate. For the spectral simulation results shown in Fig. 6.11(b) square sizes between $L = 70\,\text{nm}$ and $L = 500\,\text{nm}$ as well as a gap-less film are simulated. The films are excited with a plane wave with an AOI $\alpha = 30°$ propagating parallel to the x-axis. Comparing Fig. 6.10 and Fig. 6.11(b) a qualitative agreement between experiment and simulation can be observed. The simulations can reproduce the increase of the reflectance for square sizes from $L = 100\,\text{nm}$ to $L = 300\,\text{nm}$ converging against the closed gold film. In Fig. 6.12(a)-(d) the spatial distribution of the absolute value of

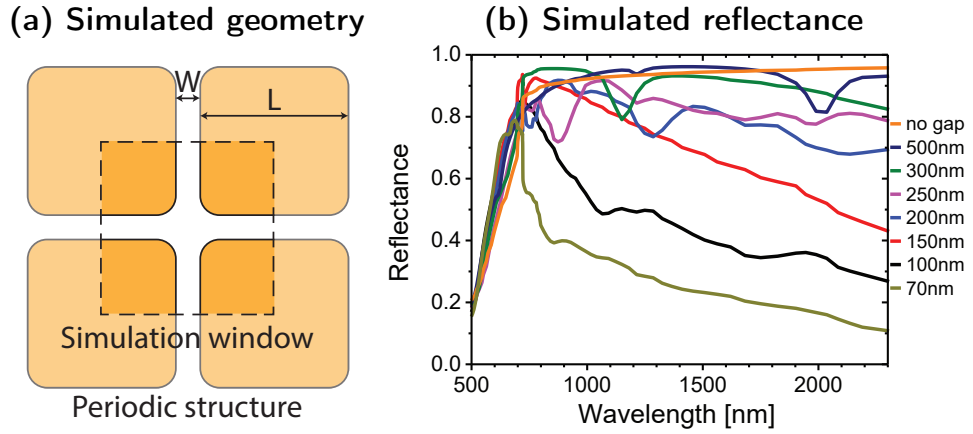

Figure 6.11.: (a) Scheme of the simulated geometry, indicating the simulated area. L is the size of the simulated squares and W is the gap in between them. (b) Simulated reflectance for different square sizes and a gap-less film as reference. A plane wave excitation and an AOI $\alpha = 30°$ is used.

the $\vec{E}$-field for $L = 100\,\mathrm{nm}$ squares with g $= 10\,\mathrm{nm}$ separation are depicted. The frequency of the exciting TE mode s-polarized plane wave is increased from $f = 170\,\mathrm{THz}$ to $f = 550\,\mathrm{THz}$. The propagation direction of the wave is parallel to the x-axis. In the gaps parallel to the wave propagation a high absolute value of the $\vec{E}$-field can be seen compared to the gaps parallel to the y-axis and on the squares. From all four graphs a cut line parallel to the x- and y-axis are extracted and plotted in Fig. 6.12(e). The maximum absolute value of the $\vec{E}$-field in the y-parallel gaps is lower than in the x-parallel gaps. Further the difference between maximum and minimum of the absolute value of the $\vec{E}$-field for the x-parallel gaps is increasing for lower frequencies.

Analyzing the reflectance minimum in Fig. 6.10 and Fig. 6.11(b), the spectral position, the absence of a shift and the width of the minimum exclude surface plasmons resonances as the root cause for the investigated behavior. The thorough studies of De Zuani *et al.* [37] showed that the gaps in the films prevent percolation and therefore the films behave as a dielectric layer. As a result the gold squares behave as an anti-reflection layer optimizing the absorption of the substrate in the near-infrared range. Additionally, the square size defines the absorption maximum and thereby the reflectance minimum, this allows to fabricate broadband anti-reflection coatings for near-infrared applications.

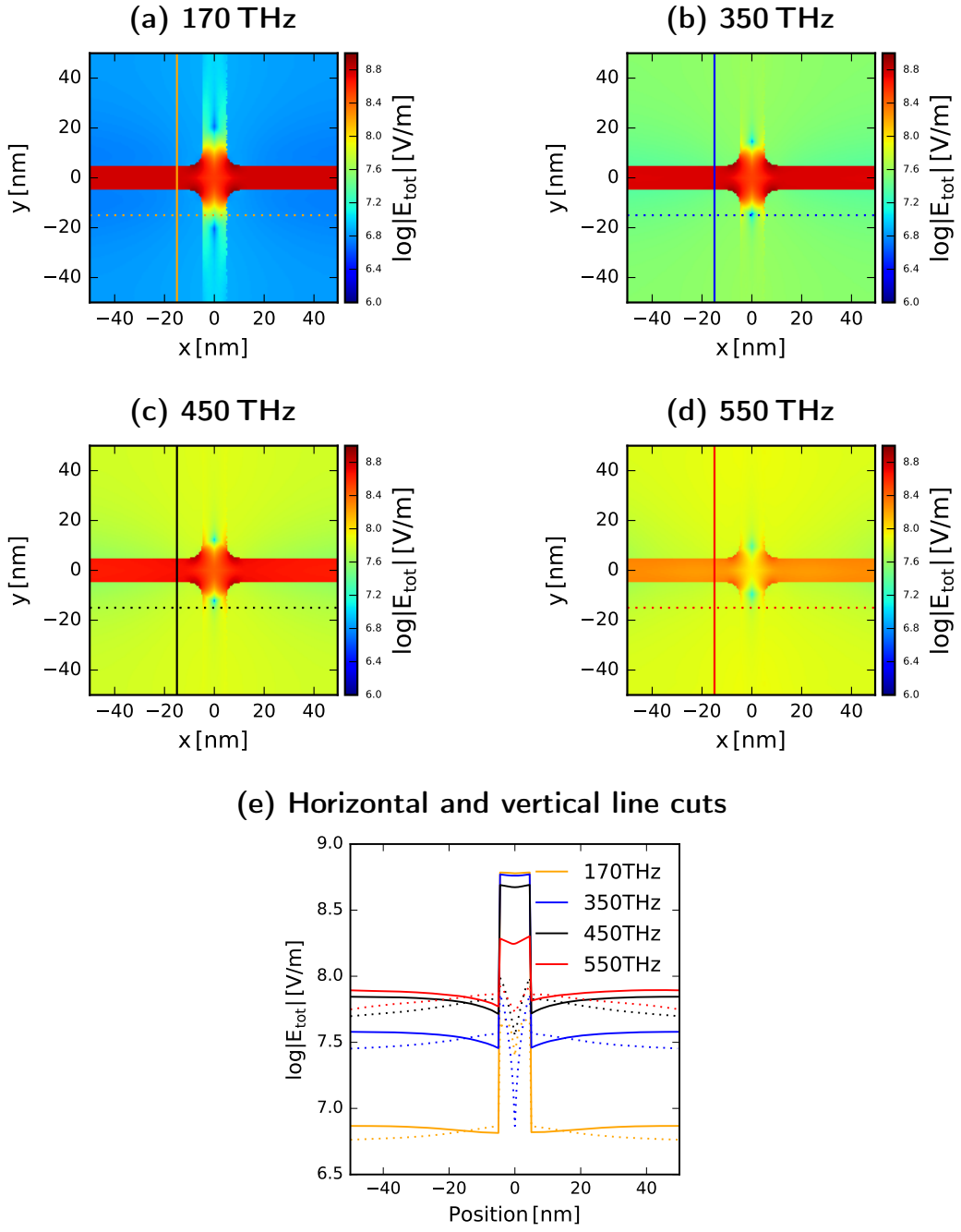

Figure 6.12.: Simulated spatial distribution of the absolute value of the $\vec{E}$-field for a quasi-film containing 100 nm squares separated by 10 nm excited by a TE s-polarized plane wave with frequencies (a) 170 THz, (b) 350 THz, (c) 450 THz and (d) 550 THz. The wave propagation direction is parallel to the x-axis and the AOI is $\alpha = 30°$. For each simulation a x-parallel (dashed) and a y-parallel (solid) line are extracted and plotted in (e).

6.3. Conclusion

The investigation of optical properties of a quasi-film using a not focused ellipsometer requires a large patterned area and therefore a stable process is needed. Small gaps in the film cause a high absorption in the near-infrared regime. The fabrication demands a process featuring high resolution in the sub-10 nm range on an insulating film. The presented HSQ PMMA bilayer process, developed and optimized by myself, makes it possible to fabricate these challenging samples. Moreover, this process opens up a new field of possibilities for further investigation of small features covering large areas on semiconductors and insulator covered semiconductors.

After investigating the influence of the filling factor by varying the square size it would be interesting to study the reflectance depending on increasing gap sizes preserving the square size. This type of samples are interesting from the fabrication point of view, too. The 100 nm squares with sub-10 nm gaps are already challenging to fabricate. Increasing the gap size leads to an increase in the pattern coverage and stronger process effects as well as more difficulties to produce proper structures are expected. Using PMMA instead is not an option, since a positive tone resist process would have to deal with a coverage up to almost 1 which makes the fabrication impossible. Closing the gap between coverages processable with HSQ and PMMA would be an interesting topic.

7. Summary and outlook

EBL is a well-studied and versatile lithography technique used in industry and research. In this thesis I investigated the potential and the capabilities of EBL for high-resolution sample fabrication down to the sub-10 nm regime. I developed an HSQ/PMMA bilayer lift-off process. The sacrificial PMMA layer allows the combination of the high resolution of HSQ with the organic solvent-based lift-off capabilities of PMMA. Therefore I could avoid the use of HF to dissolve HSQ, which allowed me to fabricate large-area pattern (several square millimeter) consisting of periodic metallic nano-structures on a Si substrate covered with SiO_2. The pattern consisted of squares with an edge length of 100 nm and the gap size could be reduced to below 10 nm. To change the filling factor the square size was increased and the samples can still be fabricated with the same process. The variety and needed resolution of these patterns require a high process control, especially the PMMA ashing step is critical to preserve the resolution of the patterned HSQ layer.

The patterned films I fabricated with the HSQ/PMMA bilayer process show an interesting optical response in the infrared regime, which was studied by De Zuani *et al.* [37]. Reflectivity measurements and FDTD simulations have confirmed a tunable broad reduced reflectivity in the infrared regime, which is close to zero depending on the size of the fabricated squares. The measured optical properties of the quasi-films could explained by a suppression of the percolation of the gold film leading to a dielectric behavior of the film causing the measured broad band low reflectivity. The resolution and large-area capabilities of the HSQ/PMMA bilayer process I developed was key to fabricate this new type of samples allowing to study optical properties at the percolation threshold.

After investigating the influence of the filling factor by increasing the square size and keeping the gap constant it would be interesting to study the influence of the gap size and the shape of the primitive element of the pattern. An increase of the gaps should decrease the coupling of the exposed squares. As a result it should be possible to measure a transition from a collective (quasi-film) to an averaged individual (well-spaced particle) behavior of the gold pattern.

For fabricating periodic, symmetric and large-area samples, the proximity effect (PE) is negligible, since only a constant background is generated in the region of interest. If the structures are randomly distributed with a constant

pattern density the long-range energy density contribution by backscattered electrons is still homogeneous. However, the short- and mid-range PE depends on the local disk distribution, which is irregular causing local deviations of the deposited energy density, which have to be corrected by proximity effect correction (PEC). I fabricated six samples with nanodisks on high-quality fused silica substrates using PEC. Three of them with randomly distributed disks of different pattern densities and three with the same variation in the structure density, however the disks are arranged on an upright square lattice. The transmission of the disk pattern on a fused silica substrate upon far-field illumination is studied by De Zuani *et al.* to investigate long-range interactions of the illuminated disks [18]. In order to have the disk size in all patterns as uniform as possible, PEC was used in combination with an undersize-overdose approach.

The third application discussed is the fabrication of line gratings containing holographic information on 30 nm thin silicon nitride membranes. Fabrication on thin substrates is challenging since the membranes are fragile, however the absence of a thick bulk material allows to neglect the PE. The fabricated gratings were designed to transfer orbital angular momentum to a transmitted electron beam. In order to achieve a high quality grating the EBL system was set up to use a good compromise of writing field size and beam current resulting in a 5 nm beam diameter. I was able to fabricate gratings with 40 nm line and gap width. In this project the sample handling was the main challenge since the membranes are fragile and the carrier chips are small. I developed a special chip holder to be able to load a carrier chip into the EBL system. Additionally, the holder improved the sample handling during all process steps after spin coating.

After fabrication several different gratings were loaded into different TEMs by Dr. Behnaz Rahmati from the StEM group at the MPI-FKF to use them as filters. The gratings should transfer OAM to the electron beam in order to measure EMCD with high spatial resolution. Unfortunately, no reproducible measurements were possible. From the fabrication point of view the thickness of the patterned film should be increased to achieve a better opacity. This might be possible by increasing the resist thickness and simultaneously improving the process contrast.

PEC is an interesting topic and is important if the substrate is a bulk material and the patterns are less symmetric and periodic. Additionally, the importance of the point spread function (PSF) and the extracted PSF_z as a starting point for a proper 2D PEC is interesting. To understand the interplay of PSF_z and PEC better I studied the dependency between them. By comparing two different Monte-Carlo simulation (MCS) packages, my collaborators and

me found a discrepancy in the simulated energy density distribution in the mid-range regime of the PSF_zs. This deviation could be explained by the method used to treat secondary electron (SE) generation and tracing. The different PSF_zs led to differences in the correction quality, which I confirmed with specifically designed control experiments. The MCS software PENELOPE has the option to influence the generation and tracking of SEs. By prohibiting the movement of SEs the PSF_z shows a reduced mid-range contribution (similar to the PSF_z calculated by SceletonX-v2011), and the exposed test pattern reveals a lower quality. If the SEs are simulated like the injected electrons, a large process window and a lower dose discrepancy for fabricating the test patterns are observed. This result confirms the importance of considering the SEs correctly. Further the company GenISys which develops the PEC software BEAMER started developing and distributing their own MCS software called TRACER based on my experimental results.

Often substantial deviations in the mid-range region can be observed, if PSF_zs generated by PENELOPE are compared with double-Gaussian approximations of those PSF_zs. Investigating the actual shape of the PSF_z of different material stacks in a double logarithmic representation the curve shows a linear slope in the mid-range region. This linear slope can be fitted using a power function. Therefore I was able to fit the whole PSF_z by using a sum of two Gaussian functions treating the short- and long-range part of the PSF_z as well as a power function accounting for the mid-range.

In order to verify simulated PSF_zs I developed an experimental method, the ring-test. The ring-test utilizes a disk pattern as a calibrated sensor superimposed by a ring. By the mean radius and the width of the ring the investigated part of the PSF_z is chosen. The resist height in the center of the sensor depends on the exposure contributed by the concentric ring. If the ring is exposed with the right dose considering the mean radius and width the resist height in the sensor center is constant. In this case the inverse normalized dose plotted versus the mean radius reproduces the PSF_z.

In a proof of concept I studied a PSF_z for 100 nm resist on a silicone substrate. The theoretical validation of my concept showed a good agreement of the original PSF_z and the simulation result of the ring-test. For the experimental validation of the ring-test I exposed an ensemble of sensors and concentric rings in a negative tone resist and measured the remaining resist thickness for multiple sensor-ring pairs using an AFM. I was able to measure the resist height of the sensor for ring radii down to 160 nm. After translating the measured thicknesses into the local exposure the PSF_z could be reconstructed down to 160 nm from the point of injection. The measured PSF_z was in good agreement with the original PSF_z calculated by PENELOPE.

With this new method to verify simulated PSF_z it is possible to study less well studied substrates like bulk insulators, complex heterostructures or pre-patterned substrates. Especially, bulk sapphire or thick insulator layers on silicon substrate would be interesting to study since I observed unexpected lithography results several times.

The PSF_zs can be used to determine the deposited energy density an average electron deposits in a certain resist slice by convolving the pattern and the PSF_z. Studying the progression of the deposited energy at pattern edges and within the patterned areas is a powerful method to understand how different PE correction algorithms work, why the designed pattern and the lithography results do not match or why the lithography failed. I used this method to understand the correlation between the dose to clear a large area (LADTC) and the dose to size (DTS). Theoretically the DTS has to be exactly twice the LADTC. However, process influences during measuring these doses cause a lower factor. Both doses are used as base dose to link the normalized energy density an average electron deposits in a certain resist slice to the normalized exposure within this resist slice. Which of the base doses has to be used depends on the PE correction algorithm.

With the help of the normalized exposure and the contrast curve of a specific resist process the resist thickness after development can be predicted. The E-BEAM simulation module of BEAMER provides the normalized exposure as result. The resist thickness prediction using this result is limited to the information the pattern, the PSF_z and the contrast curve account for. However, additional process influences not covered can contribute to the observed fabrication result and have to be considered by other means.

8. Zusammenfassung

Elektronen-Strahl-Lithografie (EBL) ist eine vielseitige Lithografie-Technik mit zahlreichen Anwendungsgebieten in der Industrie, Entwicklung und Forschung. In dieser Arbeit habe ich die Möglichkeiten und das Potenzial der EBL bezüglich der Herstellung hochaufgelöster Nanostrukturen untersucht. Dabei konnte ich eine Auflösung im Bereich von unter 10 nm erreichen. Hierfür entwickelte ich einen Doppellagenprozess unter Verwendung der elektronenstrahl-empfindlichen Lacke Polymethylmethacrylat (PMMA) und Wasserstoffsilsesquioxane (HSQ). Der PMMA Lack wird zu erst auf das Substrat aufgebracht und nach anschließendem Ausbacken wird HSQ aufgeschleudert.

Nach der Belichtung wird zunächst der HSQ Lack selektive entwickelt, wobei die belichteten Regionen bestehen bleiben. Anschließend wird die HSQ Struktur mittels Sauerstoffplasma in das PMMA übertragen, gefolgt vom Aufdampfen der gewünschten funktionellen Materialien. Die PMMA Schicht unter dem HSQ Lack dient als Opferschicht. Dadurch kann die hohe Auflösungsfähigkeit von HSQ mit der guten Löslichkeit von PMMA kombiniert werden. Während des Lift-Off Vorgangs wird die PMMA Schicht aufgelöst und das überflüssige Material ohne Kontakt zum Substrate wird abgehoben.

Dieser Lift-Off Prozess ermöglicht die Strukturierung von großen Flächen (mehrere Quadratmillimeter) mit der beschrieben hohen Auflösung. Weiterhin kann durch die Opferschicht die Verwendung von Flusssäure (HF) vermieden werden, welches gewöhnlich zum Auflösen von HSQ verwendet wird. Durch die Vermeidung von Kontakt der Probe mit Flusssäure ist es möglich höchaufgelöste metallische Nanostrukturen beispielsweise auf Glasproben herzustellen.

Mit Hilfe dieses PMMA/HSQ Doppellagenprozesses konnte ich großflächige, dicht gepackte, periodische Strukturen bestehend aus 100 nm große Goldquadrate herstellen, wobei der Abstand der Quadrate auf unter 10 nm reduziert werden konnte. Mit dem gleichen Prozess konnte ich ebenfalls Strukturen mit größeren Quadraten bei gleicher Separation herstellen. Somit konnten Proben mit unterschiedlichen Verhältnissen von Gold belegter Fläche zu nicht belegten Gräben hergestellt werden. Die unterschiedlichen Strukturgrößen und benötigte Auflösung stellen große Anforderungen an die Prozesskontrolle. Insbesondere die Kontrolle während der Plasmaerodierung des PMMAs ist kritisch um die hohe Auflösung der HSQ-Struktur erhalten zu können.

Die von mir hergestellten strukturierten Goldfilme zeigten einen unerwartetes und interessantes Verhalten bei Vermessung im Infrarotbereich. Um dieses Verhalten näher zu studieren hat Dr. Stefano De Zuani vom 1. Physikalischen Institut der Universität Stuttgart Reflektivitätsmessungen durchgeführt und sie zusammen mit seinen Kollegen ausgewertet, sowie mit Simulationen abgeglichen [37]. In ihren Untersuchungen konnten sie eine breitbandige verschiebbare Reduktion der Reflektivität bestätigen. Je nach Größe der Quadrate konnte ein Unterschied der spektralen Position sowie der minimalen Reflektivität beobachtet werden. Die minimale gemessene Reflektivität war nahezu null. Das gemessene optische Verhalten der strukturierten Quasi-Filme konnte auf die Unterdrückung der Perkolation der Goldfilme zurückgeführt werden. Dadurch kann das dielektrische Verhalten der Proben sowie die breitbandige reduzierte Reflektivität erklärt werden.

Das Auflösungsvermögen und die Nutzbarkeit zur Strukturierung großer Flächen des von mir entwickelten HSQ/PMMA Doppellagenprozesses haben diese neuartigen Proben sowie die Messungen und Beobachtungen möglich gemacht. Nachdem bereits der Einfluss des Verhältnisses von Quadratgröße zu Grabenbreite untersucht wurde, könnten weitere Experimente mit anderen Grundformen oder der Variation der Grabenbreite durchgeführt werden. Eine Verbreiterung der Gräben sollte die Kopplung der einzelnen Nanostrukturen reduzieren. Damit verbunden sollten die Messungen einen Übergang von einem kollektivem (Quasi-Film) zu einem gemittelten Verhalten (großzügig separierte Nanostrukturen) zeigen.

Ein weiterer Schwerpunkt meiner Arbeit war die Untersuchung des Proximity Effekts (PE). Der PE beschreibt den ungewollten Energieeintrag im Lack in unbelichteten Regionen, verursacht durch die Elektronenstreuung. Für die Herstellung periodischer, symmetrischer großflächiger Proben ist der Proximity Effekt (PE) vernachlässigbar. Die zurückgestreuten Elektronen Erzeugen einen flächigen Hintergrund welcher in den untersuchten Bereichen konstant ist und kann somit durch Prozesskalibrierung korrigiert werden. Wenn die Strukturen, bei konstanter Strukturdichte, zufällig verteilt sind, ist der langreichweitige deponierte Energiedichtebeitrag immer noch homogen, der kurz- und mittelreichweitige PE hingegen hängt von der lokalen Strukturverteilung ab. Durch die ungleichmäßige Anordnung werden Variationen in der deponierten Energiedichte verursacht. Diese Inhomogenitäten können mit Hilfe von Proximity Effekt Korrektur (PEC) behoben werden.

Bei der PEC wird versucht mit Hilfe von Dosisanpassung das alle Belichteten Flächen eine deponierte Energiedichte größer als ein gewisser Schwellwert erhalten. Der gewählte Schwellwert spiegelt ein gewisses Verhalten des belichteten Lackes wider. So wird zum Beispiel ein positiver Lack während des Entwi-

ckelns in den belichteten Regionen komplett aufgelöst wenn der Schwellwert überschritten wurde. Wenn die PEC korrekt ausgeführt wurde sollte somit nach der Belichtung einer PE korrigierten Struktur das definierte Design exakt reproduziert werden.

Unter Zuhilfenahme von PEC habe ich sechs großflächige Proben bestehend aus 190 nm großen Nanoscheiben auf Quarzglas hergestellt. Drei bestanden aus zufällig verteilten Scheiben mit unterschiedlicher Strukturdichte. Drei weitere Proben hatten die gleiche Strukturdichte jedoch waren sie auf einem periodischen Quadratgitter angeordnet. Durch die Verwendung von qualitative hochwertigem Quarzglas als Substrat wurde sowohl die Messungen der Reflektivität als auch der Transmissivität ermöglicht. Im Rahmen der Vermessung des Transmissionsverhaltens der Proben im Fernfeld wurden langreichweitige Wechselbeziehungen der Scheiben von De Zuani *et al.* untersucht [18].

Um möglichst identische Nanoscheiben in Form und Größe sowie möglichst gleichmäßige Proben zu erhalten, habe ich PEC mit dem „Undersize-Overdose“ Verfahren kombiniert. Dabei werden die Strukturen bewusst kleiner definiert und anschließend die Belichtungsdosis entsprechend nach oben korrigiert um die gewünschte Strukturgröße zu erhalten. Mit Hilfe der beschriebenen Herangehensweise kann das Prozessfenster gespreizt werden und zuverlässigere Herstellungsergebnisse erzielt werden.

Die dritte Sorte Proben, welche ich hergestellt habe und in dieser Arbeit beschrieben habe, sind Liniengitter, die holographische Informationen enthalten. Diese Gitter wurden auf 30 nm dünnen Siliziumnitridmembranen hergestellt um sie später als Filter in einem Transmissionselektronenmikroskop (TEM) zu installieren. Die Herstellung von Nanostrukturen auf sehr dünnen Schichten ist anspruchsvoll, da die verwendeten Membranen empfindlich sind. Jedoch kann für diese dünnen Substrate, auf Grund der geringen Rückstreuwahrscheinlichkeit der Elektronen beim Belichten, der PE vernachlässigt werden.

Die hergestellten Gitter wurden mittels computergestützter Holographie designt und sollen bei kohärenter Beleuchtung den transmittierten Elektronen ein Orbital Winkelmoment übertragen. Ziel ist es einen Elektronenstrahl zu generieren der magneto-dichromatische Messungen (EMCD) mit Hilfe von Elektronenenergieverlustspektroskopie (EELS) ermöglicht.

Um möglichst gut definierte Gitter herstellen zu können, wurde beim Kalibrieren des verwendete EBL System ein Kompromiss zwischen Schreibfeldgröße und Strahlstrom geschlossen. Dieser Kompromiss beschränkte den kleinst möglichen Strahldurchmesser auf 5 nm. Unter den genannten Voraussetzungen war es mir möglich Gitter mit einer Linienbreite sowie einem Linienabstand von jeweils 40 nm herzustellen. In diesem Projekt war die Probenhandhabung die Hauptherausforderung da die Membranen zerbrechlich und die Trägersubstrate

klein waren. Zu diesem Zweck habe ich einen speziellen Probenhalter entwickelt um die Substrate in das EBL System laden zu können. Der gleiche Probenhalter wurde während des gesamten Herstellungsprozesses verwendet und hat die Handhabung der Proben deutlich vereinfacht.

Nach der Fertigstellung wurden verschiedene Gitter in unterschiedliche TEMs geladen und als Filter verwendet. Dr. Behnaz Rahmati von der StEM Gruppe am Max-Planck-Institut für Festkörperforschung (MPI-FKF) hat die Arbeiten an und mit den TEMs durchgeführt. Sie hat EMCD Messung an dünnen Eisenfilmen auf Magnesiumoxid durchgeführt. Dabei zeigten vereinzelte Messungen das erwartete dichromatische Signal für die L_2 und L_3 Übergänge im Eisen, leider waren die Messungen jedoch nicht reproduzierbar und das Projekt wurde eingestellt.

Von der Herstellungsseite könnten die Filter weiter verbessert werden, in dem zum Beispiel die Dicke des aufgedampften Goldfilms vergrößert würde. Damit könnte eine verbesserte Undurchlässigkeit in den bedeckten Regionen erreicht und somit die Effizienz der Interferenz erhöht werden. Wenn dickere Metallfilme verwendet werden sollen, muss die Lackdicke vergrößert und gleichzeitig der Prozesskontrast verbessert werden.

Die Proximity Effekt Korrektur ist ein interessanter Prozess und ist wichtig wenn auf massiven Proben, weniger symmetrische oder nicht-periodische Strukturen belichtet werden. Um die PEC systematisch durchführen zu können wird eine sogenannte Punktspreizfunktion (PSF) benötigt. Die PSF beschreibt die deponierte Energiedichteverteilung in der belichteten Probe, dabei ist vor allem die Verteilung in der Lackschicht (PSF_z) von Interesse um das Strukturierungsergebnis zu verbessern.

Um das Zusammenspiel der PEC und der im Lack extrahierten PSF_z zu verstehen habe ich Tests entwickelt um die PEC Qualität zu untersuchen. Beim Vergleich verschiedener PSF_z, welche mit Hilfe zwei unterschiedlicher Monte-Carlo Simulationsprogramme (MCS) erzeugt wurden, haben meine Kollegen und ich Abweichungen in der Form der PSF_z entdeckt. Speziell der mittelreichweitige Bereich der PSF_z war verschieden für die verwendeten Simulationspakete PENELOPE und SceletonX-v2011. Uns war es möglich durch Simulationen die Abweichungen auf die Bearbeitungsweise der erzeugten Sekundärelektronen (SE) zurückzuführen. PSF_z ohne detaillierte Verfolgung der SEs haben in den Testbelichtungen Strukturen geringerer Qualität hervorgebracht. Wurde die SE Verfolgung hingegen berücksichtigt, konnte mit den entsprechenden PSF_z eine geringere Basisdosis Abweichung und ein größeres Prozessfenster bei der Herstellung der Teststrukturen erreicht werden. Somit kann konstatiert werden, dass die detaillierte Betrachtung der Sekundärelektronen bei der Simulation der PSFs ein wichtiger Bestandteil für die Verbesserung des PEC Resultats ist. Für

sämtliche Korrekturen wurde die selbe PEC Software (BEAMER von GenISys) verwendet. Basierend auf diesen Ergebnissen begann GenISys die Entwicklung und Vermarktung einer eigenen MCS Software genannt TRACER.

Werden mit PENELOPE simuliert PSF_z durch Doppel-Gaußverteilungen genähert kann oft eine bedeutende Abweichung im mittelreichweitigen Bereich beobachtet werden. In doppelt logarithmischer Darstellung zeigt die PSF_z einen linearen Verlauf im Bereich mittlerer Reichweite. Dieser Kurvenverlauf weist auf eine Potenzfunktion hin. Damit ist es möglich die gesamte PSF_z mit Hilfe der Summe zweier Gaußverteilungen und einer Potenzfunktion abzubilden. Hierbei reproduzieren die Gaußverteilungen die kurzreichweitigen und langreichweitigen Teile der PSF_z und die Potenzfunktion beschreibt die mittelreichweitigen Einflüsse der PSF_z.

Weiterhin habe ich einen experimentelle Methode entwickelt um simulierte PSF_z zu validieren, den sogenannten Ring-Test. Der Ring-Test nutzt eine Scheibe mit $d = 1\,\mu\mathrm{m}$ als kalibrierten Sensor welcher mit einem konzentrischen Ring überlagert wird. Der mittlere Radius und die Ringbreite definieren den untersuchten Bereich der PSF_z. Für den Ring-Test wird ein Lack verwendet der durch Elektronenbestrahlung vernetzt und somit in Abhängigkeit von der deponierten Energiedichte zunehmend schwieriger im Entwicklerbad gelöst werden kann. Die Lackdicke in der Mitte des Sensors nach dem entwickeln hängt damit zum einen von verwendeten Dosis zur Belichtung des Sonsors als auch vom Belichtungsbeitrag der in den Ring injizierten Elektronen ab. Wird der Ring mit der richtigen Dosis belichtet, so wird die gemessene Lackdicke in der Mitte des Sensors immer gleich sein. Die Dosis wird in Abhängigkeit von Radius und Breite des Rings unter Verwendung der PSF_z berechnet. Trägt man die reziproke normierte Dosis gegen den Ringradius auf so wird die Ausgangs-PSF_z reproduziert.

Für die Validierung des Ring-Tests habe ich die PSF_z für 100 nm Lack auf einem Siliziumsubstrat untersucht. Die theoretische Validierung habe ich mit Hilfe des E-BEAM Simulationsmoduls von BEAMER erbracht. Dabei konnte ich eine gute Vereinbarkeit der Simulationen und der Ausgangs-PSF_z zeigen. Für den experimentellen Nachweis habe ich ein Ensemble von Sensoren und Ringen belichtet und die nach dem Entwickeln verbleibende Lackdicke mit einem Rasterkraftmikroskop (AFM) gemessen. Nach dem konvertieren der gemessenen Lackdicken mit Hilfe der Kalibrierkurve der Sensoren war es möglich die mit PENELOPE simulierte PSF_z bis zu 160 nm vom Elektroneninjektionspunkt im Rahmen der Messfehler zu rekonstruieren.

Mit diesem neuen Verfahren ist es möglich die PSF_z für weniger gründlich untersuchte Substratmaterialien zu verifizieren. Massive Nichtleiter, komplexe Heterostrukturen oder vorstrukturierte Proben werden immer häufiger zur

Herstellung von Nanostrukturen mittels EBL genutzt. Insbesondere Saphirwafer und dicke isolierende Schichten auf Siliziumsubstraten sind interessant zu untersuchen, da ich wiederholt unerwartete Lithografieergebnisse auf diesen Materialien beobachtet habe.

Die PSF_z kann verwendet werden um die deponierte Energiedichteverteilung zu bestimmen, welche ein durchschnittliches Elektron in einem definierten Muster erzeugen kann. Hierfür wird die PSF_z mit dem Muster gefaltet. Der Verlauf der deponierten Energiedichte an den Kanten der belichteten Struktur ist eine gute Möglichkeit Aufschluss über unterschiedliche PEC Algorithmen zu erhalten und zu verstehen warum die designte Struktur mit der hergestellten nicht übereinstimmen oder warum der Lithografieschritt fehlschlug. Ich habe diese Methode genutzt um die Beziehung der Dosis zur vollständigen Entfernung des Lackes in der Mitte einer großen Fläche (LADTC) und der Dosis zum erreichen der designten Stukturgröße (DTS) zu untersuchen. Dabei habe ich festgestellt, dass die DTS exakt doppelt so groß wie die LADTC sein sollte. In der Wirklichkeit ist der Faktor jedoch kleiner, was auf Prozesseinflüsse zurückgeführt werden kann. Beide Dosiswerte werden als Basisdosis für verschieden PEC Algorithmen verwendet. Außerdem kann die Basisdosis verwendet werden um die „Belichtung“ zu definieren.

Die „Belichtung“ ist das Produkt aus der Basisdosis und der deponierten Energiedichte. Mit Hilfe der „Belichtung“ und der Kontrastkurve des verwendeten Lackes kann die erwartete Lackdicke nach dem Entwickeln vorhergesagt werden. Die deponierte Energiedichteverteilung kann vom E-BEAM Modul von BEAMER berechnet werden. Die Kontrastkurve beschreibt die Lackdicke einer großen belichteten Fläche nach dem Entwickeln in Abhängigkeit von der Dosis. Die Vorhersage ist jedoch beschränkt durch die zur Verfügung gestellten Informationen. Im Detail sind das die designte Struktur die PSF_z und die Kontrastkurve. Alle Effekt, die in diesen Bestandteilen nicht abgebildet sind, können auf diese Weise nicht berücksichtigt werden und müssen anderweitig korrigiert werden.

A. Considerations concerning the calculated deposited energy distribution

A.1. Calculating the total deposited energy

The total energy E_{tot} deposited in an exposed sample can be defined as:

$$E_{\text{tot}} = N\,E_1. \tag{A.1}$$

N is the number of injected electrons in the exposed area and E_1 is the deposited energy in the sample per injected average electron. Using the dose D and the exposed area A_{exp}, N can be calculated as follows:

$$\begin{aligned} N &= D\,A_{\text{exp}}\left(6.242\times10^{18}\,\frac{1}{\text{C}}\right) \\ &= n\,A_{\text{exp}}. \end{aligned} \tag{A.2}$$

$6.242\times10^{18}\,\text{C}^{-1}$ is the number of electrons per Coulomb and n is the electron density injected into the exposed area. n corresponds to D. Without loss of generality the pattern $p(x,y)$ can be defined as a sum of rectangles described by Heaviside step functions (Θ):

$$p(x,y) = \sum_i \left(\Theta\left(x+x_i\right)\,\Theta\left(-x+x_i+w_i\right)\,\Theta\left(y+y_i\right)\,\Theta\left(-y+y_i+h_i\right)\right). \tag{A.3}$$

Using x_i, w_i, y_i and h_i rectangles can be defined to approximate any arbitrary pattern. Inserting Eqn. (A.2) into Eqn. (A.1) results in:

$$E_{\text{tot}} = n\,A_{\text{exp}}\,E_1, \tag{A.4}$$

E_1 can be calculated by:

$$E_1 = \int_V \varepsilon_1(x,z,y)\,\mathrm{d}V. \tag{A.5}$$

V is the volume of the resist and $\varepsilon_1(x,y,z)$ is the energy density distribution a single average injected electron could deposit in the sample at an observation point $P(x,y,z)$. $\varepsilon_1(x,y,z)$ can be calculated by a convolution of the product $\big(p(x,y)\,\mathrm{DF}(x,y)\big)$ with the $\mathrm{PSF}(r,z)$. The convolution it self is a weighted averaging of the dimensionless pattern with the PSF, therefore the dimensions of the PSF are preserved.

$$\begin{aligned}\varepsilon_1(x,y,z) &= \big(p(x,y)\,\mathrm{DF}(x,y)\big) * \mathrm{PSF}(r,z)\\ &= \int_\tau\int_\upsilon \big(p(\tau,\upsilon)\,\mathrm{DF}(\tau,\upsilon)\big)\,\mathrm{PSF}\left(\sqrt{(x-\tau)^2+(y-\upsilon)^2},z\right)\mathrm{d}\upsilon\,\mathrm{d}\tau\end{aligned} \tag{A.6}$$

$\mathrm{DF}(x,y)$ is the dose factor map to account for the PEC.

Replacing E_1 in Eqn. (A.4) by the expression from Eqn. (A.5), leads to:

$$E_{\mathrm{tot}} = n\,A_{\mathrm{exp}}\int_V \varepsilon_1(x,y,z)\,\mathrm{d}V \tag{A.7}$$

Introducing Eqn. (A.6) in Eqn. (A.7) results in:

$$\begin{aligned}E_{\mathrm{tot}} = n\,A_{\mathrm{exp}}\int_V\int_\tau\int_\upsilon &\big(p(\tau,\upsilon)\,\mathrm{DF}(\tau,\upsilon)\big)\\ &\cdot\,\mathrm{PSF}\left(\sqrt{(x-\tau)^2+(y-\upsilon)^2},z\right)\mathrm{d}\upsilon\,\mathrm{d}\tau\,\mathrm{d}V,\end{aligned} \tag{A.8}$$

describing the total energy deposited by all injected electrons in the complete sample also supporting PEC by facilitating a position dependent dose factor map $\mathrm{DF}(x,y)$.

The PSF(r,z) is gradually changing in the z-direction over the whole material stack. Due to technical reasons, PENELOPE is binning the deposited energy into finite bins [26] and hence averaging the PSF over the bin height t_{bin}. Choosing bins with $t_{\mathrm{bin}} = 20\,\mathrm{nm}$ has proven to be a good compromise between simulation time and PSF quality. The PSF is extracted from a slice at the height z, usually in the middle of the resist height, with a slice thickness t_{bin}. Therefore the approximation,

$$\int_{z-\frac{t_{\mathrm{bin}}}{2}}^{z+\frac{t_{\mathrm{bin}}}{2}} \mathrm{PSF}(r,z)\mathrm{d}z = t_{\mathrm{bin}}\,\mathrm{PSF}_z(r), \tag{A.9}$$

can be done for a PSF simulated by PENELOPE. The total deposited energy in a resist slice $E_{\mathrm{tot},z}$ can be calculated by applying Eqn. (A.9) to Eqn. (A.8).

$$\begin{aligned}E_{\mathrm{tot},z} = n\,A_{\mathrm{exp}}\,t_{\mathrm{bin}}\int_x\int_y\int_\tau\int_\upsilon &\big(p(\tau,\upsilon)\,\mathrm{DF}(\tau,\upsilon)\big)\\ &\cdot\,\mathrm{PSF}_z\left(\sqrt{(x-\tau)^2+(y-\upsilon)^2}\right)\mathrm{d}\upsilon\,\mathrm{d}\tau\,\mathrm{d}x\,\mathrm{d}y.\end{aligned} \tag{A.10}$$

The same calculation can be repeated for all available resist slices PSF_z of the PSF. Those might be necessary if the resist profile is of concern for example in grayscale lithography. If the z-profile of the resist is negligible, like in most cases of 2D lithography, it is usually enough to investigate a single slice in the middle of the resist.

Eqn. (A.8) describes the total energy deposited by all injected electrons in the complete sample also supporting PEC by facilitating a position dependent dose factor map $\mathrm{DF}(x, y)$. If the PSFs is simulated using finite bins as PENELOPE does it requires less effort to use Eqn. (A.10). Further in EBL the resist is the part of the sample which has to be modified by the injected electrons for a successful lithography. Thus it is enough to study the $E_{tot,z}$ for the resist slices. Depending on the application it might be needed to investigate all resist slices, however often it is enough to study the middle slice in the resist. For example, a single average electron 100 keV injected into a 100 nm thick PMMA layer on a Si substrate deposits approximately 12 eV in a 20 nm thick resist slice around the middle of the resist height.

While studying LADTC or DTS, it is interesting to investigate the spatially resolved normalized deposited energy density distribution within a resist slice for an average injected electron $\varepsilon_{1,z,\mathrm{norm}}$, which I am going to derive in the next section.

A.2. Simulated energy profile

For the simulation module provided by BEAMER a specific PSF_z and the $p(x, y)$ have to be provided. As simulation result the normalized exposure $\mathcal{E}_{z,\mathrm{norm}}$ is calculated.

$$\mathcal{E}_{z,\mathrm{norm}}(x, y) = D\, \varepsilon_{1,z,\mathrm{norm}}(x, y) \tag{A.11}$$

$\varepsilon_{1,z,\mathrm{norm}}(x, y)$ is the normalized deposited energy distribution in a certain resist slice for an average injected electron. First by applying Eqn. (A.9) to Eqn. (A.6) the investigated volume can be limited to the resist slice the PSF_z was extracted $(\varepsilon_{1,z}(x, y))$.

$$\begin{aligned}\varepsilon_{1,z}(x,y) &= \int_{z-\frac{t_{\text{bin}}}{2}}^{z+\frac{t_{\text{bin}}}{2}} \int_\tau \int_\upsilon \big(p(\tau,\upsilon)\,\mathrm{DF}(\tau,\upsilon)\big) \\ &\qquad \cdot \mathrm{PSF}\left(\sqrt{(x-\tau)^2+(y-\upsilon)^2}, z\right) \mathrm{d}\upsilon\,\mathrm{d}\tau\,\mathrm{d}z \\ &= t_{\text{bin}} \int_\tau \int_\upsilon \big(p(\tau,\upsilon)\,\mathrm{DF}(\tau,\upsilon)\big) \\ &\qquad \cdot \mathrm{PSF}_z\left(\sqrt{(x-\tau)^2+(y-\upsilon)^2}\right) \mathrm{d}\upsilon\,\mathrm{d}\tau \end{aligned} \tag{A.12}$$

The second step is to normalize the PSF_z by the amount of energy an average injected electron deposits in the investigated resist slice $E_{1,z}$:

$$\begin{aligned}\mathrm{PSF}_{z,\text{norm}}(x,y) &= \frac{t_{\text{bin}}\,\mathrm{PSF}_z(x,y)}{E_{1,z}} \\ \text{with: } E_{1,z} &= 2\pi\, t_{\text{bin}} \int_r \mathrm{PSF}_z(r)\, r\,\mathrm{d}r \end{aligned} \tag{A.13}$$

$$\begin{aligned}\mathrm{PSF}_{z,\text{norm}}(x,y) &= \frac{t_{\text{bin}}\,\mathrm{PSF}_z(x,y)}{2\pi\, t_{\text{bin}} \int_r \mathrm{PSF}_z(r)\, r\,\mathrm{d}r} \\ &= \frac{\mathrm{PSF}_z(x,y)}{2\pi \int_r \mathrm{PSF}_z(r)\, r\,\mathrm{d}r}. \end{aligned} \tag{A.14}$$

By replacing $\mathrm{PSF}_z(x,y)$ with $\mathrm{PSF}_{z,\text{norm}}(x,y)$ in Eqn. (A.12) $\varepsilon_{1,z}(x,y)$ becomes $\varepsilon_{1,z,\text{norm}}(x,y)$:

$$\begin{aligned}\varepsilon_{1,z,\text{norm}}(x,y) &= \int_\tau \int_\upsilon \big(p(\tau,\upsilon)\,\mathrm{DF}(\tau,\upsilon)\big) \\ &\qquad \cdot \mathrm{PSF}_{z,\text{norm}}\left(\sqrt{(x-\tau)^2+(y-\upsilon)^2}\right) \mathrm{d}\upsilon\,\mathrm{d}\tau \\ &= \int_\tau \int_\upsilon \big(p(\tau,\upsilon)\,\mathrm{DF}(\tau,\upsilon)\big) \\ &\qquad \cdot \frac{\mathrm{PSF}_z\left(\sqrt{(x-\tau)^2+(y-\upsilon)^2}\right)}{2\pi \int_r \mathrm{PSF}_z(r)\, r\,\mathrm{d}r} \mathrm{d}\upsilon\,\mathrm{d}\tau \end{aligned} \tag{A.15}$$

This normalization is chosen to provide a $\varepsilon_{1,z,\text{norm}} = 1$ in the center of an infinitely large pattern.

Finally, by inserting Eqn. (A.15) in Eqn. (A.11) the normalized exposure

$\mathcal{E}_{z,\mathrm{norm}}$ would be:

$$\mathcal{E}_{z,\mathrm{norm}}(x,y) = D \int_{\tau}\int_{\upsilon} \big(p(\tau,\upsilon)\,\mathrm{DF}(\tau,\upsilon)\big) \cdot \frac{\mathrm{PSF}_z\left(\sqrt{(x-\tau)^2+(y-\upsilon)^2}\right)}{2\pi\int_r \mathrm{PSF}_z(r)\,r\,\mathrm{d}r}\,\mathrm{d}\upsilon\,\mathrm{d}\tau \tag{A.16}$$

In the center of a sufficiently large fully covered not PE corrected pattern ($\mathrm{DF}(x,y)=1$) $\varepsilon_{1,z,\mathrm{norm}}=1$ and therefore $\mathcal{E}_{z,\mathrm{norm}}(x,y)=D$. Hence it is possible by using the contrast curve to calculate the expected resist thickness after development.

If the dose $D=1$ is chosen Eqn. (A.16) simplifies to Eqn. (A.15) and the simulation results would be between 0 and 1. In many cases I used this normalization of the dose for my simulations to improve the understandability of the results by decoupling it from a real process. Especially for understanding of the threshold model and the relation between DTS and LADTC simulating normalized energy distribution $\varepsilon_{1,z,\mathrm{norm}}(x,y)$ instead of the normalized exposure $\mathcal{E}_{z,\mathrm{norm}}(x,y)$ is advantageous.

Bibliography

[1] G. Brewer and J. Ballantyne, *Electron-beam technology in microelectronic fabrication*. Academic Press, 1980.

[2] P. Rai-Choudhury, ed., *Handbook of Microlithography, Micromachining, and Microfabrication*, vol. 1. Microlithography of *Handbook of Microlithography, Micromachining, and Microfabrication V.2: Micromachining and Microfabricatio*. SPIE Optical Engineering Press, 1997.

[3] M. Stepanova and S. Dew, eds., *Nanofabrication: Techniques and Principles*. SpringerLink: Bücher, Springer, 2011.

[4] C. S. Wu, Y. Makiuchi, and C. Chen, *Lithography*, ch. High-energy Electron Beam Lithography for Nanoscale Fabrication. InTech, Feb 2010.

[5] S. Y. Chou, P. R. Krauss, and P. J. Renstrom, "Nanoimprint lithography," *Journal of Vacuum Science & Technology B*, vol. 14, no. 6, pp. 4129–4133, 1996.

[6] S. Y. Chou, P. R. Krauss, and P. J. Renstrom, "Imprint Lithography with 25-Nanometer Resolution," *Science*, vol. 272, no. 5258, pp. 85–87, 1996.

[7] H. Lim, K. bong Choi, G. Kim, S. Lee, H. Park, J. Ryu, S. Jung, and J. Lee, "Roll-to-roll nanoimprint lithography for patterning on a large-area substrate roll," *Microelectronic Engineering*, vol. 123, no. 0, pp. 18 – 22, 2014.

[8] N. Kooy, K. Mohamed, L. T. Pin, and O. S. Guan, "A review of roll-to-roll nanoimprint lithography," *Nanoscale Res Lett*, vol. 9, pp. 320–320, Jun 2014.

[9] S. Y. Chou, P. R. Krauss, and P. J. Renstrom, "Imprint of sub-25 nm vias and trenches in polymers," *Applied Physics Letters*, vol. 67, no. 21, pp. 3114–3116, 1995.

[10] S. Gilles, M. Meier, M. Prömpers, A. van der Hart, C. Kügeler, A. Offenhäusser, and D. Mayer, "UV nanoimprint lithography with rigid polymer molds," *Microelectronic Engineering*, vol. 86, no. 4-6, pp. 661 – 664, 2009.

[11] L. Hanson, Z. C. Lin, C. Xie, Y. Cui, and B. Cui, "Characterization of the Cell-Nanopillar Interface by Transmission Electron Microscopy," *Nano Letters*, vol. 12, no. 11, pp. 5815–5820, 2012.

[12] J. T. Robinson, M. Jorgolli, A. K. Shalek, M.-H. Yoon, R. S. Gertner, and H. Park, "Vertical nanowire electrode arrays as a scalable platform for intracellular interfacing to neuronal circuits," *Nat Nano*, vol. 7, pp. 180–184, Mar 2012.

[13] F. Persson, J. Fritzsche, K. U. Mir, M. Modesti, F. Westerlund, and J. O. Tegenfeldt, "Lipid-Based Passivation in Nanofluidics," *Nano Letters*, vol. 12, no. 5, pp. 2260–2265, 2012.

[14] K. Frykholm, M. Alizadehheidari, J. Fritzsche, J. Wigenius, M. Modesti, F. Persson, and F. Westerlund, "Probing Physical Properties of a DNA-Protein Complex Using Nanofluidic Channels," *Small*, vol. 10, no. 5, pp. 884–887, 2014.

[15] J. Svensson, N. Lindahl, H. Yun, M. Seo, D. Midtvedt, Y. Tarakanov, N. Lindvall, O. Nerushev, J. Kinaret, S. Lee, and E. E. B. Campbell, "Carbon Nanotube Field Effect Transistors with Suspended Graphene Gates," *Nano Letters*, vol. 11, no. 9, pp. 3569–3575, 2011.

[16] L. Ocola, D. Tennant, and P. Ye, "Bilayer process for T-gates and Gamma-gates using 100-kV e-beam lithography," *Microelectronic Engineering*, vol. 67-68, no. Supplement C, pp. 104 – 108, 2003.

[17] R. Sabo, I. Gurman, A. Rosenblatt, F. Lafont, D. Banitt, J. Park, M. Heiblum, Y. Gefen, V. Umansky, and D. Mahalu, "Edge reconstruction in fractional quantum Hall states," *Nat Phys*, vol. 13, pp. 491–496, May 2017.

[18] S. De Zuani, M. Rommel, R. Vogelgesang, J. Weis, B. Gompf, M. Dressel, and A. Berrier, "Large-Area Two-Dimensional Plasmonic Meta-Glasses and Meta-Crystals: a Comparative Study," *Plasmonics*, vol. 12, pp. 1381–1390, Oct 2017.

[19] R. Verre, Z. J. Yang, T. Shegai, and M. Käll, "Optical Magnetism and Plasmonic Fano Resonances in Metal-Insulator-Metal Oligomers," *Nano Letters*, vol. 15, no. 3, pp. 1952–1958, 2015.

[20] C. T. Leondes, ed., *MEMS/NEMS*. Springer US, 2006.

[21] M. G. el Hak, ed., *MEMS: Design and Fabrication*. Boca Raton, FL, USA: CRC Press, 2 ed., 2006.

[22] S. A. Rishton, H. Schmid, D. P. Kern, H. E. Luhn, T. H. P. Chang, G. A. Sai-Halasz, M. R. Wordeman, E. Ganin, and M. Polcari, "Lithography for ultrashort channel silicon field effect transistor circuits," *Journal of Vacuum Science & Technology B: Microelectronics Processing and Phenomena*, vol. 6, no. 1, pp. 140–145, 1988.

[23] C. Corporation, "CABL-UH(130kV)series," 2017.

[24] M. Hatzakis, "Electron Resists for Microcircuit and Mask Production," *Journal of The Electrochemical Society*, vol. 116, no. 7, pp. 1033–1037, 1969.

[25] D. L. Olynick, B. Cord, A. Schipotinin, D. F. Ogletree, and P. J. Schuck, "Electron-beam exposure mechanisms in hydrogen silsesquioxane investigated by vibrational spectroscopy and in situ electron-beam-induced desorption," *Journal of Vacuum Science & Technology B, Nanotechnology and Microelectronics: Materials, Processing, Measurement, and Phenomena*, vol. 28, no. 3, pp. 581–587, 2010.

[26] J. F.-V. F. Salvat and J. Sempau, *PENELOPE-2008: A Code System for Monte Carlo Simulation of Electron and Photon Transport*. OECD Nuclear Energy Agency, Issy-les-Moulineaux, France, 2008.

[27] D. A. Czaplewski, M. V. Holt, and L. E. Ocola, "The range and intensity of backscattered electrons for use in the creation of high fidelity electron beam lithography patterns," *Nanotechnology*, vol. 24, no. 30, p. 305302, 2013.

[28] Q. Dai, S.-Y. Lee, S. Lee, B.-G. Kim, and H.-K. Cho, "Estimation of resist profile for line/space patterns using layer-based exposure modeling in electron-beam lithography," *Microelectronic Engineering*, vol. 88, no. 6, pp. 902 – 908, 2011.

[29] Z. Cui, *Micro-nanofabrication: technologies and applications*. Berlin: Springer, 2006.

[30] P. C. Ng, K.-Y. Tsai, and L. S. Melvin, "Study of etching bias modeling and correction strategies for compensation of patterning process effects," *Microelectronic Engineering*, vol. 110, no. Supplement C, pp. 147 – 151, 2013.

[31] M. Rommel, K. Hoffmann, T. Reindl, J. Weis, N. Unal, and U. Hofmann, "Benchmark test of Monte-Carlo simulation for high resolution electron beam lithography," *Microelectronic Engineering*, vol. 98, pp. 202–205, 2012.

[32] M. Rommel, B. Nilsson, P. Jedrasik, V. Bonanni, A. Dmitriev, and J. Weis, "Sub-10nm resolution after lift-off using HSQ/PMMA double layer resist," *Microelectronic Engineering*, vol. 110, pp. 123 – 125, 2013.

[33] M. Rommel and J. Weis, "Hydrogen silsesquioxane bilayer resists - Combining high resolution electron beam lithography and gentle resist removal," *Journal of Vacuum Science and Technology B: Microelectronics and Nanometer Structures*, vol. 31, no. 6, pp. 06F102–1 – 06F102–5, 2013.

[34] M. Rommel and B. Nilsson, "Estimating the optimum dose for arbitrary substrate materials based on Monte Carlo simulated point spread functions," *Microelectronic Engineering*, vol. 155, pp. 29–32, 2016.

[35] R. Jany, C. Richter, C. Woltmann, G. Pfanzelt, B. Förg, M. Rommel, T. Reindl, U. Waizmann, J. Weis, J. Mundy, D. Muller, H. Boschker, and J. Mannhart, "Monolithically Integrated Circuits from Functional Oxides," *Advanced Materials Interfaces*, vol. 1, no. 1, pp. 1300031–1 – 1300031–7, 2014.

[36] S. De Zuani, T. Reindl, M. Rommel, B. Gompf, A. Berrier, and M. Dressel, "High-Order Hilbert Curves: Fractal Structures with Isotropic, Tailorable Optical Properties," *ACS Photonics*, vol. 2, no. 12, pp. 1719–1724, 2015.

[37] S. De Zuani, M. Rommel, B. Gompf, A. Berrier, J. Weis, and M. Dressel, "Suppressed Percolation in Nearly Closed Gold Films," *ACS Photonics*, vol. 3, no. 6, pp. 1109–1115, 2016.

[38] V. R. Manfrinato, J. Wen, L. Zhang, Y. Yang, R. G. Hobbs, B. Baker, D. Su, D. Zakharov, N. J. Zaluzec, D. J. Miller, E. A. Stach, and K. K. Berggren, "Determining the Resolution Limits of Electron-Beam

Lithography: Direct Measurement of the Point-Spread Function," *Nano Letters*, vol. 14, no. 8, pp. 4406–4412, 2014.

[39] T. H. P. Chang, "Proximity effect in electron-beam lithography," *Journal of Vacuum Science and Technology*, vol. 12, no. 6, pp. 1271–1275, 1975.

[40] S. A. Rishton and D. P. Kern, "Point exposure distribution measurements for proximity correction in electron beam lithography on a sub-100 nm scale," *Journal of Vacuum Science & Technology B*, vol. 5, no. 1, pp. 135–141, 1987.

[41] P. Hudek and D. Beyer, "Exposure optimization in high-resolution e-beam lithography," *Microelectronic Engineering*, vol. 83, no. 4, pp. 780 – 783, 2006.

[42] GenISys GmbH, Munich, *BEAMER - Advancing the standard - v5.4.3 Manual*, 2017.

[43] K. Königsberger, *Analysis 2*. Springer, Berlin, Heidelberg, 2000.

[44] G. Udupa, M. Singaperumal, R. S. Sirohi, and M. P. Kothiyal, "Characterization of surface topography by confocal microscopy: I. Principles and the measurement system," *Measurement Science and Technology*, vol. 11, no. 3, p. 305, 2000.

[45] B. Bhushan, J. C. Wyant, and C. L. Koliopoulos, "Measurement of surface topography of magnetic tapes by Mirau interferometry," *Appl. Opt.*, vol. 24, pp. 1489–1497, May 1985.

[46] M. H. Kalos and P. A. Whitlock, *Monte Carlo Methods. Vol. 1: Basics*. New York, NY, USA: Wiley-Interscience, 1986.

[47] M. Berger, *Methods in Computational Physics, vol. 1, Statistical Physics*, vol. 1, ch. Monte Carlo Calculation of the Penetration and Diffusion of Fast Charged Particles, pp. 135–215. New York and London: Academic Press, 1963.

[48] H. Bethe, "Zur Theorie des Durchgangs schneller Korpuskularstrahlen durch Materie," *Annalen der Physik*, vol. 397, no. 3, pp. 325–400, 1930.

[49] R. H. Garvey and A. E. S. Green, "Energy-apportionment techniques based upon detailed atomic cross sections," *Phys. Rev. A*, vol. 14, pp. 946–953, Sep 1976.

[50] R. Bracewell, *The Fourier Transform and Its Applications, 3rd ed.* New York, USA: McGraw-Hill, 3rd ed., 1999.

[51] L. Stevens, R. Jonckheere, E. Froyen, S. Decoutere, and D. Lanneer, "Determination of the proximity parameters in electron beam lithography using doughnut-structures," *Microelectronic Engineering*, vol. 5, no. 1, pp. 141 – 150, 1986.

[52] K. Keil, M. Hauptmann, K.-H. Choi, J. Kretz, L. M. Eng, and J. W. Bartha, "Fast backscattering parameter determination in e-beam lithography with a modified doughnut test," *Microelectronic Engineering*, vol. 86, no. 12, pp. 2408 – 2411, 2009.

[53] L. E. Ocola and A. Stein, "Effect of cold development on improvement in electron-beam nanopatterning resolution and line roughness," *Journal of Vacuum Science & Technology B: Microelectronics and Nanometer Structures Processing, Measurement, and Phenomena*, vol. 24, no. 6, pp. 3061–3065, 2006.

[54] A. Schleunitz, V. A. Guzenko, M. Messerschmidt, H. Atasoy, R. Kirchner, and H. Schift, "Novel 3D micro- and nanofabrication method using thermally activated selective topography equilibration (TASTE) of polymers," *Nano Convergence*, vol. 1, p. 7, Feb 2014.

[55] H. G. Craighead, R. E. Howard, L. D. Jackel, and P. M. Mankiewich, "10-nm linewidth electron beam lithography on GaAs," *Applied Physics Letters*, vol. 42, no. 1, pp. 38–40, 1983.

[56] W. W. Hu, K. Sarveswaran, M. Lieberman, and G. H. Bernstein, "Sub-10 nm electron beam lithography using cold development of poly(methylmethacrylate)," *Journal of Vacuum Science & Technology B: Microelectronics and Nanometer Structures Processing, Measurement, and Phenomena*, vol. 22, no. 4, pp. 1711–1716, 2004.

[57] M. A. Mohammad, C. Guthy, S. Evoy, S. K. Dew, and M. Stepanova, "Nanomachining and clamping point optimization of silicon carbon nitride resonators using low voltage electron beam lithography and cold development," *Journal of Vacuum Science & Technology B, Nanotechnology and Microelectronics: Materials, Processing, Measurement, and Phenomena*, vol. 28, no. 6, pp. C6P36–C6P41, 2010.

[58] K. Albrecht, M. Stickler, and T. Rhein, *Ullmann's Encyclopedia of Industrial Chemistry*, ch. Polymethacrylates. Wiley-VCH Verlag GmbH & Co. KGaA, 2000.

[59] G. H. Bernstein and D. A. Hill, "On the attainment of optimum developer parameters for PMMA resist," *Superlattices and Microstructures*, vol. 11, no. 2, pp. 237 – 240, 1992.

[60] S. Yasin, D. Hasko, and H. Ahmed, "Comparison of MIBK/IPA and water/IPA as PMMA developers for electron beam nanolithography," *Microelectronic Engineering*, vol. 61-62, no. Supplement C, pp. 745 – 753, 2002.

[61] J. S. Papanu, D. S. Soane (Soong), A. T. Bell, and D. W. Hess, "Transport models for swelling and dissolution of thin polymer films," *Journal of Applied Polymer Science*, vol. 38, no. 5, pp. 859–885, 1989.

[62] B. Cord, J. Lutkenhaus, and K. K. Berggren, "Optimal temperature for development of poly(methylmethacrylate)," *Journal of Vacuum Science & Technology B: Microelectronics and Nanometer Structures Processing, Measurement, and Phenomena*, vol. 25, no. 6, pp. 2013–2016, 2007.

[63] I. Haller, M. Hatzakis, and R. Srinivasan, "High-resolution Positive Resists for Electron-beam Exposure," *IBM Journal of Research and Development*, vol. 12, pp. 251–256, May 1968.

[64] A. Grigorescu, M. van der Krogt, C. Hagen, and P. Kruit, "10nm lines and spaces written in HSQ, using electron beam lithography," *Microelectronic Engineering*, vol. 84, no. 5, pp. 822 – 824, 2007.

[65] D. Corning, "XR-1541-002 e-beam resist." data sheet, 2017.

[66] S.-W. Nam, M. J. Rooks, J. K. W. Yang, K. K. Berggren, H.-M. Kim, M.-H. Lee, K.-B. Kim, J. H. Sim, and D. Y. Yoon, "Contrast enhancement behavior of hydrogen silsesquioxane in a salty developer," *Journal of Vacuum Science & Technology B: Microelectronics and Nanometer Structures Processing, Measurement, and Phenomena*, vol. 27, no. 6, pp. 2635–2639, 2009.

[67] J. K. W. Yang and K. K. Berggren, "Using high-contrast salty development of hydrogen silsesquioxane for sub-10-nm half-pitch lithography," *Journal of Vacuum Science & Technology B: Microelectronics and Nanometer*

Structures Processing, Measurement, and Phenomena, vol. 25, no. 6, pp. 2025–2029, 2007.

[68] W. Henschel, Y. M. Georgiev, and H. Kurz, "Study of a high contrast process for hydrogen silsesquioxane as a negative tone electron beam resist," *Journal of Vacuum Science & Technology B: Microelectronics and Nanometer Structures Processing, Measurement, and Phenomena*, vol. 21, no. 5, pp. 2018–2025, 2003.

[69] F. Gaucher, A. Pautrat, S. Autier-Laurent, C. David, L. Calvet, P. Lecoeur, and A.-M. Haghiri-Gosnet, "Fabrication of metallic oxide nanowires," *Microelectronic Engineering*, vol. 86, no. 4, pp. 820 – 823, 2009.

[70] F. Stade, A. Heeren, M. Fleischer, and D. Kern, "Fabrication of metallic nanostructures for investigating plasmon-induced field enhancement," *Microelectronic Engineering*, vol. 84, no. 5, pp. 1589 – 1592, 2007.

[71] V. Sidorkin, A. Grigorescu, H. Salemink, and E. van der Drift, "Resist thickness effects on ultra thin HSQ patterning capabilities," *Microelectronic Engineering*, vol. 86, no. 4, pp. 749 – 751, 2009.

[72] T. Arnal, R. Soulimane, A. Aassime, M. Bibes, P. Lecoeur, A. Haghiri-Gosnet, B. Mercey, A. Khvalkovskii, A. Zvezdin, and K. Zvezdin, "Magnetic nanowires patterned in the La2/3Sr1/3MnO3 half-metal," *Microelectronic Engineering*, vol. 78-79, no. Supplement C, pp. 201 – 205, 2005.

[73] M. Häffner, A. Haug, A. Heeren, M. Fleischer, H. Peisert, T. Chassé, and D. P. Kern, "Influence of temperature on HSQ electron-beam lithography," *Journal of Vacuum Science & Technology B: Microelectronics and Nanometer Structures Processing, Measurement, and Phenomena*, vol. 25, no. 6, pp. 2045–2048, 2007.

[74] F. C. M. J. M. van Delft, "Delay-time and aging effects on contrast and sensitivity of hydrogen silsesquioxane," *Journal of Vacuum Science & Technology B: Microelectronics and Nanometer Structures Processing, Measurement, and Phenomena*, vol. 20, no. 6, pp. 2932–2936, 2002.

[75] F. C. M. J. M. van Delft, J. P. Weterings, A. K. van Langen-Suurling, and H. Romijn, "Hydrogen silsesquioxane/novolak bilayer resist for high aspect ratio nanoscale electron-beam lithography," *Journal of Vacuum*

Science & Technology B: Microelectronics and Nanometer Structures Processing, Measurement, and Phenomena, vol. 18, no. 6, pp. 3419–3423, 2000.

[76] H. Namatsu, T. Yamaguchi, M. Nagase, K. Yamazaki, and K. Kurihara, "Nano-patterning of a hydrogen silsesquioxane resist with reduced linewidth fluctuations," *Microelectronic Engineering*, vol. 41-42, no. Supplement C, pp. 331 – 334, 1998.

[77] X. Yang, S. Xiao, W. Wu, Y. Xu, K. Mountfield, R. Rottmayer, K. Lee, D. Kuo, and D. Weller, "Challenges in 1teradotin^2 dot patterning using electron beam lithography for bit-patterned media," *Journal of Vacuum Science & Technology B: Microelectronics and Nanometer Structures Processing, Measurement, and Phenomena*, vol. 25, no. 6, pp. 2202–2209, 2007.

[78] H. Duan, H. Hu, K. Kumar, Z. Shen, and J. K. W. Yang, "Direct and Reliable Patterning of Plasmonic Nanostructures with Sub-10-nm Gaps," *ACS Nano*, vol. 5, no. 9, pp. 7593–7600, 2011.

[79] P. Walker and W. H. Tran, eds., *CRC Handbook of Metal Etchants*. Boca Raton, FL, USA: CRC Press, 2010.

[80] A. E. Grigorescu and C. W. Hagen, "Resists for sub-20-nm electron beam lithography with a focus on HSQ: state of the art," *Nanotechnology*, vol. 20, no. 29, p. 292001, 2009.

[81] O. J. Guy, G. Burwell, A. Castaing, and K.-A. D. Walker, *Photochemistry in Electronics*, pp. 435–465. Dordrecht: Springer Netherlands, 2013.

[82] S. Xiao and X. Yang, "Electron-beam patterning and process optimization for magnetic sensor fabrication," *Journal of Vacuum Science & Technology B: Microelectronics and Nanometer Structures Processing, Measurement, and Phenomena*, vol. 24, no. 6, pp. 2940–2944, 2006.

[83] H. Yang, A. Jin, Q. Luo, J. Li, C. Gu, and Z. Cui, "Electron beam lithography of HSQ/PMMA bilayer resists for negative tone lift-off process," *Microelectronic Engineering*, vol. 85, no. 5, pp. 814 – 817, 2008.

[84] L. Magdenko, F. Gaucher, A. Aassime, M. Vanwolleghem, P. Lecoeur, and B. Dagens, "Sputtered metal lift-off for grating fabrication on InP based optical devices," *Microelectronic Engineering*, vol. 86, no. 11, pp. 2251 – 2254, 2009.

[85] H. Duan, H. Hu, H. Hui, Z. Shen, and J. Yang, "Free-standing sub-10 nm nanostencils for the definition of gaps in plasmonic antennas," *Nanotechnology*, vol. 24, no. 18, p. 185301, 2013.

[86] Z. Cui, *Nanofabrication: Principles, Capabilities and Limits*. Bosten, MA, USA: Springer US, 2008.

[87] L. E. Ocola, M. Costales, and D. J. Gosztola, "Development characteristics of polymethyl methacrylate in alcohol/water mixtures: a lithography and Raman spectroscopy study," *Nanotechnology*, vol. 27, no. 3, p. 035302, 2016.

[88] J. Penaud, F. Fruleux, and E. Dubois, "Transformation of hydrogen silsesquioxane properties with RIE plasma treatment for advanced multiple-gate MOSFETs," *Applied Surface Science*, vol. 253, no. 1, pp. 395 – 399, 2006.

[89] C. T. Koch, W. Sigle, R. Höschen, M. Rühle, E. Essers, G. Benner, and M. Matijevic, "SESAM: Exploring the Frontiers of Electron Microscopy," *Microscopy and Microanalysis*, vol. 12, no. 6, pp. 506–514, 2006.

[90] D. B. Williams and C. B. Carter, *The Transmission Electron Microscope*, pp. 3–17. Boston, MA: Springer US, 1996.

[91] P. Schattschneider, S. Rubino, C. Hebert, J. Rusz, J. Kunes, P. Novák, E. Carlino, M. Fabrizioli, G. Panaccione, and G. Rossi, "Detection of magnetic circular dichroism using a transmission electron microscope," *Nature*, vol. 441, pp. 486–488, May 2006.

[92] J. Rusz, O. Eriksson, P. Novák, and P. M. Oppeneer, "Sum rules for electron energy loss near edge spectra," *Phys. Rev. B*, vol. 76, p. 060408, Aug 2007.

[93] J. Verbeeck, H. Tian, and P. Schattschneider, "Production and application of electron vortex beams," *Nature*, vol. 467, pp. 301–304, Sep 2010.

[94] N. R. Heckenberg, R. McDuff, C. P. Smith, H. Rubinsztein-Dunlop, and M. J. Wegener, "Laser beams with phase singularities," *Optical and Quantum Electronics*, vol. 24, pp. S951–S962, Sep 1992.

[95] R. D. Leapman, L. A. Grunes, and P. L. Fejes, "Study of the L_{23} edges in the $3d$ transition metals and their oxides by electron-energy-loss spectroscopy with comparisons to theory," *Phys. Rev. B*, vol. 26, pp. 614–635, Jul 1982.

[96] G. Schütz, W. Wagner, W. Wilhelm, P. Kienle, R. Zeller, R. Frahm, and G. Materlik, "Absorption of circularly polarized x rays in iron," *Phys. Rev. Lett.*, vol. 58, pp. 737–740, Feb 1987.

[97] W. Khunsin, B. Brian, J. Dorfmüller, M. Esslinger, R. Vogelgesang, C. Etrich, C. Rockstuhl, A. Dmitriev, and K. Kern, "Long-Distance Indirect Excitation of Nanoplasmonic Resonances," *Nano Letters*, vol. 11, no. 7, pp. 2765–2769, 2011.

[98] H. Fredriksson, Y. Alaverdyan, A. Dmitriev, C. Langhammer, D. Sutherland, M. Zäch, and B. Kasemo, "Hole-Mask Colloidal Lithography," *Advanced Materials*, vol. 19, no. 23, pp. 4297–4302, 2007.

[99] M. Schwind, V. D. Miljković, M. Zäch, V. Gusak, M. Käll, I. Zorić, and P. Johansson, "Diffraction from Arrays of Plasmonic Nanoparticles with Short-Range Lateral Order," *ACS Nano*, vol. 6, no. 11, pp. 9455–9465, 2012.

[100] A. Oliver, J. C. Cheang-Wong, A. Crespo, J. M. Hernández, C. Solís, E. M. noz, R. Espejel-Morales, and J. Siejka, "Study of the optical properties of fused quartz after a sequential implantation with Si and Au ions," *Applied Physics Letters*, vol. 73, no. 11, pp. 1574–1576, 1998.

[101] M. Hövel, B. Gompf, and M. Dressel, "Dielectric properties of ultrathin metal films around the percolation threshold," *Phys. Rev. B*, vol. 81, p. 035402, Jan 2010.

[102] S. De Zuani, T. Peterseim, A. Berrier, B. Gompf, and M. Dressel, "Second harmonic generation enhancement at the percolation threshold," *Applied Physics Letters*, vol. 104, no. 24, p. 241109, 2014.

[103] A. Belardini, A. Benedetti, M. Bertolotti, M. Centini, and C. Sibilia, "Second harmonic generation from artificial metasurfaces," *Proc. SPIE*, vol. 9503, pp. 950306–950306–8, 2015.

[104] D. Hilbert, "Über die stetige Abbildung einer Line auf ein Flächenstück," *Mathematische Annalen*, vol. 38, no. 3, pp. 459–460, 1891.

[105] M. Mohammad, T. Fito, J. Chen, S. Buswell, M. Aktary, M. Stepanova, and S. Dew, "Systematic study of the interdependence of exposure and development conditions and kinetic modelling for optimizing low-energy electron beam nanolithography," *Microelectronic Engineering*, vol. 87, no. 5, pp. 1104 – 1107, 2010.

[106] Y. Chen, H. Yang, and Z. Cui, "Effects of developing conditions on the contrast and sensitivity of hydrogen silsesquioxane," *Microelectronic Engineering*, vol. 83, no. 4, pp. 1119 – 1123, 2006.

[107] M. J. Rooks, E. Kratschmer, R. Viswanathan, J. Katine, R. E. F. Jr., and S. A. MacDonald, "Low stress development of poly(methylmethacrylate) for high aspect ratio structures," *Journal of Vacuum Science & Technology B: Microelectronics and Nanometer Structures Processing, Measurement, and Phenomena*, vol. 20, no. 6, pp. 2937–2941, 2002.

[108] H. E. Bennett and J. M. Bennett, *Optical Properties and Electronic Structure of Metals and Alloys: Proceedings of the International Colloquim*, ch. Validity of the Drude theory for silver, gold and aluminum in the infrared. North-Holland Publ.Comp., 1966.

Selbstständigkeitserklärung

Hiermit erkläre ich, dass die vorliegende Arbeit von mir eigenständig und ohne fremde Hilfe verfasst wurde. Weiterhin versichere ich, dass die Resultate auf von mir durchgeführten Experimenten beruhen. Alle von mir übernommenen Aussagen, Tabellen, Grafiken oder Ähnliches als auch von mir mit eigenen Worten wiedergegebene Aussagen, abgewandelte Tabellen, Grafiken oder Ähnliches sind als solche gekennzeichnet und die entsprechenden Quellen sind angegeben.

Marcus Rommel

Landvetter, den 11. Februar 2018

Acknowledgements

Finally, I would like to thank everybody contributing to this work or helping and supporting me on my way closing this chapter of my life. My special thanks goes to:

- Prof. Dr. (apl.) Jürgen Weis for taking on the supervision of this work, the great support and providing a modern nanofabrication infrastructure. Further, I am very thankful for getting the freedom to follow my own research interests and for encouraging me in building up my own collaborations.
- Prof. Dr. Martin Dressel for the successful collaboration with his department and the evaluation of this thesis.
- Prof. Dr. Klaus von Klitzing for giving me the opportunity to join his department and to do my research in a friendly and constructive environment.
- Thomas Reindl, Bengt Nilsson and Ulrich Hofmann for being great mentors and friends introducing me to the fascinating craft, art and science of electron beam lithography. I am deeply grateful for all the shared knowledge, the suggestions and advices in the whole field of nanofabrication and beyond.
- Niclas Lindvall for being a great and energetic colleague, taking the load off me as well as pushing me gently when ever it is necessary and for proofreading this thesis.
- The staff of the Nanostructuring Lab at the Max-Planck Institute in Stuttgart and the Nanofabrication Laboratory at Chalmers University of Technology in Gothenburg for taking care of all the sophisticated equipment and sharing their profound and highly specialized knowledge creating amazing research environments.
- Daniel Ritter, Dr. Christoph Sambale and Nezih Ünal as well as the whole GenISys team for providing an enormous suit of tools improving electron

beam lithography results. Moreover, I would like to thank you for being the basis for the whole EBL community.

- Dr. Leonhard Schulz, Dr. Marcel Mausser and Dr. Moritz Esslinger for being a constant source of good advice, all the long discussion concerning science and beyond as well as all the fun we had together. Thanks guys.
- Dr. Maximilian Köpke, Dr. Konstantinos Panos and Andreas Gauß for being great colleagues.
- All the members of the departments von Klitzing and Mannhart for the nice atmosphere.
- My parents Petra and Lutz Rommel as well as my grand parents Marianne and Harald Rommel as well as Gisela and Albrecht Kühr for their absolute support, patience and warm motivating words. Thank you for all the freedom.
- My dear wife Sonja for enduring me while writing, providing fruitful discussions and proofreading this thesis so many times. Together with our beloved son Arthur you are the backbone of our life. Thank you.

Marcus Rommel

Person

Date of birth:	08.09.1987, Eisenach, Germany

Current Status

since 02/2014	**Research Engineer at the Nanofabrication Laboratory, Chalmers University of Technology, Gothenburg, Sweden**

Education

08/2010 – 01/2014	**PhD student at the Nanostructuring Lab, Max Planck Institute for Solid State Research, Stuttgart, Germany** Thesis: "High Resolution Electron Beam Lithography - An improved understanding of a versatile lithography technique"
10/2006 – 07/2010	**Julius-Maximilians-Universität Würzburg** Course of study: Physics Thesis: "Setup of a fully achromatic, pulsed excitation apertureless scanning near-field optical microscope for ultrafast nano-optics" at the Nanoscale Science Department, Max Planck Institute for Solid State Research Stuttgart
09/2002 – 07/2006	**Math.-nat. Spezialschulteil am Albert-Schweitzer-Gymnasium Erfurt** Secondary school with general qualification for university entrance